3-27-2019

Coherent and Incoherent Dynamics of Quasiparticles in Monolayer Molybdenum Diselenide

Michael Titze
mtitz001@fiu.edu

FLORIDA INTERNATIONAL UNIVERSITY

Miami, Florida

COHERENT AND INCOHERENT DYNAMICS OF QUASIPARTICLES IN MONOLAYER MOLYBDENUM DISELENIDE

A dissertation submitted in partial fulfillment

of the requirements for the degree of

DOCTOR OF PHILOSOPHY

in

PHYSICS

by

Michael Titze

2019

To: Dean Michael R. Heithaus
College of Arts, Sciences, and Education

This dissertation, written by Michael Titze, and entitled Coherent and Incoherent Dynamics of Quasiparticles in Monolayer Molybdenum Diselenide, having been approved in respect to style and intellectual content, is referred to you for judgment.

We have read this dissertation and recommend that it be approved.

Bernard Gerstman

Raphael Raptis

Yifu Zhu

Hebin Li, Major Professor

Date of Defense: March 27, 2019

The dissertation of Michael Titze is approved.

Dean Michael R. Heithaus
College of Arts, Sciences, and Education

Andrés G. Gil
Vice President for Research and Economic Development
and Dean of the University Graduate School

Florida International University, 2019

ACKNOWLEDGMENTS

This page is here to thank those who have helped me in the process of obtaining the graduate degree.

First, I would like to thank my committee members Hebin Li, Bernard Gerstman, Raphael Raptis and Yifu Zhu for the time and effort they took to make this dissertation a reality. I also thank the Ultrafast Optics research group at Florida International University. I thank financial support through the Florida International University Dissertation Year Fellowship giving me the opportunity to focus on the writing of this thesis.

Personally, I want to express my gratitude to Hebin Li for pushing me to keep working on the experiment, even when I wanted to give up. He taught me how to independently perform research and showed me how to identify the correct questions to ask for advancing scientific knowledge. To Feng Gao, who has greatly helped setting up the lab and who has taught me some tricks on how to align optics. Without his efforts this work would have been significantly delayed. To Alex Sarracino, who has spent countless hours in complete darkness staring at a computer screen with me for photoluminescence characterization of samples and who has introduced me to the beauty of python programming and still is available for debugging my code. To Shaogang Yu, with whom I had many interesting and insightful discussions and who has taught me how to operate the collinear 2D setup. To Feng Zhang, who took the lead on the strained monolayer research freeing up my time to focus on the 2D experiment. To Maria Munoz, who has helped in operating the non-collinear setup and whose input was helpful for perfecting the work on perovskites. To everyone else who have worked with me in the ultrafast optics group, especially Raybel Almeida and Eduardo Guevara who have built custom microscopes for the research group.

To Bernard Gerstman, who did not get tired of asking questions during my annual

reviews, pushing me to gain a broader view of the research field. To Xuewen Wang who was always available for discussion and providing valuable input from a theorists side of view. To He Wang at the University of Miami, who has generously made thin film perovskite samples for us and helped us in understanding the physics inside the material, allowing me to dive into a completely new material system with minimal guidance.

To those in the broader 2D spectroscopy community, thank you for welcoming me into this wonderful group of people and teaching me the power of 2D spectroscopy. Particularly to Steve Cundiff and his research group: thank you for opening your doors, letting me visit, and giving me feedback on my work. A special thanks goes out to Christopher Smallwood who helped with the analysis of 2D spectra and to Eric Martin, who has given invaluable guidance on the collinear setup.

To Gabriel Allan for help with making the drawings in the appendix.

Finally, I want to thank my family. Most importantly, for helping both financially and physically to move to Miami and getting settled. To my mom for her ongoing support throughout my long-lasting education. To my dad, who has always been there to talk even with the time-shift. To my brother, who has made the long time away more bearable by keeping me in touch with the most recent german youtube content.

ABSTRACT OF THE DISSERTATION

COHERENT AND INCOHERENT DYNAMICS OF QUASIPARTICLES IN MONOLAYER MOLYBDENUM DISELENIDE

by

Michael Titze

Florida International University, 2019

Miami, Florida

Professor Hebin Li, Major Professor

Monolayer Materials, especially single-layer graphite, called graphene, as the first synthesized and most prominent representative, have attracted significant research interest since its discovery in 2004. The efforts were rewarded with a Nobel prize in 2010 for the discovery of graphene, the same year in which the first monolayer transition metal dichalcogenide (ML-TMD) was found to have a direct bandgap. In contrast to graphene ML-TMDs have a direct bandgap in the visible or near-infrared spectral range, making them ideally suited for optoelectronic device applications. Explicit inversion symmetry breaking of the unit cell in ML-TMDs furthermore leads to a new interesting property, called valley pseudo-spin. Electrons excited within one valley are restricted to this valley due to momentum trapping. Investigating the valley pseudo-spin dynamics is of importance for both understanding of the fundamental physics as well as device applications since the valley pseudo-spin is a potential information carrier and has potential use for information storage or computing application.

Additionally, the confinement to two dimensions leads to enhanced Coulomb interaction and increased dielectric screening between electron and hole. Interestingly, the two-dimensional screening effects were already studied before the first two-dimensional materials were synthesized on quasi-two-dimensional systems. The screening of the Coulomb interaction in turn leads to a significantly increased binding

energy between electron and hole, such that the bound electron-hole state, so-called exciton, is stable up to room temperature and above. The same reasoning leads to an enhanced stability of charged excitons, so-called trions, which are the main focus of this dissertation. The optical response of ML-TMDs is therefore completely dominated by excitons and trions, requiring an in-depth understanding of these quasiparticles for device performance optimization.

While steady-state measurements can provide valuable insight into a material system, such as the bandgap of a semiconductor or the fact that valley spin exists and the amount of valley polarization upon continuous excitation, ultimately dynamics information is of importance for device applications. Time-resolved techniques allow access of transients and can reveal the lifetime of unstable and metastable states, which may be invisible in steady-state measurements. Excitation by a pulsed coherent source allows access to the dynamics of coherent states, which are especially interesting for quantum computing applications. A quantum system only exhibits quantum mechanical correlations within its coherence time, such that a measurement of the coherence time is essential for evaluating materials as potential platforms for quantum computing. Furthermore, coherent techniques are known for their ability to probe many-body effects and microscopic inhomogeneity, which are especially prominent effects in semiconductors. The technique used to investigate the coherent trion dynamics in this dissertation is two-dimensional coherent spectroscopy, a nonlinear coherent technique, that resolves the signal as a function of two time delays. Using two-dimensional spectroscopy, it is possible to measure the homogeneous linewidth, which is related to the coherence time, even in a strongly inhomogeneously broadened system. The measurement of the coherence time marks the first step in evaluating a material for possible quantum computation applications.

GERMAN ABSTRACT OF THE DISSERTATION

KOHÄRENTE UND INKOHÄRENTE DYNAMIK VON QUASITEILCHEN IN MOLYBDÄNDISELENID EINZELLAGEN

von

Michael Titze

Florida International University, 2019

Miami, Florida

Professor Hebin Li, Doktorvater

Einzellagenkristalle, insbesondere einlagiges Graphit, sogenanntes Graphen, als der zuerst synthetisierte und bekannteste Vertreter der Einzellagenkristalle, sind seit ihrer Entdeckung im Jahr 2004 im Fokus signifikanter Forschungsanstrengungen. Die Forschungen wurden im Jahr 2010 mit einem Nobelpreis für die Entdeckung von Graphen gewürdigt, dem gleichen Jahr in dem die direkte Bandlücke in den ersten Übergangsmetall-Dichalcogenid (ÜMD) Einzellagen experimentell nachgewiesen wurde. Im Unterschied zu Graphen haben ÜMD Einzellagen eine direkte Bandlücke im optischen oder nahinfraroten Spektralbereich, wodurch sie ideal für Anwendungen in optoelektrischen Schaltungen geeignet sind. Durch die explizite Brechung der Inversionssymmetrie der Elementarzelle in ÜMD Einzellagen haben Elektronen und Löcher im Kristall eine neuartige Eigenschaft, den sogenannten Valley Pseudo-Spin. Elektronen die innerhalb eines Valleys angeregt werden sind aufgrund ihres Impulses innerhalb dieses Valleys gefangen. Als neuartige und nur in ÜMD Einzellagen optisch addressierbare Eigenschaft ist die Erforschung der Dynamik des Valley Pseudo-Spin sowohl aus Sicht der Grundlagenforschung als auch im Hinblick auf mögliche Anwendungen interessant, da der Valley Psudo-Spin potentiell zur Informationsspeicherung oder für computing verwendet werden kann.

Weiterhin führt die Einschränkung von Elektronen und Löchern auf zwei Dimen-

sionen zu einer Verstärkung der Coulomb Wechselwirkung zwischen den beiden sowie einer erhöhten dielektrischen Abschirmung. Interessanterweise wurden die Abschirmeffekte durch Beschränkung auf zwei Dimensionen bereits vor der Entdeckung von Einzellagenkristallen mithilfe von quasi-zwei-dimensionalen Systemen untersucht. Die Abschirmung der Coulomb Wechselwirkung führt zu einer signifikanten Erhöhung der Bindungsenergie zwischen Elektron und Loch, sodass gebundene Elektron-Loch Zustände, sogenannte Exzitonen, bis zur Raumtemperatur und darüber hinaus stabil sind. Das gleiche Argument führt dazu, dass geladene Exzitonen, sogenannte Trionen, deren Eigenschaften im Hauptteil dieser Dissertation untersucht werden, auch stabiler sind als in Volumenkristallen. Die Elektronendynamik in ÜMD Einzellagen ist darum komplett durch Exzitonen und Trionen dominiert, sodass ein tiefgreifendes Verständnis derselben zur Anwendungsoptimierung notwendig ist.

Während die Messung von Zuständen im Gleichgewicht wertvolle Einblicke in ein Materialsystem gewährt, beispielsweise lässt sich die Bandlücke eines Halbleiters messen oder die Tatsache dass der Valley-Spin existiert nachweisen sowie die Menge des durch stationäre Anregung erzeugten Valley-Spins messen, ist ultimativ die Dynamik für die Anwendung entscheidend. Zeitaufgelöste Techniken erlauben den Zugang zu transienten und können die Lebensdauer von instabilen oder metastabilen Zuständen erfassen, welche in Gleichgewichtsmessungen nicht sichtbar sind. Die Anregung durch eine gepulste kohärente Quelle erlaubt zudem die Messung der Dynamik von kohärenten Zuständen, welche insbesondere in Hinblick auf Quantencomputing eine wichtige Messgröße darstellt. Ein Quantensystem zeigt nur während der Kohärenzzeit nicht-klassische Korrelationen, sodass die Messung der Kohärenzzeit einen essenzieller Schritt bei der Evaluierung eines Materials als Quantencomputing Plattform darstellt. Außerdem sind kohärente Techniken bekannt dafür Vielteilcheneffekte und mikroskopische Inhomogenität zu messen, welche insbesondere

in Halbleitern stark auftretende Effekte sind. Die Methode zur Untersuchung der kohärenten Trionendynamik in dieser Dissertation ist zwei-dimensionale kohärente Spektroskopie, eine nichtlineare kohärente Messtechnik, die ein Signal als Funktion zweier Zeitabstände misst. Mithilfe der zweidimensionalen kohärenten Spektroskopie ist es möglich die homogene Linienbreite welche mit der Kohärenzzeit verknüpft ist, auch in einem stark inhomogen verbreiterten System eindeutig zu messen. Die Messung der Kohärenzzeit stellt den ersten Schritt der Evaluierung eines Materials für den Einsatz in Quantenrechnern dar.

TABLE OF CONTENTS

LIST OF FIGURES

ABBREVIATIONS AND ACRONYMS

2DCS	- Two-Dimensional Coherent Spectroscopy
AR	- Anti-Reflection
CCD	- Charge-Coupled Device
CVD	- Chemical Vapor Deposition
cw	- Continuous Wave
EID	- Excitation Induced Dephasing
FT	- Fourier Transform
FWM	- Four-Wave Mixing
GaAs	- Gallium Arsenide
hBN	- Hexagonal Boron Nitride
ML	- Monolayer
MoS_2	- Molybdenum Disulfide
$MoSe_2$	- Molybdenum Diselenide
NMR	- Nuclear Magnetic Resonance
OBE	- Optical Bloch Equation
OPO	- Optic Parametric Oscillator
PID	- Phonon Induced Dephasing
PL	- Photoluminescence
PLL	- Phase-Locked Loop
RF	- Radio Frequency
SEQ	- Schrödinger Equation
SI	- Spectral Interferometry
T-FWM	- Transient Four-Wave Mixing
TI-FWM	- Time-Integrated Four-Wave Mixing
TMD	- Transition Metal Dichalcogenide

TR-PL - Time-Resolved Photoluminescence

μ-PL - Microscopy Photoluminescence

WS_2 - Tungsten Disulfide

WSe_2 - Tungsten Diselenide

PUBLICATIONS LEADING UP TO THIS THESIS

The following publications are directly related to the content of this thesis

1. F. Gao, Y. Gong, M. Titze, R. Almeida, P.M. Ajayan and H.Li, "Valley Trion Dynamics in Monolayer $MoSe_2$", Phys. Rev. B, 94:245413, Dec. 2016

2. M. Titze and H. Li, "Optical 2D coherent spectroscopy of valley dynamics in monolayer Transition Metal Dichalcogenide (Invited Paper)", Ultrafast Bandgap Photonics III, Apr. 2018

3. M. Titze, B. Li, X. Zhang, P.M. Ajayan and H. Li, "Intrinsic Coherence Time of Trions in Monolayer $MoSe_2$ Measured via Two-Dimensional Coherent Spectroscopy", Phys. Rev. Materials, 2:054001, May 2018

1 Introduction

1.1 Monolayer Materials

Since the discovery of graphene in 2004, monolayer (ML) materials have become a major point of attention in the condensed matter physics community, culminating in the Nobel prize in physics for the discovery of graphene in the year 2010, only six years after its first synthesis [2, 3]. Besides graphene as the first discovered and most prominent representative of ML materials, many other materials have been reduced to MLs [4, 5]. All these materials have a layered crystal structure with the interlayer coupling being due to the weak induced-dipole van-der-Waals interaction simplifying the exfoliation of single layer crystals. Among the layered materials, transition metal dichalcogenides (TMDs) are a class of materials that are indirect semiconductors in bulk with a bandgap around the Γ point, similar to the electronic structure of silicon. When reduced to a single molecular layer, the bandgap widens and shifts from the Γ point to the K points. The derivation of this phenomenon can be found in Section 2 based on an approximation of the bandstructure in a nearest-neighbor interaction tight-binding model. Besides a shift of the bandgap location, the bandgap also shifts from an indirect one to a direct bandgap leading to an enhanced light absorption and emission on resonance [6–9]. A single molecular layer can absorb up to 20 %, much more than in the bilayer case and the emission is enhanced in the ML by approximately a factor 100 compared to a multilayer sample [4]. In graphene the K points are equivalent because the unit cell is inversion symmetric, but in ML-TMDs, there are two inequivalent K points reflecting the explicit inversion symmetry breaking of the unit cell. The large separation of the K points in momentum space means that electrons can be excited into two different states that are energetically degenerate [10]. The two states can therefore be treated like an energetically degenerate spin-$\frac{1}{2}$ sys-

tem. Investigating the valley spin dynamics is of interest both on a fundamental physics level and for device applications, since the valley spin may be used as an information carrier and may be used for information storage or, given suitable coupling capabilities, computing applications [8, 11–16]. Moreover, the two-dimensional confinement of electrons and holes leads to an enhancement of the Coulomb interaction in combination with dielectric screening effects [17]. Although these effects were already studied before the first two-dimensional crystals were synthesized using quasi-two-dimensional systems, the advent of ML materials has opened a new route for the study of low dimensional systems [18].

Quasiparticles have been a topic of interest since the first discovery of direct bandgap semiconductors. Bound electron-hole states in semiconductors act as the solid-state equivalent to the hydrogen atom in atomic physics, representing a two-particle system with a Rydberg-like energy structure [19]. Studies of such quasiparticles allow insights into the dielectric environment in a semiconductor making them an ideal probe of the material they are in. The two-dimensional confinement of the quasiparticles leads to a significantly increased binding energy between electron and hole, such that excitons are stable up to room temperature and above in stark contrast to excitons in other well-studied direct bandgap semiconductors such as gallium arsenide (GaAs) [20]. Similarly, charged excitons called trions also have an increased binding energy making them exceptionally stable [21]. Consequentially, in ML materials the optoelectronic properties are completely dominated by bound electron-hole states such that an in-depth understanding of these quasiparticles is necessary prior to device applications.

To study quasiparticles, time-resolved techniques are used in the present dissertation. While steady-state measurements may be used to gain insight into some properties, such as the bandstructure, ultimately the timescale on which processes

happen is of interest. With the goal of information processing in mind, information about transients and possible decay channels into dark states is essential. Besides probing the population dynamics, which is presented in Section 4 and reveals the existence of defect states that trap trions, the coherent dynamics of trions are studied. The results, which are explained by decoherence of trions through scattering off of defect states that trap trions on a longer timescale, are shown in Section 5. To investigate the dynamics in the samples, different techniques are used which are described in the following section.

1.2 Two-Dimensional Coherent Spectroscopy

There are many techniques for performing time-resolved optical spectroscopy, such as time-resolved photoluminescence (TR-PL), transient and time-integrated four-wave-mixing (T-/TI-FWM), pump-probe spectroscopy and two-dimensional coherent spectroscopy (2DCS). To be able to probe the coherence dynamics, the exciting source needs to be coherent, such that a quantum coherence may be generated in the system. Furthermore, to investigate the coherent dynamics, the technique needs to resolve the time within which the coherence evolves. Photoluminescence and pump-probe spectroscopies do not allow access of the coherence time while nonlinear techniques such as second-harmonic generation, sum-frequency generation, FWM and 2DCS are sensitive to the sample coherence.

Although second order processes are intrinsically stronger than third order nonlinear processes because of a lower order in the perturbation expansion, the second order signal vanishes in all centrosymmetric materials, making them unsuitable for the investigation of most materials [22]. However, a significant advantage of second order processes lies in their ability to probe surfaces. Since a ML is intrinsically a surface and breaks inversion symmetry, second order processes can be used to study

MLs [23–27]. The downside of second order processes lies in the need for a state at the two-photon energy for the possibility of using resonant enhancement. Third order processes can circumvent this issue by never exciting the system to more than the single-photon energy. Contrary to second-order processes the third order signal exists in all materials and gives access to the coherence time. The signal strength can be significantly enhanced by using resonant excitation and probing conditions. Therefore, the FWM and 2DCS techniques used in this dissertation are all performed on resonance and fully degenerate. Although the resonant excitation improves signal strength, it comes at the cost of spectral overlap between signal and excitation source. Various techniques exist for rejecting noise in degenerate FWM techniques [28–32].

Originally 2DCS was developed in nuclear magnetic resonance (NMR) spectroscopy where it received a Nobel prize in chemistry in 1991 [33, 34]. In chemistry it has contributed greatly to the determination of crystal structures while in biology and neuroscience 2D NMR spectroscopy is used for mapping brain activity and is now a routinely used technique [35, 36]. In the optical domain however, the oscillatory period of the electromagnetic field is about six orders of magnitude higher. While NMR uses radio frequency (RF) pulses, optical domain signals are in the hundreds of THz region and impossible to electronically detect with phase resolution. Furthermore, the Fourier transform (FT) involved in the preparation of 2D spectra requires sub-wavelength stability, which, in the case of RF pulses, is easily realized while in the optical domain optic pathlength fluctuations must be corrected within nanometer precision. Due to these two requirements the transfer of 2DCS from the RF to the optical domain proved to be challenging. Although originally proposed in 1993 [37], it took years for the first 2D spectra to be recorded from model systems [38–47]. Topics of interest for 2DCS are the measurement of dynamics of electronic and vibrational transitions in molecules [48], interactions in atomic vapors, especially the weak

dipole-dipole interaction [49–51], and the study of coherence dynamics and many-body effects in semiconductors. 2DCS performed on semiconductors has revealed coupling between excitonic resonances and to unbound electron-hole pairs [43], by phase-resolving the signal evidence of many-body interactions was obtained [52] and detailed comparison between microscopic calculations and 2DCS results has shown the existence of correlation terms beyond a mean-field theory [53]. By adjusting the polarization of each of the exciting beams, biexcitonic resonances can be isolated because many-body contributions can be suppressed [54].

The general idea of 2DCS lies in correlating a signal to two time delays. Typically the experimental realization consists of using three excitation pulses with wavevectors $\vec{k}_A, \vec{k}_B$ and $\vec{k}_C$. These interact in the sample to produce a nonlinear mixing signal in all possible phase-matching directions. Throughout the experiments done here, the direction $\vec{k}_S = -\vec{k}_A + \vec{k}_B + \vec{k}_C$ is chosen. Pulses A and B are separated by a time delay τ, pulses B and C are separated by delay T and the signal is recorded as a function of the emission time t resulting in a three-dimensional time domain signal $S_i(\tau, T, t)$. The index i denotes the arrival time of the conjugated field with wavevector $-\vec{k}_A$. For a $S_I(\tau, T, t)$ spectrum the homogeneous and inhomogeneous broadening are separated because the phase accumulated during delay τ is cancelled during t. In a TFWM experiment this is known as the photon echo. However, in the case of a $S_{II}(\tau, T, t)$ spectrum, the phase during τ and t have the same sign and do not cancel. The sum of $S_I(\tau, T, t)$ and $S_{II}(\tau, T, t)$ spectrum produces a so-called correlation spectrum that isolates the absorptive part of the nonlinear response [55]. For the case of $S_{III}(\tau, T, t)$ spectra, a double-quantum coherence is generated during delay T and two- and more-photon transitions can be probed [50, 51, 56]. In the present dissertation, only $S_I(\tau, T, t)$ spectra are presented since these are able to reveal the homogeneous linewidth. Besides the separation of the homogeneous and

inhomogeneous broadening, the spreading of spectra along two dimensions enables the deconvolution of congested spectra, such that couplings in complex systems can be found. This was used to determine whether the beating observed in TI-FWM signals originates from quantum mechanical interference or electromagnetic interference [57, 58]. Furthermore, 2DCS allows probing of non-radiative coherences that are not coupled through a dipole allowed transition [1, 59].

For ML-TMDs 2DCS is of interest because of its high sensitivity making it an ideal technique to probe ML-TMDs with low quantum efficiency and only approximately 10 % light absorption on resonance. Topics of interest are the coherence time of excitons and trions in ML-TMDs, the determination of valley coherence dynamics, measurement of valley coupling and the coupling dynamics between different quasiparticles such as exciton and trion [15, 60–64].

2 Monolayer Materials

2.1 Introduction

The optical properties in ML materials differ strongly from their bulk counterparts [2, 6–9, 65, 66]. The optical properties in two-dimensional crystals are affected by the restriction of possible phonon-modes to the plane [67, 68] as well as an enhanced screening of the Coulomb interaction [10, 69–73]. The restriction to a plane introduces a shift of the band structure [6]. While in multilayer TMDs, the bandgap is an indirect one and located around the Γ-point, the bandgap increases and shifts to a direct one in the single-layer limit. Furthermore, the bandgap shifts to the K-point, such that the required electron momentum for near-bandgap excitation is non-zero [4, 6]. The band structure of ML-TMDs is explained through overlap between the large d-orbitals [74, 75] and, for non-suspended samples, by dielectric screening from the substrate [76]. Other than in graphene, the unit cell is not symmetric in ML-TMDs. In reciprocal space this means that the K points are split into a $+K$ and $-K$ point, which are energetically degenerate but electrons excited at the two points have opposite momentum [10]. The $+K$ and $-K$ points can be selectively excited by σ^+ and σ^- light. Exciting the sample with light of linear polarization can generate a superposition between the $+K$ and $-K$ valleys and was used for an indirect measurement of valley coherence [77].

2.2 Optical Excitations in Two-Dimensional Materials

Two-dimensional confinement of electrons and holes leads to an enhanced screening of the Coulomb interaction, increasing the binding energy between electron and hole when compared to the bulk crystal [20, 78, 79]. The large binding energy between electron and hole makes excitons and charged excitons, so-called trions, thermody-

namically stable up to room temperature, such that device performance is significantly affected by these quasiparticles [80–82].

In an intrinsic semiconductor, no trions are formed, since the charges are balanced. However, defects, impurities or doping can introduce excess charges which will bind to excitons forming trions [21]. In the case of ML-TMDs another source of excess charges is the substrate, from where a charge can be captured and bound to an exciton formed within the ML [83].

Before discussing bound states, the band structure of two-dimensional semiconductors with a hexagonal lattice structure is discussed, followed by the introduction of excitons and trions. At the end of this section an overview of the decay and dephasing processes of excitons and trions is given.

2.3 Bandstructure in Monolayer Semiconductors

Semiconductors have electronic properties that are inbetween those of insulators and metals. Their electric and optical properties are governed by the electronic band structure which stems from electrons being nearly free in the material but still being affected by atomic potentials in addition to the position of the Fermi energy. While all crystalline materials form a band structure, the electronic properties of each material depend on the number of available states to their highest-energy electrons. In metals, a band is not fully filled up making it easy for electrons to move around different energy levels even when excited by only small energies. In insulators the gap between the highest filled energy state and the next available state is too large for electrons to cover at room temperature, meaning their bandgap is ≥ 3 eV [84]. Semiconductors have a bandgap that is small enough for some electrons to get excited from the valence band to the conduction band, corresponding to $1-3$ eV. This energy also corresponds

to the energy of near-infrared and visible light, making electron properties accessible through optical methods.

The defining property of a crystal is the existence of a repeating pattern, forming a lattice structure. Therefore a potential created by the crystal structure has to obey the form

$$V(\vec{r}) = V(\vec{r} + \vec{R}) \tag{1}$$

where $\vec{R} = \sum_i n_i \vec{a}_i$ is a lattice vector made up of a linear combination of the basis vectors $\vec{a}_i$ with the restriction that the $n_i \in \mathbb{Z}$. It can be shown that an electron moving in a periodic potential has a wavefunction Ψ that satisfies the Bloch theorem [84]

$$e^{i\vec{k}\cdot\vec{R}_n}\Psi(\vec{k}, \vec{r}) = \Psi(\vec{k}, \vec{r} + \vec{R}_n) \tag{2}$$

with the crystal momentum $\vec{k}$. Equation 2 shows that the wavefunction at any two lattice points is equal up to a phase factor. The Schrödinger equation (SEQ) describing the electron wavefunction is

$$\left(-\frac{\hbar^2}{2m}\nabla^2 + V(\vec{r})\right)\Psi(\vec{r}) = E\Psi(\vec{r}) \tag{3}$$

with the potential satisfying the above mentioned condition of Equation 1, one can write

$$V(\vec{r}) = \sum_{\vec{R}} V_i(\vec{r} - \vec{R})$$

with $V_i(\vec{r})$ being the contribution of a single lattice site to the total potential and the sum being over all possible lattice vectors $\vec{R}$.

For graphene and ML-TMDs the tight-binding approximation is a good approximation for calculating the band structure [85–89]. The benefit of the tight-binding model is the fact that it returns an analytical result. The major drawback is that it

does not capture the bandstructure completely and deviates from more sophisticated but numerical methods, such as band structure calculations using density functional theory (DFT) [6]. It has been shown that upon including up to the third nearest neighbors the overall calculated bandstructure is in good agreement with the experimentally measured bandstructure [88]. For simplicity and since the main features are visible even in the most rudimentary approximation, the discussion here is limited to only nearest-neighbor interactions. The tight-binding approximation assumes that an electron is mostly bound to its lattice site meaning that perturbations from an atomic wavefunction are only due to interaction with lattice sites close to the excitation spot. Implementing the tight-binding approximation assuming that electrons only interact with nearest-neighbor lattice sites, the electron wavefunction in Equation 2 is rewritten as

$$\Psi(\vec{k},\vec{r}) = \frac{1}{\sqrt{N}} \sum_i e^{i\vec{k}\cdot\vec{R}_i} \Phi_a(\vec{r}-\vec{R}_i) \ ,$$

where the sum over i is still running through all lattice sites and with the atomic wavefunction Φ_a. The energy of the electron states is then found by solving for the eigenvalues of the SEQ Equation 3

$$E = \langle \Psi | H | \Psi \rangle. \tag{4}$$

Neglecting interactions with any atoms that are further away than the nearest-neighbors, the electron energy in the tight-binding model for a single-atom basis is

$$E = \langle \Phi_a | H | \Phi_a \rangle + \sum_{NN} \langle \Phi_a | V(\vec{r}-\vec{R}_i) | \Phi_a \rangle e^{i\vec{k}\cdot\vec{R}_i},$$

where the sum over NN now runs only over all nearest-neighbors of lattice site a instead of the whole crystal lattice. In ML-TMDs, there are two non-equivalent basis

atoms. Naming the two basis atom electron wavefunctions Φ_a and Φ_b, the terms necessary to calculate the bandstructure of ML-TMDs are

$$\langle\Phi_a|H|\Phi_b\rangle = \langle\Phi_b|H|\Phi_a\rangle^* \ , \ \langle\Phi_a|H|\Phi_a\rangle \text{ and } \langle\Phi_b|H|\Phi_b\rangle \ .$$

The terms $\langle\Phi_i|H|\Phi_j\rangle$ are called the self-energy if $i = j$ and the hopping term if $i \neq j$. The self-energy can be interpreted as the energy of an electron at a lattice point compared to the energy at other lattice points, i.e., it is the energy difference between the atomic potentials making up the lattice. In contrast, the hopping term is related to the transition probability between atomic wavefunctions Φ_i and Φ_j. Since only relative energies are relevant in optical experiments, one of the self-energies $\langle\Phi_i|H|\Phi_i\rangle$ can arbitrarily be set to zero. In this case

$$\langle\Phi_b|H|\Phi_b\rangle = 0$$

is chosen.

The lattice of a typical ML-TMD is shown in Figure 1a. The lattice vectors $\vec{a}_1, \vec{a}_2$, which are introduced below, are also drawn. Figure 1b shows the corresponding first Brillouin zone with the reciprocal lattice vectors $\vec{b}_1, \vec{b}_2$. Choosing the coordinate axes as shown in the figures, the vectors can be represented in this basis as

$$\vec{a}_1 = \frac{a}{2}\left(3, \sqrt{3}\right) \quad , \quad \vec{a}_2 = \frac{a}{2}\left(3, -\sqrt{3}\right)$$

$$\vec{b}_1 = \frac{2\pi}{3a}\left(1, \sqrt{3}\right) \quad , \quad \vec{b}_2 = \frac{2\pi}{3a}\left(1, -\sqrt{3}\right).$$

Defining $t = \langle\Phi_a|V(\vec{r} - \vec{R}_i)|\Phi_b\rangle$ the hopping term is calculated to be

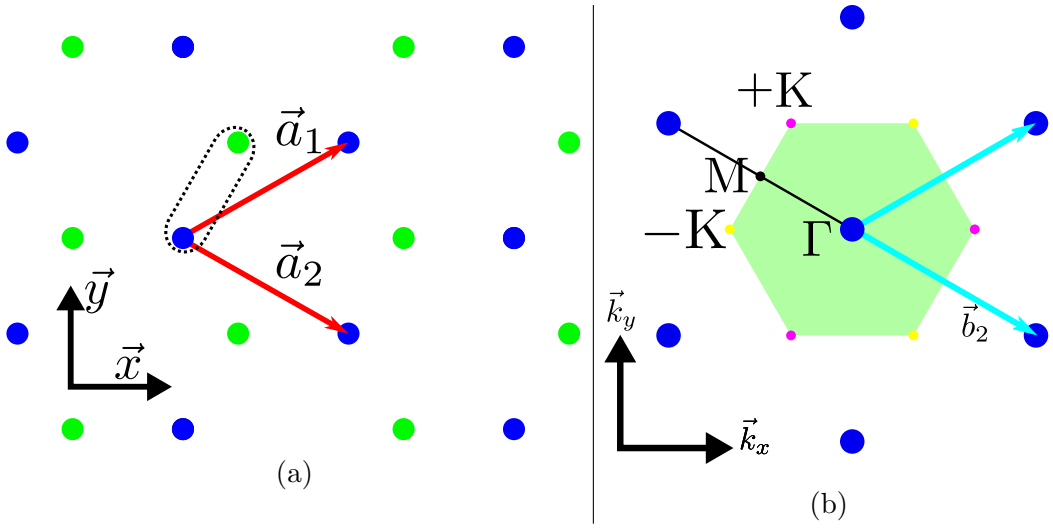

Figure 1: (a) Real-space lattice in ML-TMDs. A blue circle represents a transition metal atom while a green circle represents two chalcogenide atoms separated in the out-of-plane axis. The red arrows are the lattice vectors defining the whole lattice from linear combinations of the two. The dashed region shows a unit cell. (b) Corresponding first Brillouin zone of the reciprocal lattice with reciprocal lattice vectors $\vec{b}_1$ and $\vec{b}_2$. The yellow circles represent the +K points while the magenta colored circles are the −K points.

$$\sum_{NN}\langle\Phi_a|V(\vec{r}-\vec{R}_i)|\Phi_a\rangle e^{i\vec{k}\cdot\vec{R}_i} = t\sum_{NN} e^{i\vec{k}\cdot\vec{R}_i}$$

$$= t\left(e^{i\frac{1}{3}\sqrt{3}k_x a} + e^{i\frac{1}{3}\left(-\frac{\sqrt{3}}{2}k_x a+\frac{3}{2}k_y a\right)} + e^{i\frac{1}{3}\left(-\frac{\sqrt{3}}{2}k_x a-\frac{3}{2}k_y a\right)}\right) =: t\Gamma.$$

Plugging this into the eigenvalue problem in Equation 4 the band structure of the electron is found by solving the determinant equation

$$\det\left(H-\lambda\mathbb{1}\right)=0$$

which, when plugged in results in

$$\det \begin{pmatrix} E_A - \lambda & t\Gamma \\ t\Gamma^* & -\lambda \end{pmatrix} = 0.$$

The eigenenergies are then

$$E_{1/2} = E_A \pm t.$$

The self and hopping term energies are found by fitting the theoretical result to measured bandstructures. The two parameters contributing in this simple model are adjusted until the bandgap and bandwidth are reproduced. Using the values measured through PL and the 4 eV bandwidth of the valence band as reported in [90], the self-energy is obtained as $E_A = 1.08$ eV and the interaction term is $t = 1.50$ eV for molybdenum diselenide ($MoSe_2$). Using these parameters, the explicit bandstructure is calculated and shown in Figure 2a exhibiting the six bandgaps at the $\pm K$ points. Comparing the calculated bandstructure displayed in Figure 2 to the bandstructure calculated by DFT calculations, it is seen that even the simple, completely analytic tight-binding approach captures the energetically degenerate bandgap at the $+K$ and $-K$ valleys but fails to properly capture the behaviour around the Γ point. Projecting this bandstructure along the different crystal symmetry axes a band structure diagram shown in Figure 2b is calculated. The distances between the Γ, M and K points correspond to the relative distances between the points in the reciprocal space.

2.4 Dynamics of Excitons and Trions in ML-TMDs

A well-studied effect of excitons is the formation of an excitonic Rydberg series just below the bandgap. This was found in GaAs bulk crystals at low temperatures [19] and also confirmed for ML-TMDs [81, 91, 92]. This excitonic Rydberg series can already be used to obtain information about the dielectric environment in the crystal

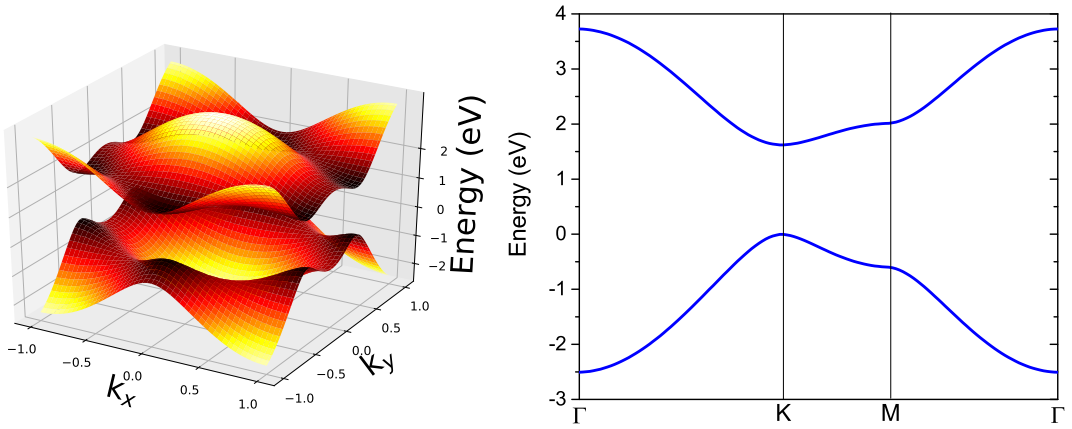

(a) (b)

Figure 2: (a) Two-dimensional bandstructure of $MoSe_2$ calculated from a nearest-neighbor interaction tight-binding model showing the direct bandgap at the K points. (b) Projection of the bandstructure along the major symmetry axes showing the direct gap at the K points but lacking an indirect bandgap around the Γ point.

[91]. Excitons inherit the valley pseudo-spin polarization of their constituent electrons and holes and thus are also restricted and protected within reciprocal space. The valley pseudo-spin dynamics of ML-TMDs are attracting research interest, especially the small valley polarization in ML $MoSe_2$ is still unclear [93].

In a doped crystal lattice or due to defects and impurities in the crystal, excess charges are available, which can bind to excitons forming a three-particle state called trion. Trions are also especially stable in ML-TMDs, having binding energies of ≈ 30 meV in ML $MoSe_2$ and existing up to room temperature. Excitons and trions have been shown to significantly affect the performance of ML-TMD based devices, making a complete understanding of the exciton and trion interactions important for applications [20, 80, 94–96].

The correct characterization of exciton and trion decay dynamics as radiative and non-radiative processes can be challenging because of the interaction with impurity and defect states. Below, excitons are classified as bright and dark excitons. For bright excitons, the momentum of electron and hole matches and radiative recom-

bination of electron and hole is possible. Contrary to a bright exciton, in a dark exciton the electron and hole have different momentum and radiative recombination is only possible through a phonon-assisted recombination process reducing the transition dipole moment of dark excitons. Some of the radiative and non-radiative decay processes for excitons are summarized below [97].

1. Radiative Decay

   The recombination of the electron and hole constituting the exciton and release of a photon. Radiative recombination can only occur when the momentum of electron and hole constituting the electron are matched. In this case, the radiative recombination has been measured to be 150 fs in tungsten diselenide (WSe_2) [98] for bright excitons with near-zero center-of-mass momentum, as predicted by theoretical considerations using Fermis golden rule [97].

2. Trion formation

   An electron or a hole gets captured by an exciton leading to formation of a trion and release of the binding energy. This process was found to happen on a picosecond timescale in $MoSe_2$ and shows strong dependence on the pumping energy. Excitons excited at a higher energy were found to more rapidly (1.6 ps) form trions than those excited at the low-energy wing of the exciton resonance (2.3 ps) [21].

3. Biexciton formation

   The binding of two excitons to form a biexciton and release of the binding energy. Biexcitons are found to have a binding energy of approximately 5 meV for neutral and 20 meV for charged excitons in $MoSe_2$ [62], while the binding energy is between $30-50$ meV in WSe_2. The biexciton relaxation time in WSe_2 was found to be 27 ps, limited by non-radiative decay [99].

4. Inter-valley scattering

   An exciton absorbs a phonon and either the electron or the hole, or both get transferred from the $+K(-K)$ to the $-K(+K)$ valley. Only when both electron and hole scatter to the opposite valley and a spin flip occurs for both of them a bright exciton is formed which can then radiatively decay. Kerr rotation spectroscopy has revealed that in tungsten disulfide (WS_2) intervalley scattering happens on a picosecond timescale and that the scattering behaviour is highly dependent on the excitation energy, i.e. at off-resonant excitation an additional, long-lived component (30 ps) appears in the scattering process while the scattering on the short timescale becomes faster [100]. In WSe_2 the intervalley scattering was observed through polarization-resolved TR-PL revealing a scattering timescale on the order of 10 ps [101].

5. Intra-valley scattering

   An exciton can gain center-of-mass momentum within its valley or a spin-flip of either electron or hole can occur through absorption or emission of a phonon leading to an optically bright exciton becoming a dark exciton. The spin-flip dynamics have been probed in WS_2 through a helicity resolved pump-probe experiment [102]. Excitons become dark when the constituent electron undergoes a spin-flip, which was found to occur on a sub-picosecond timescale. At high temperatures this process becomes faster, confirming that it is a phonon-mediated process [102].

6. Exciton-exciton Auger scattering

   Two excitons scatter through their constituents. An electron (hole) of one exciton transfers energy to an electron or hole of another exciton. One of the two excitons will not be bound anymore while the other exciton recombines.

The process was observed through pump density-dependence measurements in pump-probe experiments on molybdenum disulfide (MoS_2) [103,104], WS_2 [104, 105] and WSe_2 MLs [105].

7. Defect-assisted Auger scattering

   For defect-assisted Auger scattering an electron (hole) constituting an exciton gets captured by a mid-gap defect state. The excess energy gets transferred to the hole (electron) breaking up the exciton. Since the energy difference between the initial and final electron (hole) state is smaller than in the case of direct recombination, the process can be more efficient than exciton-exciton Auger scattering. The process has been observed using pump density-dependence measurements in pump-probe experiments on MoS_2 MLs revealing a fast trapping on the scale of $1 - 2$ ps [106]. The results presented in Section 4 are explained through trion defect scattering on a few picosecond timescale.

8. Defect-assisted exciton-exciton Auger scattering

   This process is a defect-assisted version of exciton-exciton Auger scattering. An electron (hole) of one exciton transfers to a defect state and transfers the excess energy to the hole (electron) of another exciton, breaking it apart.

For trions, the above mentioned processes are largely the same. Instead of trion formation, trions can be transformed into an exciton by phonon-excited upconversion, where a phonon is absorbed breaking apart the trion into an exciton and a free carrier [107].

3 Two-Dimensional Spectroscopy

3.1 Theoretical Background

The nonlinear signals discussed in this dissertation can be understood in the perturbative limit of semi-classical theory [22]. While atoms are considered quantum mechanically, their interaction with electric fields and the electric field is treated classically. In the perturbative limit, the electric fields are low enough that only terms up to a finite order need to be considered in order to generate the observed signal. While the perturbative approach definitely has its limitations, as it fails to correctly predict effects such as Rabi flopping, it is a good framework for the description of second and third-order processes where higher order contributions can be neglected. The nonlinear signals discussed here are only up to the third order and second-order signals from the ML sample were not measured, such that the description here will start with a general treatment of perturbation theory and then go on to introduce the pulse sequence used to generate the measured third order signals. A two-level system will be discussed in detail which is then related to the ML-TMD systems. Although the optical signals measured are from the radiating polarization generated inside the medium, it is sufficient to calculate the quantum states generating the polarization since polarization and quantum state are proportional to each other

$$P_{ij}^{(n)}(t) = N\mu_{ij}\rho_{ij}^{(n)}e^{i\omega_{ij}t}.$$

The n-th order polarization P depends on the density of radiating dipoles N, the transition dipole moment μ_{ij} of transition i, j, the density matrix element $\rho_{ij}^{(n)}$ and radiates a signal at the frequency ω_{ij}.

3.1.1 Density Matrix Formalism

The simplest system to interact with a light-field is a two-level system which has only one ground state and one excited state. If light of wavelength corresponding to the energy difference between the two states is incident onto the system it can be absorbed and excite electrons from the ground state to the excited state. The corresponding atomic wavefunction $|\Psi_a\rangle$ of any combination of ground $|\Psi_g\rangle$ and excited state $|\Psi_e\rangle$ exists with the constraint that $|\Psi_a\rangle$ is normalised.

$$|\Psi_a\rangle = c_g|\Psi_g\rangle + c_e|\Psi_e\rangle \qquad \text{where } |c_g|^2 + |c_e|^2 = 1$$

This picture fails to describe the full possible state space when considering more than a single atom, since all possible states that can be described by an atomic wavefunction are separable, meaning that all atoms are behaving exactly the same. Such a collective state is realized for Dicke states and has been realized experimentally [50, 108–118], but generally is not the case for an interacting system. Instead, in a system consisting of multiple possibly interacting atoms, mixed states are possible, which can no longer be represented as a sum of wavefunctions.

In order to mathematically represent the full state space, a matrix spanned by a set of weighted wavefunctions has to be used

$$\rho_{ij} = \sum_{i,j} c_i c_j^* |\Psi_i\rangle\langle\Psi_j| \quad \text{with } \mathrm{Tr}(\rho) = 1.$$

This so-called density matrix ρ is a hermitian matrix and therefore an observable. Furthermore, for a pure state, it acts as a projection and satisfies $\rho^2 = \rho$ meaning that measuring a pure state in its eigenbasis will not affect the state. A pure state is any state that can be represented by a single wavefunction, i.e. ρ will only have one diagonal entry that is unity while all other entries are zero in its eigenbasis. The

expectation value of an operator A is obtained by calculating the trace of the density matrix multiplied by the operator $\langle A \rangle = \mathrm{Tr}(\rho A)$.

It can be shown that ρ can always be diagonalized when choosing an appropriate basis. However, this is not the interpretation most useful for perturbative nonlinear optics. Instead, ρ will be created from pure wavefunctions such that the diagonal contains only contributions from one state at any time. Then the off-diagonal elements can be interpreted as a coherent superposition between two states. As an example, one can consider the two-level system mentioned above. The corresponding density matrix would be

$$\rho = \sum_{i,j} c_i c_j^* |\Psi_i\rangle\langle\Psi_j| = c_g c_g^* |\Psi_g\rangle\langle\Psi_g| + c_e c_g^* |\Psi_e\rangle\langle\Psi_g| + c_g c_e^* |\Psi_g\rangle\langle\Psi_e| + c_e c_e^* |\Psi_e\rangle\langle\Psi_e|.$$

In the basis $\{|\Psi_g\rangle, |\Psi_e\rangle\}$ the matrix is then represented as

$$\rho = \begin{pmatrix} c_g c_g^* & c_g c_e^* \\ c_e c_g^* & c_e c_e^* \end{pmatrix},$$

with the diagonal elements containing the information about the fraction of the population in states $|\Psi_g\rangle, |\Psi_e\rangle$ and the off-diagonal elements containing information about entanglement between $|\Psi_g\rangle$ and $|\Psi_e\rangle$.

3.1.2 Optical Bloch Equation

The SEQ, which determines the time-evolution of a wavefunction, now needs to be replaced as the equation of motion, since rather than the dynamics of a quantum state the dynamics of an ensemble of quantum states is observed. The result is the

optical Bloch equation (OBE), which is derived from the SEQ. Starting with the SEQ

$$i\hbar\frac{\partial\Psi}{\partial t} = H\Psi \tag{5}$$

and multiplying with the conjugated state Ψ^* from the right

$$i\hbar\frac{\partial\Psi}{\partial t}\Psi^* = H\Psi\Psi^*,$$

the reverse product rule of derivatives can be used such that

$$i\hbar\left[\frac{\partial(\Psi\Psi^*)}{\partial t} - \Psi\frac{\partial\Psi^*}{\partial t}\right] = H\Psi\Psi^*.$$

The second term on the left side is the complex conjugate of the SEQ Equation 5 so it can be replaced by the complex conjugate on the right side of Equation 5. Subtracting this term, the OBE is almost obtained in its typical form

$$i\hbar\frac{\partial(\Psi\Psi^*)}{\partial t} = H\Psi\Psi^* - \Psi\Psi^*H^*.$$

Moving the prefactors to the right side of the equation and replacing $\Psi\Psi^*$ with the density matrix ρ, the OBE is obtained as

$$\dot{\rho} = -\frac{i}{\hbar}[H, \rho].$$

This equation describes the unitary time evolution of an ensemble of quantum states. Instead of the matrix form, the component description is often more useful, since only one or two components of the matrix need to be calculated to explain an experimentally observed signal

$$\dot{\rho}_{mn} = -\frac{i}{\hbar}\sum_k \left(H_{ik}\rho_{kj} - \rho_{ik}H_{kj}\right). \tag{6}$$

To include dissipative phenomena such as relaxation and decoherence, an additional term is added into the OBE phenomenologically

$$\dot{\rho}_{mn} = -\frac{i}{\hbar}\sum_{j}\left(H_{mj}\rho_{jn} - \rho_{mj}H_{jn}\right) - \Gamma_{mn}\rho_{mn}, \tag{7}$$

where Γ_{mn} are the components of the relaxation operator describing the dissipation dynamics. The relaxation operator consists of two main parts

$$\Gamma_{mn} = \frac{1}{2}(\gamma_n + \gamma_m) + \gamma_{nm}^{\text{dephasing}},$$

where γ_n, γ_m are the population decay rates and $\gamma_{nm}^{\text{dephasing}}$ is the rate of dephasing that is not associated with any population transfer, for example from dipoles having different eigenfrequencies or elastic collision between electrons.

In the perturbative approach, H is split into the free atom part H_0 as well as a term that is due to interaction with an electric field V. The basis for the theoretical treatment is always chosen as the eigenbasis of H_0. Then H_0 is diagonal and the eigenvalues are the energy states of the atom with energy E_i. Before solving the OBE in Equation 7, the commutator is inspected more closely and it is noted that $[A+B, C] = [A, C] + [B, C]$ due to the commutator satisfying distributivity. The free atom term is therefore

$$[H_0, \rho] = \sum_{i,j}\sum_{k}(H_{0,ik}\rho_{kj} - \rho_{ik}H_{kj}) = \sum_{i,j}\sum_{k}(E_i\rho_{ij} - \rho_{ij}E_j) = \sum_{i,j}(E_i - E_j)\rho_{ij}. \tag{8}$$

Defining the transition frequency between states i, j

$$\omega_{ij} = \frac{E_i - E_j}{\hbar}\ ,\ \Omega = \sum_{ij}\omega_{ij} \tag{9}$$

the matrix Ω is constructed. Plugging in the result of Equation 8 and the definition in Equation 9 into Equation 7 the equation is modified to

$$\dot{\rho} = -i\Omega\rho - \frac{i}{\hbar}\left[V, \rho\right] - \Gamma\left(\rho - \rho^{\mathrm{eq}}\right). \tag{10}$$

At this point the equation is expanded in form of a perturbative series, since it generally can not be solved analytically. The zeroth-order term is

$$\dot{\rho}^{(0)} = -i\Omega\rho^{(0)} - \Gamma\left(\rho^{(0)} - \rho^{\mathrm{eq}}\right).$$

This equation describes a system that will relax back into the equilibrium state ρ^{eq} from whichever state $\rho^{(0)}$ it started in with a relaxation rate given by the matrix Γ while oscillating between states ρ_{ij} with the transition frequency ω_{ij}.

For higher order terms the interaction part of the commutator is considered and the equation is written as

$$\dot{\rho}^{(n)} = -(i\Omega + \Gamma)\rho^{(n)} - \frac{i}{\hbar}[V, \rho^{(n-1)}].$$

This equation can be integrated which yields the n-th order density matrix as a function of the $(n-1)$-th order density matrix

$$\dot{\rho}^{(n)}(t) = -\frac{i}{\hbar}\int_{-\infty}^{t}\left[V(t'), \rho^{(n-1)}\right] e^{(i\Omega+\Gamma)(t'-t)}dt'. \tag{11}$$

Plugging in arbitrary electric fields and initial density matrix elements $\rho^{(0)}$, the n-th order density matrix can at least numerically be calculated.

In practice, the electric field and density matrix are often approximated by sufficiently simple functions and initial conditions such that Equation 11 can be solved analytically.

3.1.3 Double-Sided Feynman Diagrams

In order to simplify the presentation of perturbative series, a convenient representation for summarizing the terms of the perturbation expansion called double-sided Feynman diagrams has been developed [22]. These diagrams contain information about the electric fields as well as the density matrix elements ρ_{ij} involved in the interaction. There are four different kinds of vertices in Feynman diagrams, corresponding to non-conjugated / conjugated pulses exciting / relaxing the sample. The possible vertices in Feymnam diagrams are shown in Figure 3. The corresponding changes to the density matrix are

(a) $\rho_{jk}^{(n)} = i\frac{\mu_{ij}}{2\hbar}e^{i\vec{k}_n\cdot\vec{r}}\int_{-\infty}^{t} E_n(t')e^{-i\omega_n t'}e^{-i\Omega_{jk}(t-t')}\rho_{ik}^{(n-1)}(t')dt'$

(b) $\rho_{jk}^{(n)} = i\frac{\mu_{ij}}{2\hbar}e^{-i\vec{k}_n\cdot\vec{r}}\int_{-\infty}^{t} E_n^*(t')e^{i\omega_n t'}e^{-i\Omega_{jk}(t-t')}\rho_{ik}^{(n-1)}(t')dt'$

(c) $\rho_{il}^{(n)} = -i\frac{\mu_{kl}}{2\hbar}e^{-i\vec{k}_n\cdot\vec{r}}\int_{-\infty}^{t} E_n^*(t')e^{i\omega_n t'}e^{-i\Omega_{il}(t-t')}\rho_{ik}^{(n-1)}(t')dt'$

(d) $\rho_{il}^{(n)} = -i\frac{\mu_{kl}}{2\hbar}e^{i\vec{k}_n\cdot\vec{r}}\int_{-\infty}^{t} E_n(t')e^{-i\omega_n t'}e^{-i\Omega_{il}(t-t')}\rho_{ik}^{(n-1)}(t')dt'$

with the frequency Ω_{ij} defined through the transition frequency $\omega_{ij} = \omega_i - \omega_j$ and the component Γ_{ij} of the relaxation operator as

$$\Omega_{ij} = \omega_{ij} - i\Gamma_{ij} \tag{12}$$

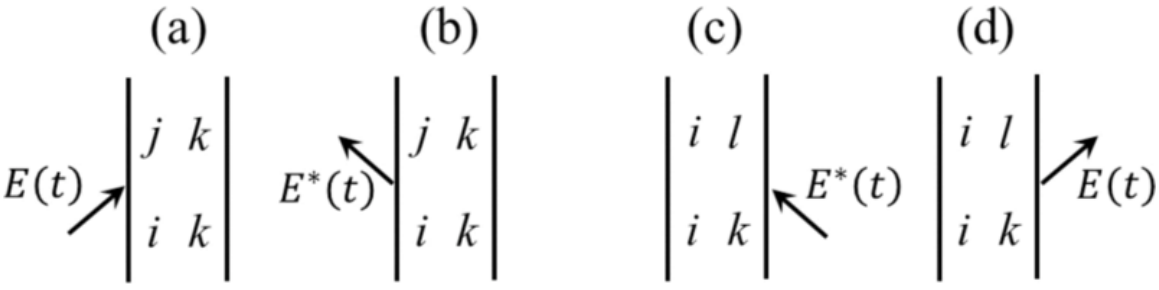

Figure 3: Possible vertices in a Feynman diagram, reproduced with permission from [1].

By convention, time evolves in the upward direction. An arrow pointing towards the vertex means a photon is absorbed and the system is further excited while an arrow pointing away from the vertex means that the system is emitting a photon and relaxes. An arrow pointing to the left means that the electric field interacting is a conjugated field while an arrow pointing to the right corresponds to a non-conjugated field. The indices inside the diagram correspond to the entries of the density matrix. Each interaction with a field changes the system by changing one index of the density matrix, in agreement to the perturbation expansion derived in Section 3.1.2.

For a complete treatment of a nonlinear signal all possible Feynman diagrams need to be considered making the required calculations lengthy. However, due to time-ordering and phase-matching conditions typically the number of relevant Feynman diagrams contributing to any signal of interest is significantly reduced.

3.1.4 Four-Wave Mixing

The coherence dynamics of ML semiconductors happen on a timescale ranging from hundreds of femtoseconds to a few picoseconds for encapsulated samples. Therefore, ultrafast spectroscopic techniques are required to resolve their dynamics.

In the case of degenerate TI-FWM, the signal is generated by nonlinear light-matter interaction of three pulses with the same frequency.

For non-collinear excitation, the process for generating a FWM signal is shown in Figure 4. A first pulse A with a wavevector $-\vec{k}_A$ interacts with the sample, inducing a linear polarization, which in the perturbative approximation corresponds to moving the system from the ground state to a coherent superposition between ground and excited states. After a time delay τ, a second pulse B with wavevector $\vec{k}_B$ is incident on the sample and converts the polarization into a population. Since the two pulses are non-collinear, the relative phase of the electric field of pulse B with respect to

the polarization created by pulse A varies across the illuminated area. The generated population is maximum when the two interfere constructively and minimum when they interfere destructively. This process forms a population grating where the maximum and minimum population density of the grating depends on the time delay τ between pulses A and B as well as the coherence time of the superposition of ground and excited state, which is related to the decay rate Γ_{ij} in Equation 10. In order to measure the coherence time, a third pulse C with wavevector $\vec{k}_C$ is incident on the sample after time delay T creating a polarization and scattering off the grating created by pulses A and B, probing the population in the maximum and minimum regions of the grating. The signal created in this way is highly directional due to the phase-matching conditions between the wavevectors of beams A, B, C and therefore largely background free.

One problem related to TI-FWM spectroscopy is the distinction between a homogeneously or inhomogeneously broadened sample. From solving the OBE, there is a factor of two difference in the measured dephasing rate from TI-FWM between a homogeneously broadened and inhomogeneously broadened sample [119]. An even larger problem arises in the case of intermediate inhomogeneous broadening, where neither the homogeneous nor the inhomogeneous limit holds. The issue of distinguishing between different types of broadening in a system can be circumvented using 2DCS.

The TI-FWM signal presented here depends on the two time delays τ and T as well as the ordering of the pulses. During the first time delay the system evolves coherently while during the second time delay the system is in a population state evolving incoherently. Therefore the coherent and incoherent dynamics are associated with the time delays τ and T, respectively. Changing the pulse ordering such that the conjugated pulse A arrives after pulses B and C double-quantum spectra can be obtained [120, 121]. For a two-level system, there is no double-quantum signal,

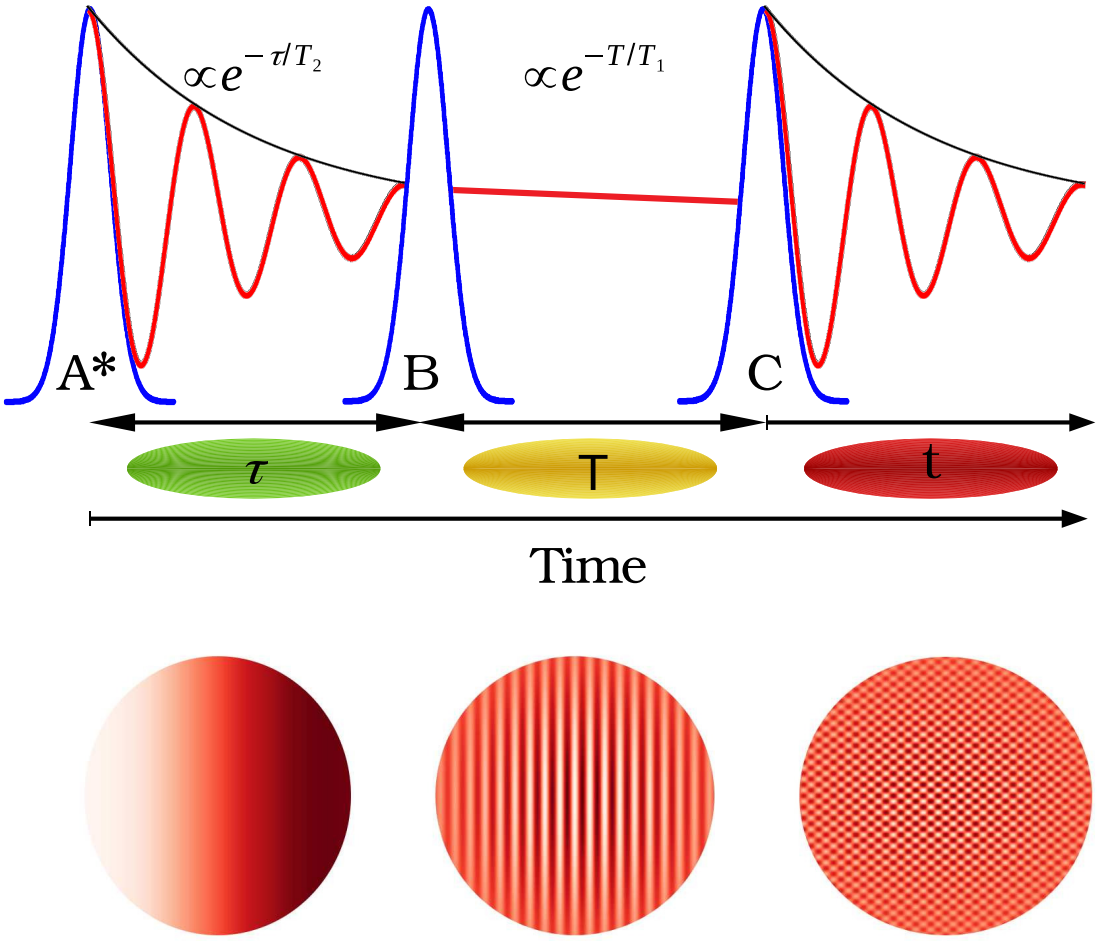

Figure 4: top: Pulse ordering and corresponding time delays used in 2DCS. bottom: Phase and population distribution at the focus after interaction of the sample with one, two and three pulses.

however, interactions can lead to a modified energy level scheme which allows for a double-quantum signal even in two-level systems [50,51,122,123]. This makes double-quantum 2DCS a powerful tool for investigating many-body effects.

Using different light polarization configurations, different resonances can selectively be excited or made inaccessible which allows for the isolation of weak signals, such as the signal due to biexcitons in semiconductor quantum wells or ML-TMDs [54,62].

Different approaches can be used to isolate the signal from the background. For

non-collinear approaches to FWM spectroscopy, wavevector selection is used [124]. However, to be able to perform FWM spectroscopy at the diffraction limit, it is necessary to have the excitation and signal beams copropagate in order to get a tight focus. For the collinear approach, an approach based on the detection of a frequency modulated signal has been developed more recently, which will also be discussed and was used for measuring the coherence in encapsulated MLs [32].

Phase-Matching

Wavevector selection is used to extract the signal from the background in the non-collinear excitation scheme and can be understood by direct inspection of the mixing of electric fields. In the non-collinear 2DCS setup, the three beams interacting with the sample all have different momenta. The fields mix through the susceptibility leading to cancellation of the signal in most cases and constructive interference in only certain directions. The four-wave mixing electric field is written as

$$\begin{aligned} E_{\mathrm{FWM}} \propto & E_A E_B E_C \\ & \propto \left(e^{-i\left(\vec{k}_A \cdot \vec{r} - \omega_A t_A\right)} + c.c. \right) \\ & \quad \times \left(e^{-i\left(\vec{k}_B \cdot \vec{r} - \omega_B t_B\right)} + c.c. \right) \\ & \quad \times \left(e^{-i\left(\vec{k}_C \cdot \vec{r} - \omega_C t_C\right)} + c.c. \right). \end{aligned} \tag{13}$$

Expanding the right-hand side it is seen that the phase-matching directions are along $\vec{k}_s = \pm\vec{k}_A \pm \vec{k}_B \pm \vec{k}_C$. In the non-collinear setup used throughout this work, the phase-matching direction $\vec{k}_s = -\vec{k}_A + \vec{k}_B + \vec{k}_C$ is used fixing pulse A to interact as a conjugated pulse while beams B and C act as non-conjugate pulses.

Since the background in a FWM experiment is mostly scatter and luminescence which both radiate homogeneously, the nonlinear signal along the phase-matching

direction will be stronger than the background in this direction making it possible to perform FWM spectroscopy even in the presence of strong background and, more importantly, with fully degenerate excitation conditions used for resonant enhancement of the FWM signal.

Phase-matching for signal extraction can only be used when the sample size is larger than the wavelength of the light used to interrogate the sample since otherwise no population grating can be formed from the interference of the pulses. In the case of ML-TMDs, which are typically between a few to hundreds of micrometers in size, phase-matching happens in all samples.

When performing 2DCS at the diffraction limit, wavevector selection can not be used since all excitation beams are copropagating and the FWM signal will therefore be copropagating with the excitation beams as well. To extract the signal from the background in this case, each beam is tagged with a unique phase modulation frequency. In the discussion of Equation 13, so far only the terms containing the fields wavevector $\vec{k}_i$ was used. Instead of the mixing of the wavevectors $\vec{k}_i$, the phase of the signal is modulated by the rapidly varying field frequencies ω_i and the pulse arrival times t_i. In the collinear setup, the field frequencies (100s of THz) are shifted by a comparably slow (10s of MHz) radio frequency. The RF mixing leads to a modulation of the signal, in the case of the PL detected collinear setup used in Appendix A the detection frequency of the signal is chosen as

$$\omega_S = -\omega_A + \omega_B + \omega_C - \omega_D.$$

The PL detected collinear setup is a four-pulse experiment, such that Equation 13 needs to be expanded by a fourth exponential

$$
\begin{aligned}
E_{\text{collinear}} &\propto E_A E_B E_C E_D \\
&\propto \left(e^{-i\left(\vec{k}_A\cdot\vec{r}-\omega_A t_A\right)}+c.c.\right)\left(e^{-i\left(\vec{k}_B\cdot\vec{r}-\omega_B t_B\right)}+c.c.\right) \\
&\times \left(e^{-i\left(\vec{k}_C\cdot\vec{r}-\omega_C t_C\right)}+c.c.\right)\left(e^{-i\left(\vec{k}_D\cdot\vec{r}-\omega_D t_D\right)}+c.c.\right).
\end{aligned}
$$

The signal frequency ω_S is fed to a lock-in amplifier as the reference frequency and the signal can be extracted from the background.

FWM Signal from a Homogeneously Broadened Two-Level System

Using wavevector selection and implementing the restrictions from pulse-ordering, only two Feynman diagrams contribute to the FWM signal from a two-level system in a three pulse experiment as shown in Figure 4. In the diagrams shown, the signal propagates in the phase-matching direction $\vec{k}_S = -\vec{k}_A+\vec{k}_B+\vec{k}_C$ such that pulse A acts as a conjugated pulse. The time-ordering is chosen such that A arrives first, followed by beams B and C. The remaining Feynman diagrams are shown in Figure 5. The coherence time can be measured by measuring the dynamics of any superposition state denoted by 10 or 01 in the diagram, i.e. the dynamics during delay τ or t.

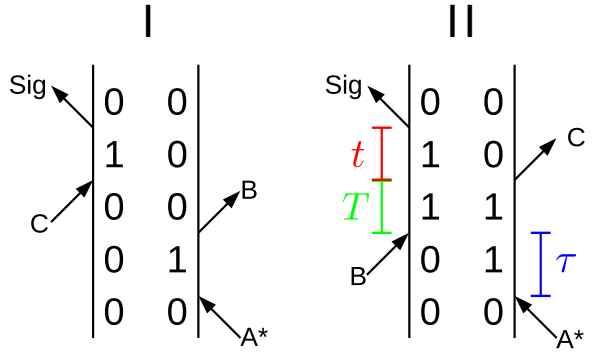

Figure 5: Feynman diagrams in a three-pulse experiment with time-ordering A, B, C from a two-level system contributing to the signal in the phase-matching direction $\vec{k}_S = -\vec{k}_A + \vec{k}_B + \vec{k}_C$

.

Applying the rules for vertices in Feynman diagrams the FWM signal from diagram I is

$$\begin{aligned}\rho^{(3)}_{10,I}(t) = &- i\frac{\mu_{01}^3}{8\hbar^3}e^{i(-\vec{k}_A+\vec{k}_B+\vec{k}_C)\cdot\vec{r}} \\ &\times \int_{-\infty}^{t} E_C(t')e^{-i\omega_C t'}e^{-i\Omega_{10}(t-t')} \\ &\times \int_{-\infty}^{t'} E_B(t'')e^{-i\omega_B t''}e^{-i\Omega_{10}(t'-t'')} \\ &\times \int_{-\infty}^{t''} E_A(t''')e^{-i\omega_B t'''}e^{-i\Omega_{10}(t''-t''')}\rho^{(0)}_{00}(t''')dt'''dt''dt'.\end{aligned}$$

For now, it is assumed that the pulse duration is much shorter than the laser pulse width. The treatment for a finite pulse is delayed to Section 5.3.2. The approximation of short pulses can be written mathematically as a Dirac-δ function, i.e. $E_i(t) = E_i\delta(t-t_i)$ where index i denotes pulse i and t_i is the arrival time of pulse i. Implementing this approximation and using the fact that $\int_{-\infty}^{x}\delta(x-x_0) = \Theta(x-x_0)$ with the Heaviside step function $\Theta(x) = \begin{cases} 0\ , & x<0 \\ 1\ , & x\geq 0 \end{cases}$, the integration can be performed analytically

$$\begin{aligned}\rho^{(3)}_{10,I}(t) = &- i\frac{\mu_{01}^3}{8\hbar^3}e^{i(-\vec{k}_A+\vec{k}_B+\vec{k}_C)\cdot\vec{r}}e^{-i(-\omega_A t_A+\omega_B t_B+\omega_C t_C)}E_A^*E_BE_C \\ &\times \Theta(t_B-t_A)\Theta(t_C-t_B)\Theta(t-t_C)e^{-i\Omega_{10}(t-t_C)}e^{-i\Omega_{11}(t_C-t_B)}e^{-i\Omega_{01}(t_B-t_A)}\rho^{(0)}_{00}(t_A).\end{aligned}$$

Assuming that $\rho^{(0)}_{00}(t) = const. = 1$ and rewriting the pulse arrival times in terms of delay times defined as $\tau = t_B - t_A$, $T = t_C - t_B$ and $t = t - t_C$, the density matrix

element contributing to the FWM signal is obtained in the time-domain as

$$\begin{aligned}\rho^{(3)}_{10,I}(t,T,\tau) =& -i\frac{\mu_{01}^3}{8\hbar^3}e^{i(-\vec{k}_A+\vec{k}_B+\vec{k}_C)\cdot\vec{r}}e^{-i(-\omega_A t_A+\omega_B t_B+\omega_C t_C)}E_A^* E_B E_C \\ &\times \Theta(\tau)\Theta(T)\Theta(t)e^{-i\Omega_{10}t}e^{-i\Omega_{11}T}e^{-i\Omega_{01}\tau}. \end{aligned} \tag{14}$$

Taking the FT of this expression, the frequency response is found to be

$$\begin{aligned}\rho^{(3)}_{10,I}(\omega_t,\omega_T,\omega_\tau) =& -i\frac{\mu_{01}^3}{8\hbar^3}e^{i(-\vec{k}_A+\vec{k}_B+\vec{k}_C)\cdot\vec{r}}e^{-i(-\omega_A t_A+\omega_B t_B+\omega_C t_C)}E_A^* E_B E_C \\ &\times \frac{1}{\sqrt{2\pi}^3}\int_{-\infty}^{\infty}d\tau\int_{-\infty}^{\infty}dT\int_{-\infty}^{\infty}dt\ \Theta(\tau)\Theta(T)\Theta(t) \\ &\times e^{-i\omega_t t}e^{-i\Omega_{10}t}e^{-i\omega_T T}e^{-i\Omega_{11}T}e^{-i\omega_\tau\tau}e^{-i\Omega_{01}\tau} \\ =&\frac{\mu_{01}^3}{16\sqrt{2}\pi^{\frac{3}{2}}\hbar^3}e^{i(-\vec{k}_A+\vec{k}_B+\vec{k}_C)\cdot\vec{r}}e^{-i(-\omega_A t_A+\omega_B t_B+\omega_C t_C)}E_A^* E_B E_C \\ &\times \frac{1}{\Omega_{10}+\omega_t}\frac{1}{\Omega_{11}+\omega_T}\frac{1}{\Omega_{01}+\omega_\tau}. \end{aligned}$$

Repeating this calculation for diagram II, the frequency response for the second Feynman diagram contributing to the signal in the phase-matching direction $\vec{k}_S$ is

$$\begin{aligned}\rho^{(3)}_{10,II}(\omega_t,\omega_T,\omega_\tau) =&\frac{\mu_{01}^3}{16\sqrt{2}\pi^{\frac{3}{2}}\hbar^3}e^{i(-\vec{k}_A+\vec{k}_B+\vec{k}_C)\cdot\vec{r}}e^{-i(-\omega_A t_A+\omega_B t_B+\omega_C t_C)}E_A^* E_B E_C \\ &\times \frac{1}{\Omega_{10}+\omega_t}\frac{1}{\Omega_{00}+\omega_T}\frac{1}{\Omega_{01}+\omega_\tau}. \end{aligned}$$

The total signal in the phase-matching direction $\vec{k}_S$ is then the sum of the two individual contributions

$$\rho^{(3)}_{10,\text{tot}} = \rho^{(3)}_{10,I} + \rho^{(3)}_{10,II}.$$

To further analyze this result, Ω_{ij} is replaced by the transition frequency ω_{ij} and

relaxation rate Γ_{ij} associated with the respective transitions according to Equation 12

$$\rho^{(3)}_{10,I}(\omega_t,\omega_T,\omega_\tau) = \frac{\mu_{01}^3}{16\sqrt{2}\pi^{\frac{3}{2}}\hbar^3} e^{i(-\vec{k}_A+\vec{k}_B+\vec{k}_C)\cdot\vec{r}} e^{-i(-\omega_A t_A+\omega_B t_B+\omega_C t_C)} E_A^* E_B E_C \times \frac{1}{\omega_{10}-i\Gamma_{10}+\omega_t}\frac{1}{-i\Gamma_{11}+\omega_T}\frac{1}{\omega_{01}-i\Gamma_{01}+\omega_\tau}$$

and

$$\rho^{(3)}_{10,II}(\omega_t,\omega_T,\omega_\tau) = \frac{\mu_{01}^3}{16\sqrt{2}\pi^{\frac{3}{2}}\hbar^3} e^{i(-\vec{k}_A+\vec{k}_B+\vec{k}_C)\cdot\vec{r}} e^{-i(-\omega_A t_A+\omega_B t_B+\omega_C t_C)} E_A^* E_B E_C \times \frac{1}{\omega_{10}-i\Gamma_{10}+\omega_t}\frac{1}{-i\Gamma_{00}+\omega_T}\frac{1}{\omega_{01}-i\Gamma_{01}+\omega_\tau}.$$

The transition frequencies of a population are zero, since $\omega_{00} = \omega_0 - \omega_0 = 0 = \omega_{11}$ and were therefore dropped in the equations above. From the above two equations the shape of a three-dimensional spectrum can be readily read off. In the case of the two-level system discussed here, there will be one peak on the $\omega_T = 0$ axis. The peak is a sum of two peaks, one with width Γ_{11} and the other with a width of Γ_{00} along the ω_T axis. The peak is at the location ω_{10} with a width Γ_{10} along the ω_t axis and at $\omega_{01} = -\omega_{10}$ with width $\Gamma_{01} = \Gamma_{10}$ on the ω_τ axis. An example three-dimensional spectrum is shown in Figure 6 for a homogeneously broadened system. The parameters used are $\Gamma_{11} = \Gamma_{00} = 7.2$ meV, $\Gamma_{01} = 3.6$ meV, $\omega_{10} = 1620$ meV.

The figure exhibits the typical Lorentzian star shape in all three dimensions. The solid (semi-transparent) red isosurfaces are drawn at a value of 30 % (10 %) of the maximum peak amplitude. The projection of the spectrum onto the x-y plane, corresponding to a rephasing spectrum as recorded during the course of this dissertation also exhibits a Lorentzian star shape. The contour spacing is 5 % of the maximum peak amplitude.

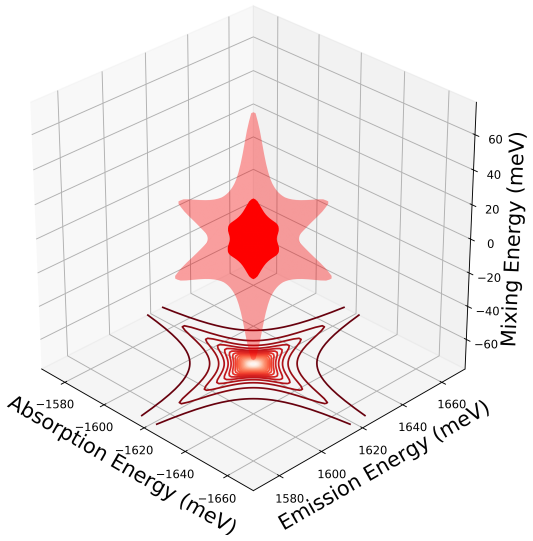

Figure 6: Three-dimensional spectrum of a homogeneously broadened system and the projection onto the x-y plane showing the corresponding two-dimensional rephasing spectrum.

FWM Signal from an Inhomogeneously Broadened Two-Level System

Although the exponential decay processes involved in electronic relaxation will lead to a homogeneously broadened lineshape, different effects can lead to inhomogeneous broadening, which will change the resonance shape. In atomic vapors thermal broadening can lead to a distribution of absorption and emission energies of individual atoms as seen in the laboratory frame. In semiconductors, differences in the local dielectric environment lead to a distribution of dipole eigenenergies leading to a similar broadening of the resonance as thermal broadening of atomic vapors. However, in semiconductors this broadening is often dominating even at low temperatures, making an explicit treatment of the broadening necessary for a full understanding of the FWM signal.

For an inhomogeneously broadened two-level system the same Feynman diagrams as before contribute to the signal, i.e., diagrams I and II in Figure 5. The broadening is introduced assuming a Gaussian distribution with center frequency ω_{10}^{c} and width

$\delta\omega$, given by the function

$$g(\omega_{10}) = \frac{1}{\sqrt{2\pi}\delta\omega} e^{-\frac{(\omega_{10}-\omega_{10}^c)^2}{2\delta\omega^2}}.$$

To include the broadening in the calculation of the frequency response of the density matrix elements, the broadening is introduced in the time-domain. For the contribution from diagram II, the resulting equation is

$$\begin{aligned}\rho^{(3)}_{10,II}(\tau,T,t) = &- i\frac{\mu_{01}^3}{8\hbar^3} e^{i(-\vec{k}_A+\vec{k}_B+\vec{k}_C)\cdot\vec{r}}\Theta(t)\Theta(T)\Theta(\tau)e^{-i(-\omega_A t_A+\omega_B t_B+\omega_C t_C)}E_A^* E_B E_C \\ &\times \int_0^\infty e^{-i\Omega_{10}t}e^{-i\Omega_{11}T}e^{-i\Omega_{01}\tau}g(\omega_{10})d\omega_{10}\end{aligned}$$

where the integration over ω_{10} only runs over positive frequencies to avoid double-counting. Plugging in the definition of $\Omega_{ij} = \omega_{ij} - i\Gamma_{ij}$ from Equation 12 the equation is rewritten as

$$\begin{aligned}\rho^{(3)}_{10,II}(\tau,T,t) = &- i\frac{\mu_{01}^3}{\sqrt{2\pi}\delta\omega 8\hbar^3} e^{i(-\vec{k}_A+\vec{k}_B+\vec{k}_C)\cdot\vec{r}}\Theta(t)\Theta(T)\Theta(\tau)e^{-i(-\omega_A t_A+\omega_B t_B+\omega_C t_C)} \\ &\times E_A^* E_B E_C \int_0^\infty e^{-i(\omega_{10}-i\Gamma_{10})t}e^{-i(-i\Gamma_{11})T}e^{-i(-\omega_{10}-i\Gamma_{01})\tau}e^{-\frac{(\omega_{10}-\omega_{10}^c)^2}{2\delta\omega^2}}d\omega_{10}.\end{aligned}$$

Isolating only the terms containing ω_{10} under the integral and expanding and recollecting the binomial terms the equation is rewritten as

$$\begin{aligned}\rho^{(3)}_{10,II}(\tau,T,t) = &- i\frac{\mu_{01}^3}{\sqrt{2\pi}\delta\omega 8\hbar^3} e^{i(-\vec{k}_A+\vec{k}_B+\vec{k}_C)\cdot\vec{r}}\Theta(t)\Theta(T)\Theta(\tau)e^{-i(-\omega_A t_A+\omega_B t_B+\omega_C t_C)} \\ &\times E_A^* E_B E_C e^{-\Gamma_{10}(t+\tau)-\Gamma_{00}T}e^{-\frac{1}{2}\delta\omega^2(t-\tau)^2+i(\omega_{10}-\omega_{10}^c)(t-\tau)}.\end{aligned} \tag{15}$$

A better interpretation of this result is possible by defining the new temporal variables $\tau' = t - \tau$ and $t' = t + \tau$, which are the diagonal and cross-diagonal directions in a

2D time-domain spectrum. The Equation 15 is then

$$\rho^{(3)}_{10,II}(\tau,T,t) = -i\frac{\mu_{01}^3}{\sqrt{2\pi}\delta\omega 8\hbar^3}e^{i(-\vec{k}_A+\vec{k}_B+\vec{k}_C)\cdot\vec{r}}\Theta(t'-\tau')\Theta(T)\Theta(\tau'+t')e^{-i(-\omega_A t_A+\omega_B t_B+\omega_C t_C)}$$
$$\times E_A^* E_B E_C e^{-\Gamma_{10}t'-\Gamma_{00}T}e^{-\frac{1}{2}\delta\omega^2\tau'^2+i(\omega_{10}-\omega_{10}^c)\tau'}.$$

In this form the homogeneous linewidths Γ_{10} and Γ_{00} can unambiguously be separated from the inhomogeneous linewidth $\delta\omega$. While the homogeneous linewidths are found along the t' and T directions, the inhomogeneous linewidth is disentangled from the homogeneous linewidths and can be found by measuring the linewidth along the τ' direction. However, the homogeneous and inhomogeneous linewidth are not completely separated along the t' and τ' axes because the step functions contain both time axes in an inseparable way. The step functions ensure that causality induced from the pulse ordering is satisfied [125].

In the case of weak inhomogeneous broadening $\delta\omega = 0$ and the homogeneously broadened case is recovered. For strong inhomogeneous broadening, i.e. $\delta\omega >> \Gamma_{10} \wedge \delta\omega >> \Gamma_{11}$, the diagonal direction contains the information about inhomogeneous broadening while the cross-diagonal direction depends only on the homogeneous broadening. For the case of intermediate broadening, the homogeneous and inhomogeneous linewidths mix in the diagonal and cross-diagonal directions. A detailed lineshape analysis of 2D spectra can be found in [125]. For comparison to the previously derived homogeneously broadened case, a 2D spectrum is generated with the same linewidth parameters $\Gamma_{11} = \Gamma_{00} = 7.6$ meV, $\Gamma_{10} = 3.6$ meV, $\omega_{10} = 1620$ meV and an inhomogeneous broadening of $\delta\omega = 30$ meV. The resulting spectrum is shown in Figure 7 and exhibits an elongation along the diagonal direction while the cross-diagonal direction is not as broad as in the homogeneously broadened case. The broadening along the diagonal direction is mostly related to the inhomogeneous

broadening $\delta\omega$ while the broadening along the cross-diagonal direction is related to the homogeneous linewidth Γ_{10}. However, comparing the spectrum to the homogeneously broadened case, it is seen that even with the same homogeneous linewidth parameters, the inhomogeneous broadening leads to an apparent decrease of the linewidth in the cross-diagonal direction. This highlights the importance of using 2DCS or complementing TI-FWM with other methods to measure FWM signals. In 2DCS homogeneous and inhomogeneous case are distinguishable from the peak shape such that the material can be correctly characterized and the homogeneous linewidth can be extracted in the presence of arbitrary inhomogeneity [125].

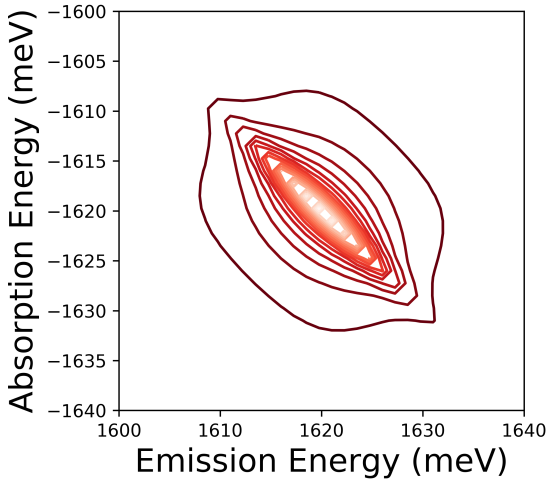

Figure 7: Inhomogeneously broadened 2D spectrum using the same linewidth parameters as in Figure 6 and an inhomogeneous broadening of 30 meV. Each contour corresponds to a difference of 5 % of the maximum amplitude in the spectrum.

3.1.5 Two-Dimensional Coherent Spectroscopy

As mentioned in Section 3.1.4, an inherent problem of TI-FWM spectroscopy lies in the correct characterization of samples into homogeneously or inhomogeneously broadened systems. For the intermediate case of a slightly inhomogeneously broadened system the dephasing rate can not reliably be obtained by TI-FWM only. To

circumvent the requirement of assuming either case and in order to gain access to the dephasing rate in all systems, 2DCS scans two time delays to generate a two-dimensional frequency map. From the frequency map the homogeneous and inhomogeneous linewidths can directly be read off along the cross-diagonal and diagonal directions, respectively as discussed in Section 3.1.4. Furthermore, a theory for measuring the homogeneous and inhomogeneous linewidths in the case of all kinds of inhomogeneity has been developed, such that it is possible to measure the dephasing time in all samples by simultaneously measuring the diagonal and cross-diagonal linewidths in a two-dimensional spectrum [125].

The basic idea of 2DCS can be understood as correlating a signal as a function of two time delays. In the case of S_I scans, the absorption and emission energy of a system can be found. A resulting S_I 2D spectrum for a homogeneously broadened system is seen in Figure 8a. There is one Lorentzian peak with typical star shape, elongated along the emission and absorption frequency axes. The width along the cross-diagonal axis relates to the homogeneous broadening while the width in the diagonal direction is related to the inhomogeneous broadening. Even though the excitation source for obtaining such a spectrum may be broadband, since there is only one resonator, only one frequency gets absorbed and reemitted. In the case of inhomogeneous broadening, different dipoles have different eigenenergies. Therefore, each dipole absorbs and emits at a different frequency and although each dipole generates the same homogeneously broadened spectrum, the peak of an inhomogeneously broadened system becomes elongated along the diagonal axis, as shown in Figure 8b. For the case presented, Gaussian broadening according to the envelope distribution shown in Figure 8c is used. This highlights how the inhomogeneous distribution of homogeneously broadened emitters generates an inhomogeneously broadened peak elongated along the diagonal direction. Even if it may seem like the homogeneous

linewidth may not readily be read off the spectrum anymore, it was shown in Section 3.1.4 that for strongly inhomogeneously broadened spectra, the homogeneous and inhomogeneous linewidths become independent and the homogeneous broadening related to the dephasing time is simply the width along the cross-diagonal direction while the inhomogeneous broadening can be obtained by measuring the width along the diagonal direction [125].

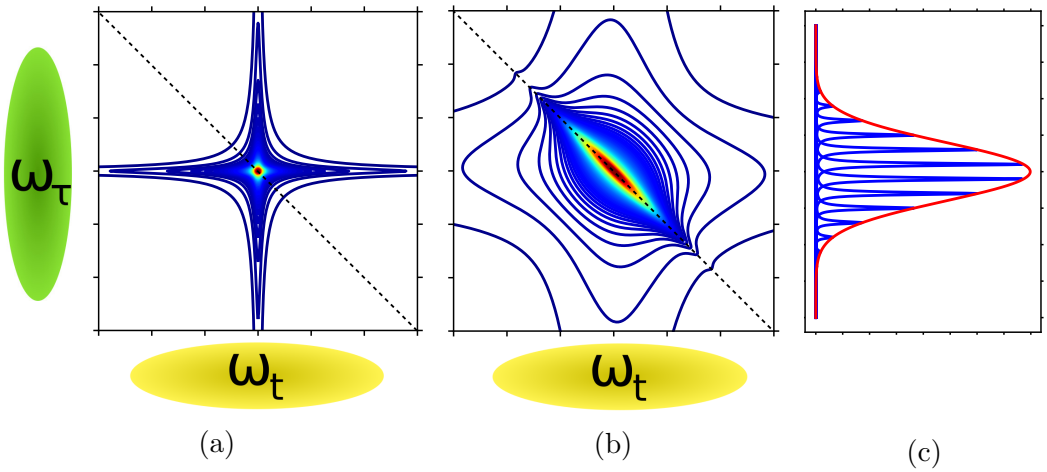

Figure 8: (a) 2D Spectrum of a purely homogeneously broadened system. (b) An inhomogeneously broadened system with inhomogeneous:homogeneous broadening ratio 2:1 exhibiting elongation along the diagonal direction. (c) The distribution of homogeneous emitters along the diagonal axis projected onto the absorption frequency axis ω_τ.

For the intermediate case of a slightly inhomogeneously broadened system the resulting spectrum needs to be analyzed along both the diagonal and cross-diagonal axes simultaneously since coupling between the two broadening mechanisms leads to a mixing of the broadening in the diagonal and cross-diagonal directions [125].

Phase-Cycling

For weak signals, even with the use of heterodyne detection and phase-matching, the signal may be buried in the background. A way of isolating the signal is phase-cycling,

where each spectrum is taken multiple times and the relative phase of the pulses is varied and added in a way that the linear contributions such as luminescence and scatter are canceled in the acquired signal while the FWM signal adds up with each spectrum [19]. The phase-cycling scheme used is a two-axis phase-cycling scheme where the phase of the first two pulses is changed by π (A and B for rephasing, non-rephasing and zero-quantum, C and D for double-quantum). The procedure is summarized in Table 2 for rephasing scans with the different spectra being taken labeled S1−S4. The FWM phase contains contributions from all three pulses A, B, C and therefore the phase of π on both A and B gets cancelled out in the FWM signal. In the case of double-quantum scans the pulses C and D are modulated instead in order to maintain the phase-lock inside the instrument.

Pulse	S1	S2	S3	S4
A	0	π	π	0
B	0	0	π	π
C	0	0	0	0
FWM	0	π	0	π

Table 2: Phase-cycling scheme used for rephasing, non-rephasing and zero-quantum scans. S1-4 correspond to four spectra that are being taken successively.

A phase of π is equal to a negative sign of the spectrum. Therefore, adding the signals as $S_{tot} = S1 - S2 + S3 - S4$ it is seen that the contribution to the total spectrum due to beams A and B completely cancels and only four FWM signals remain.

3.2 Experimental Methods

In this section some experimental methods for performing FWM and 2DCS spectroscopy are discussed. As seen before, there are three time delays contributing to a FWM signal of interest. Depending on the pulse ordering and which of the delays

is scanned, different information about the system and the coherence or population dynamics can be extracted.

3.2.1 Time-Integrated Four-Wave Mixing

One of the simplest FWM techniques is TI-FWM in which only one delay is scanned and the signal is integrated over its emission time. By scanning delay τ shown in Figure 4, the homogeneous lifetime can be measured and coherent coupling between two states can be resolved. However, care must be taken not to confuse coherent coupling with possible interference effects. An example spectrum comparing a homogeneous and inhomogeneously broadened system is shown in Figure 9. The homogeneously broadened case in Figure 9a is taken from Potassium (K) vapor in Argon buffer gas atmosphere inside a high temperature cell at 165 °C [126]. Potassium in this experiment can be treated as a three-level system with two excited states connected through a common ground state. This leads to quantum beating between the two states at their difference frequency, in the case of the potassium D_1 and D_2 lines, the difference frequency is 1.73 THz corresponding to a beating period of 578 fs. The beating period can be readily read off the graph. The decay of the envelope function is related to the rate of decoherence between the two D states, measured to be ≈ 5 ps. In the graph presented, the decay constant is measured to be $\tau = 4.55 \pm 0.14$ ps. In contrast, the result of the TI-FWM of a $MoSe_2$ ML at 10 K and with 30 mW excitation power per beam is shown in Figure 9b. The most prominent feature is the fact that the FWM signal rises and decays within almost the same time. This reflects the rapid dephasing in ML-TMDs which is on the same order as the pulse duration, or the response function of the experiment. The actual dephasing time is too short to be clearly resolved by TI-FWM so a reference scan is taken with beam C blocked. Even though the amplitude of the reference scan is much lower, this could be due to a

decreased autocorrelation strength between the excitation pulses, as only two instead of three pulses are interacting at the sample. The autocorrelation between beams A and B can be fit by a Gaussian with width 250 fs centered around -50 fs. The fit is shown as the green curve in the figure. To exclude the possibility of the measured signal being purely from autocorrelation a power dependence measurement is necessary, which allows a clear distinction between a nonlinear signal and autocorrelation. The result of the power dependence is shown as a double-logarithmic plot in the inset along with a fit to the data. The slope extracted from the fit is 1.9 which is clearly larger than the expected value of 1 for autocorrelation. It is also significantly lower than the value of 3 expected for a third-order signal. This can be understood by considering the strong scattering of the beams on the sample surface leading to a significant contribution of autocorrelation to the third-order signal lowering the overall slope of the power dependence.

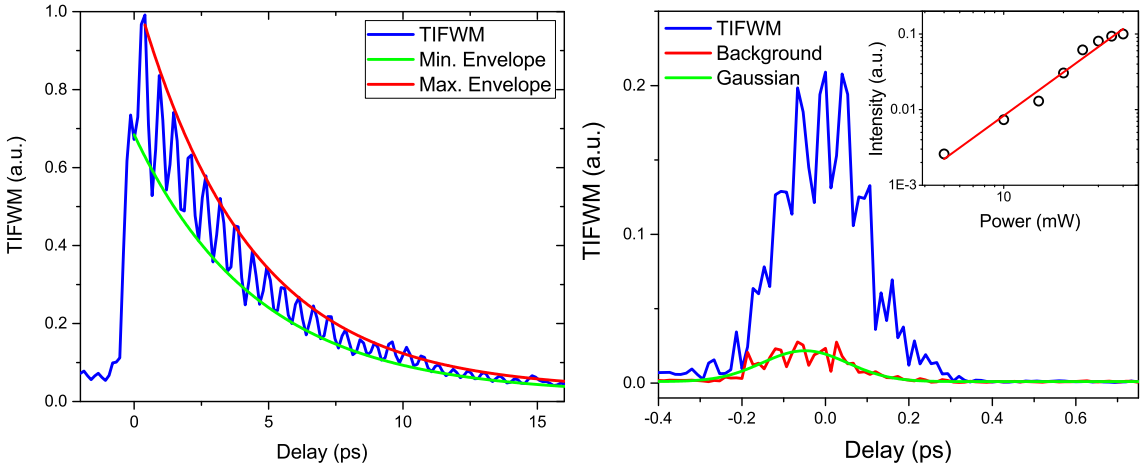

(a) (b)

Figure 9: TI-FWM traces of (a) potassium vapor in a high temperature cell at 165 °C (b) $MoSe_2$ at 10 K. The inset shows the power dependence of the TI-FWM signal used to confirm the nonlinear nature of the signal.

Another implementation of TI-FWM is scanning delay T, while keeping delay τ fixed and integrating the signal over the emission time. In this case information about

the incoherent population dynamics can be obtained. This is the typical pump-probe experiment where the first pulse acts twice and the second (generally weaker) pulse acts once. A non-degenerate pump-probe experiment is presented in Section 4.

3.2.2 Two-Dimensional Coherent Spectroscopy

Two-dimensional coherent spectroscopy is a powerful experimental method and an extension of T-FWM. The idea of 2DCS stems from NMR where it was awarded a Nobel prize in chemistry [34]. Transferring the method to the optical domain had been originally proposed by Tanimura and Mukamel [37]. However, it took some years for experiments to achieve the required pathlength stability. The first experimental demonstrations were in the infrared where the restrictions imposed on the optic pathlength fluctuations are smaller [39]. Soon after, the method was applied in the optical and near-infrared spectral regions [38, 40–47].

While in TI-FWM only the delay τ in Figure 4 is scanned, in T-FWM only the delay t is scanned. When performing 2DCS, any two delays in Figure 4 are scanned, yielding a signal as a function of two time delays. The signal is then Fourier transformed along the two time axes to generate a two-dimensional frequency correlation map. Fourier transforming the signal poses a strict requirement on the stability of the experimental setup, since in order to perform the FT, knowledge of the amplitude and phase is required. In the non-collinear approach, this is realized by active phase-locking to a reference laser copropagating with the excitation pulse laser. Besides the requirement for phase-locking, the requirements on passive phase-stabilization of the optical delays are immense. The instrument used throughout this dissertation is based on the platform presented in [28] and can actively phase-stabilize relative pathlength fluctuations to less than $\lambda/100$, i.e. a few nanometers.

Non-Collinear Two-Dimensional Coherent Spectroscopy

To perform non-collinear 2DCS the main concern is keeping the relative pathlength fluctuations between pulses that are spatially separated to a minimum. This is achieved by

1. Building the instrument as sturdy as possible leading to passive stabilization within the instrument

2. Keeping optical assemblies as close to the surface they are attached to as possible minimizing oscillations of the optics

3. Using high-precision translation stages for changing the delay between pulses

4. Actively stabilizing the phase using a reference laser that samples the same pathlength fluctuations as the pulse laser.

The first and second parts are done during the design process of the instrument and have been presented in detail in [28]. The third part was the main source of instrumental problems during the work leading up to this dissertation. The motors need to be both accurate and stable. While the accuracy and stability of the motors used (Newport XMS series) has been found to be outperforming their specifications, the controller that was originally issued with them (Newport XPS-Q8) has been shown to suffer from crosstalk between different channels when connecting more than one motor leading to in-position instability. The problem was resolved by replacing the original controller with a different controller version with fewer total channels (Newport XPS-RL) with which the specified motor performance was achieved. Lastly, once a sufficiently high positional accuracy and in-position stability of the motors has been achieved, a reference laser is copropagated with the pulses sampling the remaining optical pathlength fluctuations. Although the mechanical stability of the

system may be below the threshold required for FT, the optical pathlength may still fluctuate more than what is required for successful FT since environmental conditions such as airflow modify the local optical density. The contributions of airflow to the optical pathlength fluctuations are kept to a minimum by enclosing the whole setup and enclosing the instrument used for generating optical delays itself as well.

Even with all the discussed passive stabilization techniques, monitoring and control of the pathlength is necessary. The pulse laser cannot be used to sample the pathlength fluctuations, since during a measurement the pulses are moved away from each other in time and will therefore no longer interfere after stepping any one pulse for a delay longer than the pulse duration of approximately 100 fs. To overcome this issue, a continuous wave (cw) laser at $\lambda_{\mathrm{Ref}} = 532$ nm (shorter wavelength than the pulse laser) is copropagated with the pulse laser. The cw laser now samples the same optical pathlength as the pulse laser while simultaneously allowing a higher precision of the pathlength measurement because of the shorter wavelength. Interfering the cw laser from different paths the optical pathlength can be measured with interferometric precision. The interference signal is acquired using a photodiode and used as the error signal to a feedback loop actively correcting the optical pathlength through a piezo-mounted mirror in real-time. The feedback loop is implemented on a field-programmable gate array through a PID control with disabled derivative gain. Disabling the derivative gain allows for higher in-position robustness while sacrificing the time it takes to reach the setpoint. Since the PID controller is much faster than the remaining parts of the setup even without derivative gain, the tradeoff between control speed and robustness is not an issue. While the controller reaches the phase-lock within less than a microsecond, taking a single spectrum takes between $2 - 100$ milliseconds. The flowchart for the stepwise process when recording rephasing scans is shown in Figure 10, other scans will unlock different feedback loops but the overall

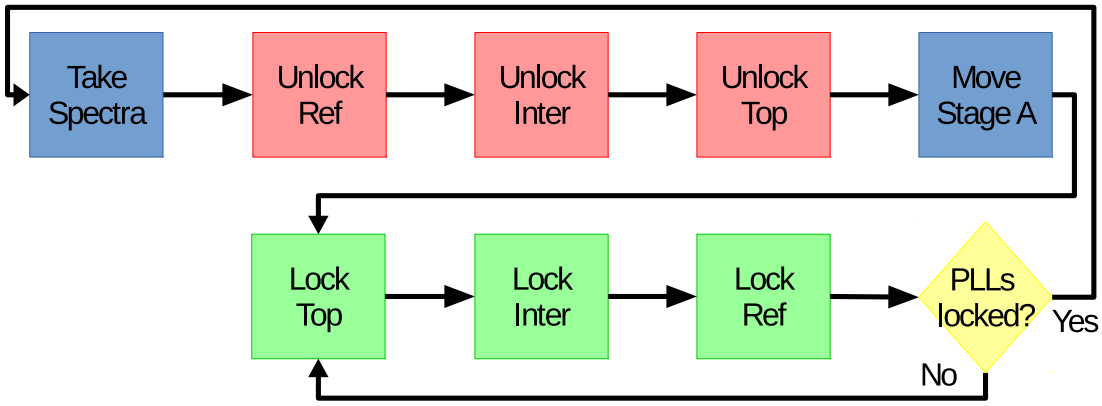

Figure 10: Flowchart of the phase-locking algorithm used for rephasing non-collinear 2DCS scans.

principle is the same. The logic for which loops to unlock is implemented in software and is chosen when selecting the type of scan to perform. For the first step, the phase-locked loops (PLLs) are locked and spectra are recorded manually. Then the PLLs are sequentially unlocked, the motor is stepped and the loops are locked in reverse order than they were unlocked. Afterwards, the locking is checked by recording the output from each of the PLLs. If the lock is sufficiently good, the next spectrum is recorded and the diagram starts from the first step again. Using this scheme, control of the optical pathlength can be achieved with $\leq \lambda_{\text{Pulse}}/100$ precision allowing FT of the TFWM signal along the time axis being stepped.

The wavelength of the reference laser could in principle be chosen arbitrarily, however there are some practical limitations on the wavelengths used for the reference laser. While physically a short wavelength is better, since the same optic pathlength fluctuation will result in a larger phase change of the reference laser, technical issues arise when using wavelengths that are too far away from the pulse laser central wavelength. These are mostly due to optical coatings not working for spectrally broad bands, leading to additional reflections of either the pulse laser or the reference laser. Reflections of the pulse laser will modify the optical response from the material, since

it will be multiply excited, so the coatings should be optimized for the pulse laser. Reflections of the reference laser will, as long as they are not in phase with the main order, degrade the contrast of the monitored interference signal, such that the reference laser wavelength should be chosen as close to the pulse laser wavelength as possible. The reference wavelength of 532 nm is a good compromise, since broadband coatings from $500 - 900$ nm are commercially available while the wavelengths are sufficiently far apart that the reference laser can be separated from the pulse laser using a dichroic mirror. However, the first iteration of the setup had beamsplitters coated only for the pulse laser centered around 800 nm which led to a weak contrast in the reference lock-in loop due to the reference laser having unequal intensity in the different interferometer arms.

After leaving the instrument, four phase-locked pulses are copropagating on the corners of a box, as shown in Figure 11. Three of the four pulses are focused onto the sample where the T-FWM signal is generated in the phase-matching direction discussed in Section 3.1.4. The three pulses only propagate through common optics after leaving the instrument to minimize relative optical pathlength differences on the way to the sample. The fourth pulse is routed around the sample and combined with the T-FWM signal after which the interferogram of T-FWM and reference pulse is recorded on a spectrometer. The pathlength between reference and T-FWM signal is also phase-stabilized using a feedback loop adjusting the reference arm pathlength. Depending on the type of scan, either the interference between pulses Ref and C or Ref and A is used for locking the phase. The reason for using different excitation pulses to lock onto lies in the fact that now the relative delay between the interferometer arms becomes crucial. While inside the instrument the cw laser was used for phase-locking which can interfere with itself for optical pathlength differences within its coherence length of a few metres, now only the pulse laser can be used for the

phase-locking. The coherence length of the pulse laser however is given by the pulse duration and on the order of a few to tens of micrometers. Therefore, a pulse that is scanned during the acquisition of a 2D spectrum can not be used as a pulse for locking the reference path and different pulses are used for different 2D scan types.

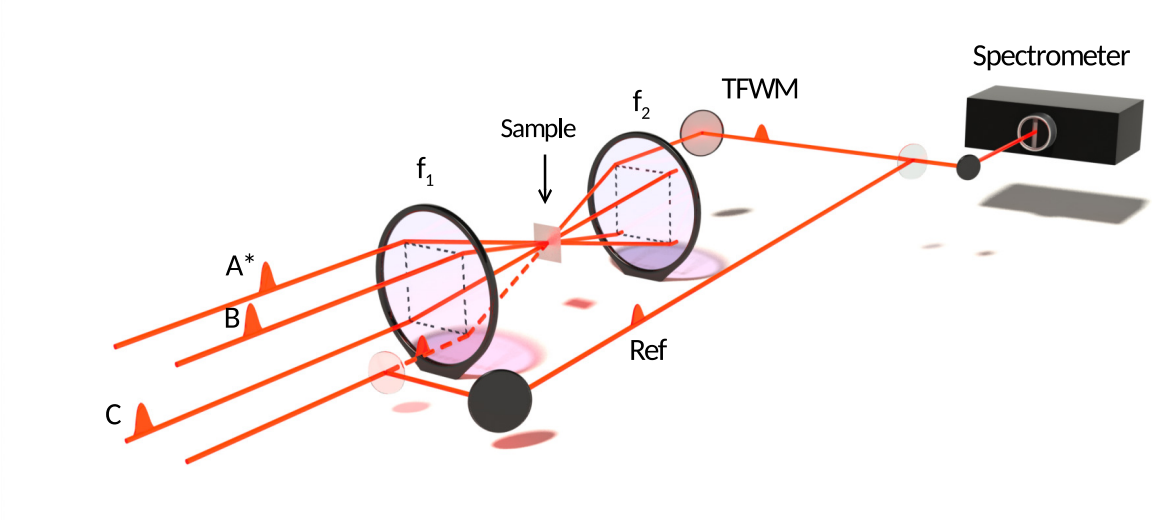

Figure 11: Schematic of the FWM generation and detection. Three pulses are focused onto the sample where a FWM signal is generated in the phase-matching direction $\vec{k}_{\mathrm{FWM}} = -\vec{k}_A + \vec{k}_B + \vec{k}_C$. The FWM signal is combined with a reference pulse routed around the sample and sent to a spectrometer where heterodyne detection is used to extract the FWM signal. Adapted from [127] with permission.

The combined T-FWM and reference pulses are used for heterodyne detection of the signal on a spectrometer and the emission time and phase of the T-FWM signal is retrieved using spectral interferometry (SI). To get the second time-axis one of the delays between the excitation pulses is scanned. For each scan step the PLLs according to the interferometer arms affected by the scan step are unlocked, one or two motors are moved, then the PLLs are locked again and a spectrum is taken which is then repeated until the total number of requested steps is reached. When using phase-cycling, four spectra with different relative phases are taken and added and subtracted to isolate the FWM signal as shown in Table 2. During the whole scan

time, the phase-lock needs to be maintained. The optic table on which the setup operates therefore may not be touched and the whole optical setup as well as the instrument containing the delay stages are enclosed to reduce airflow.

Collinear Two-Dimensional Coherent Spectroscopy

For the collinear approach also a single pulse is split into four copies. Each copy is tagged with a unique phase modulation frequency using an acousto-optic modulator (AOM). The pulses can then be independently delayed before they are recombined and sent to the sample through a common pathway. A reference laser copropagates with the pulse laser, but in this case should be as close as possible to the frequency of the pulse laser in order for pathlength fluctuations to produce the same phase difference in the excitation and reference laser. However, a technique has been developed by Eric Martin in his thesis [32] to use an arbitrary reference frequency and calculate the corresponding optic pathlength change from the phase difference. Besides the need for adequately sampling the optic pathlength differences, the reference frequency also acts as the reference frequency for calculating the axis of a 2D spectrum, such that using a large frequency difference between excitation and reference laser will require a very small stepsize to fully sample signals within the measured bandwidth. Therefore, different reference lasers are used to match the resonance of interest. This can be done by switching out the diode laser used as the reference laser. Placing the diode laser inside an external cavity, the wavelength of the laser can be sufficiently stabilized to allow phase referencing. Furthermore, placing a diode laser inside an external cavity narrows the linewidth such that longer scan durations are possible compared to a diode laser without external cavity.

The excitation and reference laser copropagate, therefore picking up the same optic pathlength differences. The reference laser is then split off the excitation laser

and the reference signal from the different paths is interfered on a photodetector. The interference pattern is modulated at the beat frequencies between the different beams. The relevant term in the collinear approach for isolating the signal from the background in Equation 14 is the phase term $e^{i(-\omega_A t_A+\omega_B t_B+\omega_C t_C)}$.

Since in this experiment there are four pulses incident on the sample, a fourth term $\omega_D t_D$ needs to be added to the exponential. The effect of an AOM can be understood as introducing a time-dependent phase term $\phi_i^f(t)$ to each beam. Here i labels the pulse and f the modulation frequency applied to the AOM. The phase term is therefore rewritten as

$$e^{i(-\omega_A t_A+\phi_A^{f_A}(t_A)+\omega_B t_B+\phi_B^{f_B}(t_B)+\omega_C t_B+\phi_C^{f_C}(t_C)+\omega_D t_D+\phi_D^{f_D}(t_D)}.$$

When all four beams are incident onto a detector, the measured interference between the beams is at all possible beat frequencies of the four AOM frequencies

$$\omega_S = \pm f_A \pm f_B \pm f_C \pm f_D.$$

Selecting only one frequency, one scan type can be performed. By detecting the signal at multiple frequencies at once, all possible 2D spectra can be recorded at the same time [128].

Since the experiment uses lock-in detection, the reference frequency determines the number of cycles contributing to the signal when using a fixed time constant. The larger the number of cycles, the higher the signal to noise ratio, meaning that the reference frequency should be chosen as high as possible with the repetition rate of the laser being the upper limit on the reference frequency. However, the electronics available in the experiment pose a limitation on the maximum frequencies that can be used. Although the repetition rate of the laser used is close to 80 MHz, the beat

frequencies are chosen on the order of tens of kHz since the bandwidth of the available electronics do not allow for higher frequencies. The modulation frequencies f_i used in the experiment are summarized in Table 3. Although each individual frequency is in the RF regime, the resulting beat frequency is in the audio band and can be detected using conventional electronics. Improving the electronics to be able to process RF signals, the signal to noise ratio can be enhanced while keeping the acquisition time constant by choosing a higher mixing frequency and therefore averaging the FWM signal over more cycles on the lock-in amplifier. On the other hand, improvement of the electronics and the associated increase in cycles per unit time can lead to a quadratic reduction of the required acquisition time while keeping the signal to noise ratio constant. In order to increase the signal to noise ratio even with the electronics currently in use, the time constant can be increased which comes at the cost of acquisition time increasing quadratically, since two axes need to be scanned.

Frequency	Value (MHz)
f_A	80
f_B	80.003
f_C	80.1173
f_D	80.100
$-f_A + f_B + f_C - f_D$	0.0143

Table 3: Frequencies used to tag each pulse as well as the detected beat frequency between all four pulses.

The four pulses are combined such that they overlap and copropagate and are then focused onto the sample, from where the signal can be collected. Different approaches have been used for measuring the signal, the first approaches to collinear 2DCS used photocurrent detection [29], later the collinear technique was expanded to detection in the transmission and reflection geometry. Signal collection is also possible by collecting just the specular reflection, as long as the signal radiates homogeneously [50, 51]. This is especially useful when using high power pump beams since the

direct reflection will easily saturate any detector. Since the encapsulated samples studied in Appendix A are on silicon, which is reflective in the near-infrared, and the samples have side lengths of approximately 10 µm and are held inside a cryostat during experiments, the signal needs to be collected through a high numeric aperture long-working distance microscope objective in the reflection geometry.

Heterodyne Detected Collinear Two-Dimensional Coherent Spectroscopy

Heterodyne detection for non-collinear 2DCS was discussed in Section 3.2.2, but the technique of heterodyning a signal is not unique to the non-collinear implementation of 2DCS. The same principle of amplifying the signal through a heterodyning field can be used in the collinear geometry. In this case only three pulses interact with the sample generating a radiating polarization. The polarization is then combined with a fourth pulse on the detector, just like when using non-collinear 2DCS. If the detector is a photodiode, the delay of the fourth pulse needs to be scanned in order to resolve the time axis, if the detector is a spectrometer with a charge-coupled device (CCD) camera, the delay can be obtained from the interference pattern between heterodyne and signal pulse.

The advantage of using heterodyne detection lies in the lower nonlinear order of the interaction. While PL or photocurrent detected 2DCS is a fourth order process, the FWM signal is due to a third order process. With the same reasoning as in the discussion between second and third order signals, the reduction from fourth to a third order signal typically leads to at least one order of magnitude stronger signal. Furthermore, the FWM signal is directional as long as the radiating structure is larger than the wavelength of the exciting light, leading to a directed signal rather than a homogeneous emission. This is both a blessing and a curse, since the homogeneous emission can allow for detection of the specular reflection and strong suppression of

the excitation beams, while the directional signal needs to be detected in the same direction as the excitation beams, leading to easy saturation of the detector. The directionality has the advantage that for weak signals, for example a signal from a ML with small dipole moment, the signal is radiating only in one direction, giving an appreciable signal magnitude in this direction, while in the PL detection the overall amplitude is spread throughout the full solid angle. Therefore the detectable signal is overall stronger for the heterodyne detected setup. The disadvantage lies in the fact that the heterodyning beam needs to be perfectly parallel and overlapped with the signal beam path in order to yield a good interference contrast. Misalignment of the heterodyning beam will lead to a multiline interference pattern, which, if integrated on a large area detector, will not show any change in amplitude when moving the relative delay.

4 Incoherent Trion Valley Dynamics in Monolayer $MoSe_2$

4.1 Introduction

To pave the way for application of ML semiconductors, it is important to investigate the carrier dynamics, since these are a major limitation of typical device performance. In ML semiconductors carriers can form bound states, electron-hole pairs, called excitons. In the presence of defects other bound states can form, for example localized excitons in MoS_2 [129]. In $MoSe_2$ MLs charged excitons can form either through the capture of an excess charge by an exciton or directly from an unbound electron-hole plasma [130–133]. In ML-TMDs, strong Coulomb interaction leads to exceptionally high binding energies for excitons and trions [134, 135], making excitons and trions stable even at room temperature [75,80,82,136,137]. The effect of trions can easily be observed in the overall PL spectrum in ML $MoSe_2$ and has been shown to reduce the conductivity in MoS_2 [138]. Besides these direct effects of trions on the optoelectronic properties of a ML-TMD, the interaction with excitons is of interest. Trions provide an additional relaxation channel for excitons because of their lower energy [83]. Excitation of trions by an optical phonon is an upconversion process to an excitonic state observed in WSe_2 [107]. Furthermore, coherent coupling between exciton and trion has been observed in ML $MoSe_2$ [139]. Besides being possibly detrimental to device performance, deliberately introducing defects to generate trions can also be used for device engineering, for example in quantum information processing [140]. Therefore, to fully unlock the potential of ML-TMDs, a thorough understanding of the dynamics of both excitons and trions in ML-TMDs is necessary.

Optical spectroscopies allow direct access to the electronic energy scales in semiconductors and are therefore ideally suited methods for the understanding of carrier dynamics. Some of the techniques used are TR-PL [141, 142], ultrafast pump-

probe spectroscopy [7, 21, 103, 143–150], optical Kerr spectroscopy [14, 151], 2DCS [15, 60–62, 64, 152, 153] and hole-burning spectroscopy [154]. These studies have been able to reveal important structural and dynamics information of layered TMDs. However, the focus of these studies has been mainly on the exciton dynamics while the trion dynamics remained largely unexplored. More recently studies of the trion formation in ML $MoSe_2$ by ultrafast pump-probe spectroscopy [21] and the trion emission in ML WSe_2 by TR-PL have brought attention to the valley dynamics of trions in layered TMDs [155].

This section contains an experiment studying the valley trion dynamics in a chemical vapor deposition (CVD) grown $MoSe_2$ ML by using ultrafast pump-probe spectroscopy. The trion population forms within 500 fs from photoexcited free carriers. The trion decay follows a biexponential decay and exhibits a surprising density dependence, as the dynamics become slower as excitation density increases. A theoretical model is developed based on a set of rate equations which quantitatively reproduces the experimental result for all pump fluences. The model reveals that the primary mechanisms responsible for the observed density dependence of the dynamics is the decay of trions into two different types of defect states. The slowing down of dynamics at high density is ascribed to filling of the limited density defect states.

4.2 Experiment

This section briefly discusses the sample used in the experiment and then goes on to present preliminary data used in the later pump-probe experiment. Furthermore, the pump-probe setup is discussed in detail.

4.2.1 Sample Description

The sample is $MoSe_2$ grown via CVD on SiO_2/Si substrate as described in [156]. After the growth, the sample is transferred from the SiO_2/Si substrate onto a glass substrate. Using this process, large single-layer triangular flakes of tens to more than one hundred micrometers in size can be grown. More recent developments are able to grow wafer-size MLs [157–159]. The size of the triangles is essential since edge effects change the optoelectronic properties of ML-TMDs [160]. The flakes used for the experiment are about 100 µm in size, much larger than the focal spot of the lasers used, completely eliminating edge effects. During all experiments the sample is kept inside a microscopy cryostat and under high vacuum with pressure less than 10^{-6} Torr.

4.2.2 Preliminary Sample Characterization

Before performing pump-probe spectroscopy, the resonance energy of of the sample needs to be found. This is done by performing steady-state microscopy-PL (µ-PL) on the sample. From pulsed excitation µ-PL experiments, the density of excitons and trions is measured. Performing pulsed excitation µ-PL the excitation conditions during the pump-probe experiment are reproduced, such that the exciton and trion densities extracted from the µ-PL measurements can be used in the explanation of the pump-probe results.

Steady State Measurements

The absorbance of the sample is measured at room temperature using a broadband white-light halogen lamp, the result of which is displayed as the blue curve in Figure 12. The absorbance curve exhibits two peaks at 1575 meV and 1745 meV which are ascribed to the A and B exciton resonances. The A exciton resonance is expected

to also contain the absorbance from the A trion. A green (2.3 eV) cw laser is used as the excitation source for the µ-PL measurements. The PL is shown as the red curve in Figure 12 and shows a strong peak at the energy of the A exciton while emission at the energy of the B exciton is below noise level.

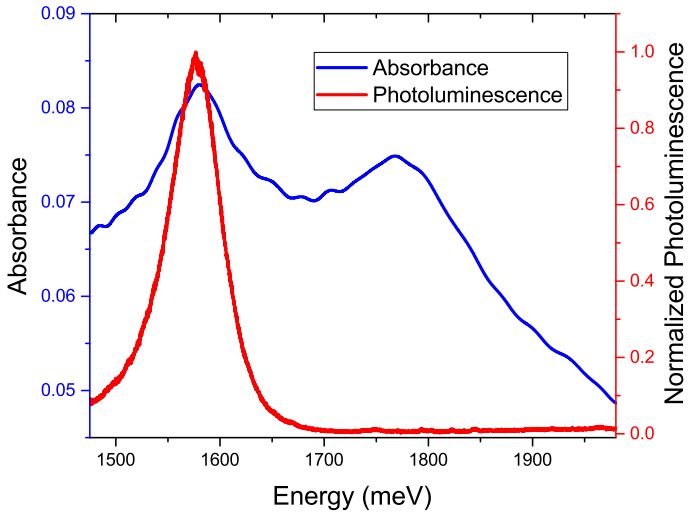

Figure 12: Room temperature absorbance of a $MoSe_2$ ML excited by broadband white-light from a 20 W halogen lamp (blue curve) and normalized PL emission from the ML upon excitation with a green (2.3 eV) cw laser.

Pulse Excitation PL

After having found the resonance energy of exciton and trion in the sample the excitation laser is replaced with the pump laser used during the experiments to better reproduce the experimental conditions. Furthermore, the sample is transferred to a microscopy cryostat where it can be cooled to liquid helium temperature. The excitation beam is focused onto the sample by a 50× long working distance objective leading to a tight focal spot with diameter on the order of few micrometers in size. The PL is collected by the same objective and spectrally filtered using a high-fidelity low-pass filter. The PL emission is recorded as a function of temperature and can be seen in Figure 13a. With decreasing temperature, the PL becomes stronger reflected

by an increased signal to noise ratio at low temperatures in the normalized spectra presented here. Additionally, the PL narrows and blueshifts until 150 K. Below 120 K two peaks become visible of which the high (low) energy peak is ascribed to the exciton (trion) resonance. The two peaks further narrow and blueshift until 10 K. At 10 K a power dependence of the PL is measured, which is shown in Figure 13b. The minimum fluence used is 10 $\mu J \cdot cm^{-2}$ and the maximum fluence is 160 $\mu J \cdot cm^{-2}$ giving access to more than one order of magnitude variation of excitation densities. Using pump fluences larger than 200 $\mu J \cdot cm^{-2}$ was found to damage some of the flakes on the sample substrate, visible in microscope images and is therefore avoided.

Each PL spectrum is fit using two Lorentzian peaks as shown in Figure 13c for 80 $\mu J \cdot cm^{-2}$. The parameters extracted from the fit are then used for further analysis. The pump fluence dependence is shown in Figure 14a and reveals that both the exciton and trion peak area linearly increase within the excitation powers used during the pump-probe experiment. This means that neither the exciton nor the trion resonance is saturated upon excitation with fluences up to 160 $\mu J \cdot cm^{-2}$. The peak center energy for different excitation densities is shown in Figure 14b and shows a redshift of the trion emission whereas that of the exciton blueshifts. Furthermore the linewidth is measured and shown in Figure 14c. Both the exciton and trion emission linewidth slightly increase with increasing excitation density.

4.2.3 Two-Color Pump-Probe Experiment

Now that the sample has been characterized and the resonances are found through µ-PL, the pump-probe experiment is performed. A schematic of the setup is shown in Figure 15. The setup consists of two lasers at different wavelengths. The Ti:Sapphire oscillator is used to generate pulses with approximately 100 fs pulse duration and bandwidth of 8 nm meaning that the pulses are nearly transform-limited. The center

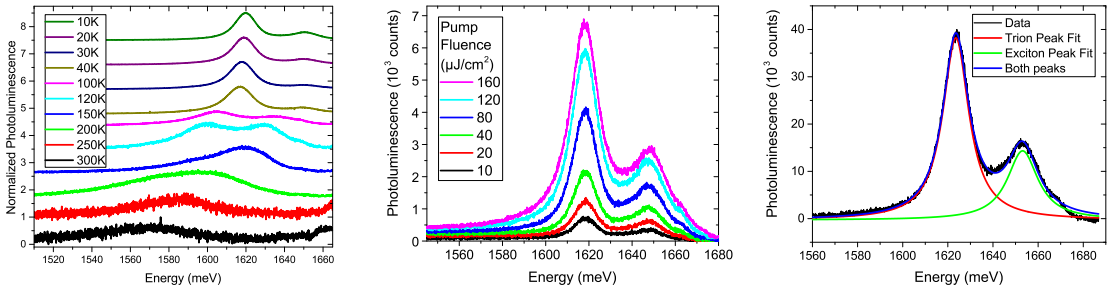

(a) (b) (c)

Figure 13: (a) Temperature dependence of the PL from a $MoSe_2$ ML. (b) Power Dependence of the PL from the same $MoSe_2$ ML at 10 K. (c) Data and double-lorentzian fit of the spectrum at 10 K taken with an excitation density of 80 μJ·cm^{-2}. Adapted from [83] with permission.

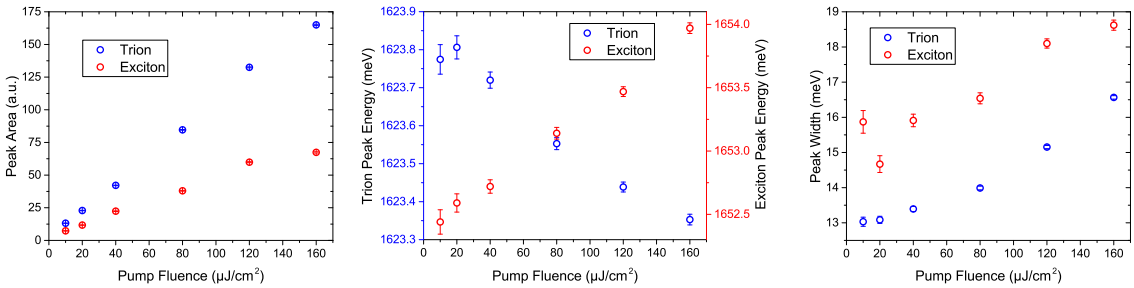

(a) (b) (c)

Figure 14: (a) Integrated peak area at different pump fluences for the trion (blue) and exciton (red) peak. (b) Peak Energy of the trion and exciton resonance. (c) Linewidth of trion and exciton resonance. Adapted from [83] with permission.

wavelength of the output is tuned to the peak of the trion PL at 1625 meV for 10 K. The output is split using a 90 : 10 beamsplitter and 90 % of the power is used to pump an optic parametric oscillator (OPO). The OPO output is frequency doubled using a β-Barium borate crystal, which gives pulses with approximately 500 fs pulse duration and adjustable center wavelength. The polarization of each pulse can be adjusted independently and right before the sample a quarter-wave plate is placed which is used to convert linearly polarized light to circularly polarized light. An important component is the set of two long focal length lenses in each of the excitation beam paths which are used to individually adjust the pump and probe beam diameter at the

sample position. The pump diameter is set to be about 7 µm while the probe beam diameter is only 5 µm to ensure a homogeneous excitation of the probed area. The pulses are combined on another beamsplitter and sent to a home-built microscope setup, where they are focused onto the sample and the reflected beams are collected through the same microscope objective. The beams are then split with a 50 : 50 beamsplitter plate to simultaneously illuminate a CCD camera used to measure the spot sizes and a photodiode used to detect the signal. A halogen lamp can be coupled into the setup instead of the laser beams to find the sample and ensure a good overlap between a sample flake and the excitation beams.

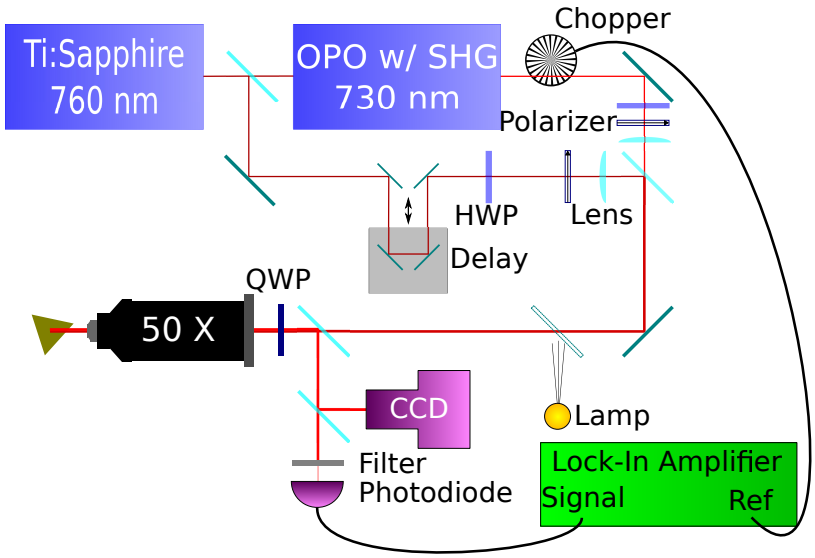

Figure 15: Schematic of the pump-probe setup.

A longpass spectral filter with a cutoff wavelength of 750 nm (1653 eV) to remove the pump beam is placed before the detector to extract the signal from the background. Furthermore, the pump beam is amplitude-modulated using a chopper wheel before interacting with the sample and lock-in detection of the probe beam is used to improve the signal-to-noise ratio.

The experiment is performed using collinearly propagating pump and probe beams in the reflection geometry. The two beams are focused onto the sample using the same

50× long working distance microscope objective as used for the µ-PL measurements. The long working distance is necessary, since the sample is held in a liquid helium cryostat where the sample is approximately 10 mm away from the cryostat window.

Before taking a full set of data, a probe fluence dependence is taken at a medium excitation density of 80 µJ·cm^{-2}. The probe fluence dependence shows a linear increase with probe fluence, the signal-to-noise ratio gets better within the studied range, and the decay dynamics are unchanged between the different fluences. The probe fluence is then fixed to 1 µJ·cm^{-2}, such that the probe fluence is about one order of magnitude smaller than the lowest pump fluences used in the following experiment. A set of data consists of a pump-probe scan trace for co- and cross-circularly polarized excitation beams and is repeated with different pump fluences.

4.3 Results

In this section the results from the two-color polarization-resolved pump-probe experiment are shown. First, the results on the valley polarization generated at different excitation energy are laid out, followed by a discussion of the dynamics at different pump fluences.

4.3.1 Pump Energy Dependence

Different pump energies were used in order to extract a nonzero polarization, as time-integrated studies have shown a strong dependence of the injected valley polarization on the pump energy [93]. For ML MoS_2, the valley polarization shows a continuous decrease of the valley polarization degree from 40 % when pumping approximately 100 meV above the A exciton resonance to almost zero as the pump energy gets increased to $>$ 2 eV [11]. In ML WSe_2 the valley polarization exhibits a global maximum when pumping 140 meV above the A exciton resonance, which is ascribed

to the first excited exciton state $2s$ [149]. The change in valley polarization with the pump energy becoming closer to being on resonance can be understood in terms of the bandstructure of ML-TMDs. While electrons are always excited within one valley, as their energy increases, the processes involved in the relaxation to the conduction band minimum will more likely add sufficient momentum to the electron to be transferred into the other valley. By resonantly pumping the excited state of the A exciton, the generation of valley polarization is enhanced, since in the transition back to the ground state the valley polarization is conserved as the process happens without invoking multi-phonon mediated relaxation. Furthermore, it was found that excitation at the resonance energy of the $MoSe_2$ B-exciton transition may lead to larger valley polarization than exciting off-resonance with a lower energy [93]. Hence, the pump energy is tuned as close as possible to the trion transition and on resonance with the B-exciton transition.

A pair of resulting spectra is shown in Figure 16 with the inset highlighting the dynamics around the zero delay showing the ultrafast signal buildup. Each dataset consists of the average decay behaviour of ten runs and the error bars are the standard deviation at each datapoint. When running the experiment, a co- and cross-circular spectrum are acquired in direct succession to minimize the effect of long-term fluctuations of the laser power or center wavelength.

For analysis, both spectra are offset in the y-direction so that the average transient reflection for delays smaller than zero is equal to zero. This way, any residual difference between the two spectra stems from a difference in the valley polarization and is not because of different background signal for different laser polarization. Figure 17 shows the result of plugging the processed signals into the equation for valley polar-

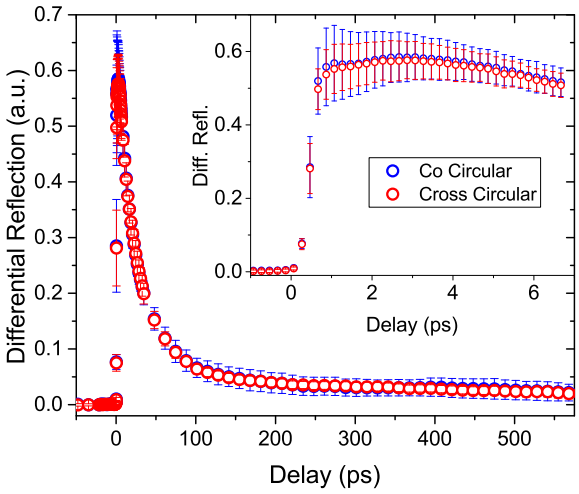

Figure 16: Pump-probe data of the trion resonance when excited at the B exciton resonance and a pump fluence of 80 µJ·cm^{-2}. The inset shows the response around the zero delay between pump and probe pulses.

ization alongside the pump-probe data used for calculating the valley polarization

$$\text{Polarization} = \frac{I_{\text{co}} - I_{\text{cross}}}{I_{\text{co}} + I_{\text{cross}}}. \tag{16}$$

The valley polarization calculated this way is zero if there is no valley polarization, i.e., the population in the two valleys is exactly equal, while it is $+(-)1$ if all the population is in the excited (opposite) K-valley. The error bars on the polarization are obtained from calculating the standard deviation of the polarization between different measurements. Within the uncertainty of the measurement, it can be concluded that in $MoSe_2$ MLs, there is no polarization generated, in support of previous TR-PL measurements [93].

4.3.2 Pump Power Dependence

After having found that valley polarization can not reliably be generated optically in ML $MoSe_2$, the dynamics of trions in the two valleys are investigated. A typical pump-probe trace can be seen in Figure 18a, where the pump energy was tuned to 735

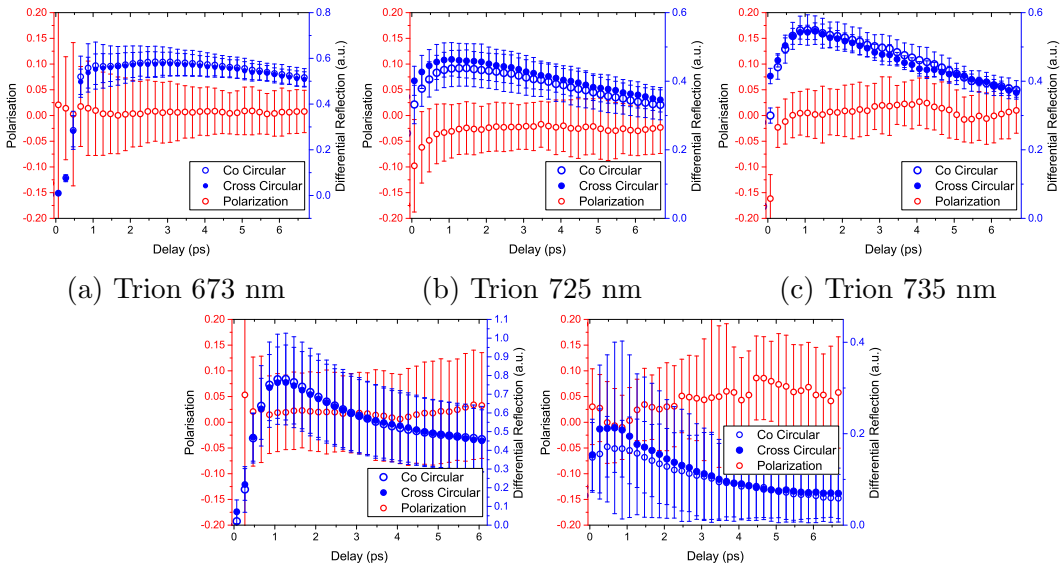

(a) Trion 673 nm (b) Trion 725 nm (c) Trion 735 nm

(d) Exciton 673 nm (e) Exciton 725 nm

Figure 17: Pump-probe signal trace and calculated valley polarization for different pump and probe energies.

nm, along with a zoom in to the time close around the zero delay shown in Figure 18b. Whereas in Figure 16 the absolute values of the pump-probe signal are shown, the spectra in Figure 18 have been normalized. Furthermore, Figure 16 shows an average between multiple measurements while Figure 18a shows the results from a single run and therefore no statistical error is shown. The offset between co- and cross-circular signals is matched for negative delays to remove contributions to the signal from different background for different polarization configurations. In Figure 18b, besides the data for co- and cross-circular excitation, a Gaussian pulse shape with 500 fs pulse width and the trace corresponding to the integration of the pulse are added to the graph to highlight the signal buildup behaviour. It can be seen that both the co- and cross-circular signal follow the integration of the pulse, meaning that the time-resolution in the experiment is too low to resolve the trion formation dynamics. The rising behaviour can be explained by two different explanations. Although electrons are excited by circularly polarized light, the fact that they are excited high into

the conduction band leads to non-radiative interaction with the lattice under which they lose their valley polarization. The second possible explanation is that it is possible that in $MoSe_2$, different to other ML semiconductors such as MoS_2, no valley polarization can be generated optically. From the rise of the pump-probe trace it can be deduced that trion formation happens on a timescale shorter than 500 fs, in agreement with other experiments that have specifically investigated the trion formation dynamics [21].

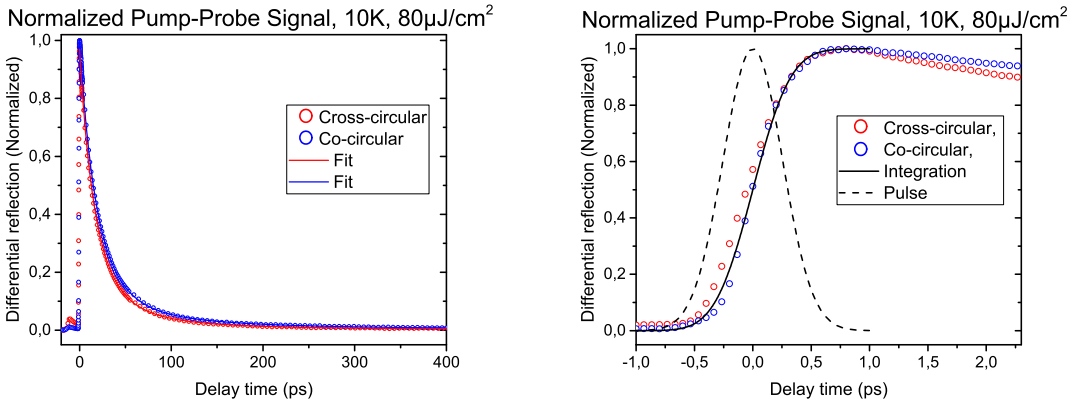

(a) (b)

Figure 18: (a) Data from the pump-probe experiment using a pump fluence of 80 $\mu J \cdot cm^{-2}$. Blue (red) circles denote co- (cross-) circularly polarized pump and probe beams. (b) Zoom in of (a) around the zero delay time. The dashed curve is a Gaussian of pulse width 500 fs, equal to the excitation pulse width used in the experiment. The black curve is the integration of the Gaussian pulse highlighting that the signal buildup is limited by the pulse duration. Adapted from [83] with permission.

The decay of trions happens on a timescale of hundreds of picoseconds and can be resolved by the experiment. The decay curves for co- and cross-circularly polarized excitation in Figure 18a almost overlap, meaning that the dynamics in the two valleys are essentially the same. This behaviour is to be expected, since two conditions are met in the sample. Firstly, trions, once formed, are trapped to their respective valleys by momentum trapping. Since the trions in the two valleys are therefore separate

in momentum space, their decay behaviour is dominated by intravalley relaxation processes which are expected to be the same for the two valleys. Secondly, since no valley polarization is generated, the population density in the two valleys is expected to be the same, meaning that many-body effects in the two valleys are also the same, therefore leading to an overall equal decay behaviour for co- and cross-circular excitation.

For further insight into the dynamics, a fluence dependence is done for both co- and cross-circular polarization. Again, a pair of spectra is recorded in succession as discussed in Section 4.3.1. Since at all powers the results for co- and cross-circular excitation are similar, only the co-circular experiment is used for further analysis. The results for different pump fluences are shown in Figure 19a. All decay traces are fit using a biexponential decay according to the equation

$$f(T) = A_0 \left(e^{-\frac{T}{t_1}} + A_{21} e^{-\frac{T}{t_2}} \right)$$

to extract the decay times. The resulting decay times are shown in Figure 19b and Figure 19c. The decay time increases with increasing fluence, opposite to what one would typically expect for many-body effects.

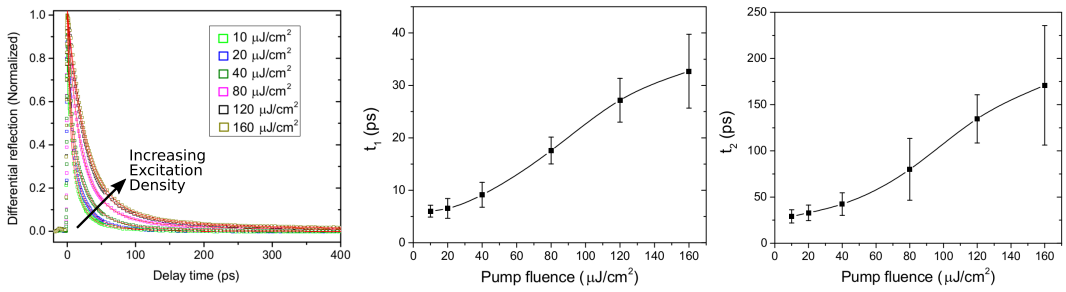

(a) (b) (c)

Figure 19: (a) Data (squares) at different pump fluences as well as biexponential fit (red curve) to the data. (b) Extracted decay time t_1. (c) Extracted decay time t_2. Reproduced from [83] with permission.

4.4 Model

To explain the unexpected decay dynamics revealed by the pump-probe experiment, a model based on rate equations is developed. The model can quantitatively explain the dynamics through the existence of two kinds of defect states. A schematic representation of the energy structure is shown in Figure 20a. Excited electrons form trions on an ultrafast timescale, however the trion formation is not modeled in the rate equations, since it can not be resolved by the experiment. After the trion formation, multiple decay channels exist for the trions, which are each modeled by a single exponential decay. The dynamics observed in the experiment are dominated by decay to two defect states, labeled D_f and D_s in Figure 20a. Filling up of the defect states then leads to a slowing down of the dynamics at high excitation densities, since the decay channel is no longer available. Besides decay into one of the defect states, trions can radiatively recombine, non-radiatively decay or be upconverted to form an exciton. All these processes are much slower than the decay to the defect states, therefore only affecting the long-term decay dynamics corresponding to delay times greater than 100 ps. During the decay time of the trions, excitons can capture an excess charge and be converted into a trion, refilling the trion population which is

also a slow process. The equations governing the dynamics are

$$\dot{N}_X = -\Gamma_r^X N_X - \Gamma_{nr}^X \left(1 - \frac{N_{nr}}{D_{nr}}\right) N_X - \Gamma_{XT} \left(1 - \frac{N_T}{D_T}\right) N_X$$

$$\dot{N}_T = -\Gamma_r^T N_T - \Gamma_f^T \left(1 - \frac{N_f}{D_f}\right) N_T - \Gamma_s^T \left(1 - \frac{N_s}{D_s}\right) N_T + \Gamma_{XT} \left(1 - \frac{N_T}{D_T}\right) N_X$$

$$\dot{N}_f = \Gamma_f^T \left(1 - \frac{N_f}{D_f}\right) N_T$$

$$\dot{N}_s = \Gamma_s^T \left(1 - \frac{N_s}{D_s}\right) N_T \tag{17}$$

where N_X is the exciton density, N_{nr} is the occupation density of non-radiative states, D_{nr} is the available non-radiative state density, N_T is the trion density, $N_f(N_s)$ is the occupied density in the fast (slow) trapping states, $D_f(D_s)$ is the available density of fast (slow) trapping states and D_T is the density of available trion states, related to the doping level of the material, which was also extracted from the pulse excitation µ-PL measurements.

Adjusting the parameters of the model, the trion dynamics can quantitatively be reproduced. The result shown in Figure 20b uses the parameters summarized in Table 4. To ease interpretation of the results from the model, the excitation fluence is converted into the photon number per area. The photon density is $\approx 40 - 600 \times 10^{12}$ photons·cm^{-2}. Assuming an absorption of 10 % for a single layer, the pump introduces $4 - 60 \times 10^{12}$ excitations·cm^{-2}, which is on the same order of magnitude as the defect state density. Therefore, the slowing down of dynamics is not because of trion-trion interactions but is rooted in the filling up of the defect states, blocking the trapping

decay channels, leaving only the radiative decay channel, with a much longer decay time.

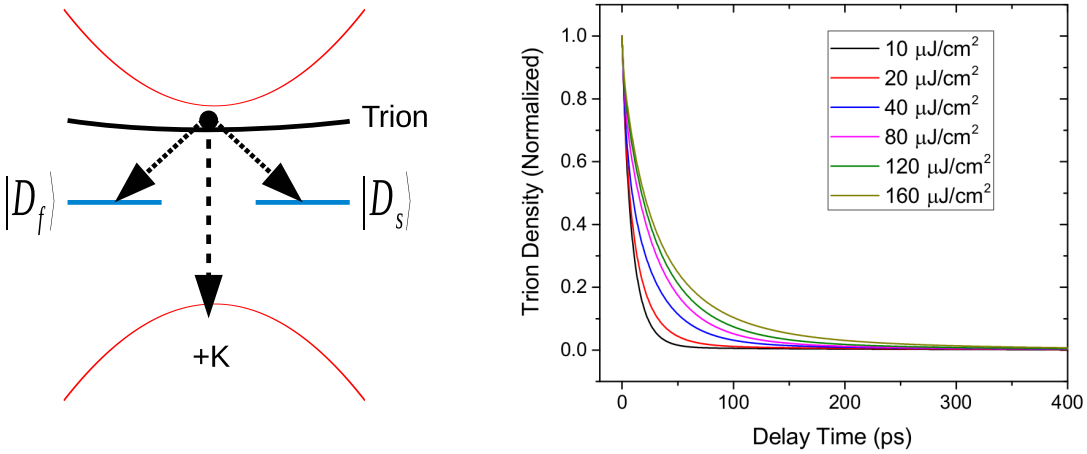

(a) (b)

Figure 20: (a) Energy level scheme of the model for simulating the trion dynamics containing two defect states. (b) Simulated trion dynamics. Adapted from [83] with permission.

Parameter	Value
$1/\Gamma_f^T$	10.3 ps
$1/\Gamma_s^T$	28.0 ps
$1/\Gamma_{XT}$	329 ps
$1/\Gamma_r^T$	500 ps
$1/\Gamma_r^X$	250 ps
D_f	1.58×10^{12} cm^{-2}
D_s	2.98×10^{13} cm^{-2}
D_T	5×10^{13} cm^{-2}

Table 4: Parameters used to model the pump-probe signal decay behaviour.

4.5 Conclusions

To summarize, in this section the incoherent population dynamics of trions in ML $MoSe_2$ was measured. The valley dynamics can not be probed with the used technique, since the valley relaxation either happens within the laser pulse duration or

no valley polarization can be created when exciting above resonance. The intravalley dynamics are explained by the existence of at least two different kinds of defect states which trap excitons on a picosecond timescale.

The trion formation dynamics are too fast to be resolved by the experiment, however, the upper limit on the valley exchange can be set to approximately 500 fs from the pump-probe measurement.

The trion relaxation was modeled with the rate equations presented in Equation 17, showing that there exist two types of defect states. The decay is dominated by trions filling up the two defect states, which leads to slower dynamics at higher excitation density. The long-term decay is explained by phonon-excited upconversion into excitons and excitons capturing excess charges, forming trions, as well as radiative decay of trions.

Population decay times obtained from the results in this section are essential to explain the coherence dephasing measured in the following section. Knowing that interaction of trions with defect states dominate the trion dynamics, the fast dephasing can be understood.

5 Coherence Time of Trions in Monolayer $MoSe_2$

5.1 Introduction

Although ML materials are promising candidates for device applications because of their reduced dimensionality and the possibility of forming heterostructures by stacking of MLs, the lower dimensionality comes at a cost. Owing to the maximally large surface-to-volume ratio, MLs are exceptionally sensitive to their surroundings. Efforts are being taken to use the high sensitivity to the ML environment for sensing applications, however, for other devices, especially with the goal of computing applications in mind, inhomogeneities of the substrate or the surroundings will affect the device performance more than with current bulk electronics. The PL linewidth of ML materials is much broader than their homogeneous linewidth, requiring to resolve the homogeneous linewidth even in the presence of strong inhomogeneous broadening. As discussed in Section 3, 2DCS is ideally suited for the determination of the homogeneous linewidth even in the presence of inhomogeneous broadening. Contrary to TI-FWM techniques, there is no ambiguity between homogeneously and inhomogeneously broadened systems, making it possible to measure the homogeneous linewidth in the presence of arbitrary inhomogeneous broadening [119]. Although a measurement of the homogeneous linewidth already contains information about the dephasing inside the material, in order to obtain a more meaningful result, it is necessary to measure a material property rather than a value dependent on the specific experimental conditions. Therefore the measured homogeneous linewidth is extrapolated to the linewidth in the absence of excitations and lattice vibrations. At finite excitation density, trions can elastically collide, leading to dephasing without energy transfer, called excitation-induced dephasing (EID). This effect is removed by taking a power dependence measurement of the homogeneous linewidth and extrapolating to zero ex-

citation density, corresponding to the linewidth of a single trion in the whole crystal lattice. Furthermore, phonons can elastically collide with a trion, also destroying the coherence. To rule out defects from phonon-induced dephasing (PID), a temperature dependence is measured in the same manner as for the excitation-induced effects and extrapolated to zero temperature, corresponding to a static lattice. The experimental procedure used for extrapolating to zero temperature is to obtain a power dependence measurement at multiple temperatures and extrapolate the zero-power result to zero temperature. The homogeneous linewidth obtained through this method is then the homogeneous linewidth of a single trion in a static lattice and therefore a material property. The variation between other measured linewidths is attributed to variations in the density of sample or substrate defects [15, 60–63].

5.2 Experiment

Ultrafast coherent spectroscopy is used to study the coherence time of trions in ML $MoSe_2$. The different approaches to performing 2DCS were discussed in Section 3.1.5. In this experiment, the non-collinear technique is used [28]. Recently a heterodyne detected collinear 2DCS technique was developed which proved to be especially suited for studying semiconductor nanostructures [64, 152]. The main challenge in performing 2DCS on ML materials lies in generating and detecting a sufficiently strong FWM signal since the absorption of a single ML flake is only ≈ 10 %, while ideal conditions for 2DCS are found for an absorption of ≈ 75 % [161, 162]. This section starts with a short introduction of the sample and preliminary data required for performing 2DCS is presented followed by a detailed introduction of the experimental setup used.

5.2.1 Preliminary Sample Characterization

The ML $MoSe_2$ that is used during the experiment was grown by CVD and subsequently transferred onto anti-reflection (AR) coated quartz glass [156]. The sample is shown in Figure 21a. The sample now is on an AR coated rather than uncoated glass substrate to suppress scatter of the pump beams. The sample size is again around 100 µm for each side of the triangle and it is again held inside a liquid helium cooled cryostat. Preliminary experiments include µ-PL measurements at different temperatures shown in Figure 21b. These measurements are used to confirm that the sample is indeed a ML. The main peak in the PL spectrum is assigned to the trion resonance, while the high-energy peak shoulder is ascribed to exciton emission. The PL spectra show a slight blueshift for lower temperatures as well as a larger amplitude. The center energy of the exciton resonance is approximately 1655 meV and the peak energy of the trion resonance is 1625 meV at 5 K. From the PL data a high doping level of either the sample or the sample substrate is expected due to the trion peak being much stronger than that from exciton emission. The excitation pulse for the 2DCS experiment is characterized using a home-built autocorrelation setup and is found to have a duration of ≈ 100 fs and can be approximated by a Gaussian shape.

The temperature dependence of the PL amplitude in ML-TMDs can be understood in terms of the relative energies of defect states and conduction band minima [163]. Controlling the defect density allows tuning of the quantum yield confirming the influence of defect states on the PL emission characteristics [141, 143, 164–166]. In $MoSe_2$ the increase of the PL amplitude at low temperatures is ascribed to the deactivation of scattering phonon modes as the temperature approaches zero leading to optically generated excitons and trions staying in a momentum allowed recombination region. Figure 21c shows the increase of the amplitude approximately follows that given by a Boltzmann factor with a phonon activation energy of 1.80 ± 0.33 meV. This value

is low compared to other reported phonon activation energies [167–169], probably because of the fact that the temperature dependence of the PL measurement was cut off at 60 K here. Including higher temperature PL data will give a more accurate value for the phonon activation energy.

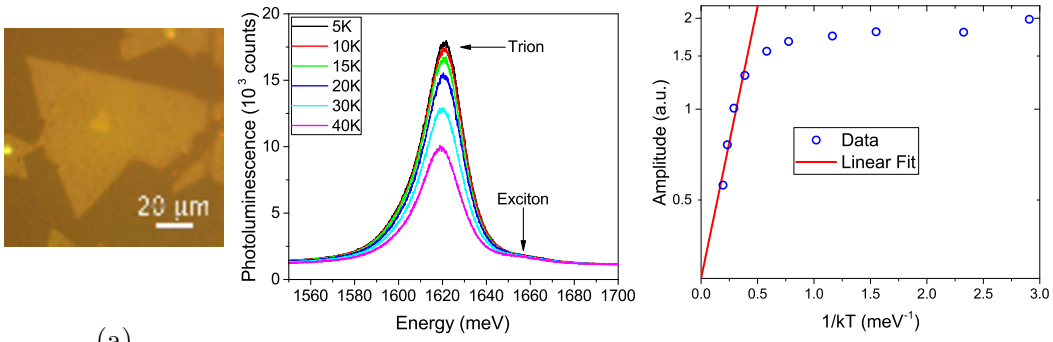

(a) (b) (c)

Figure 21: (a) Image of the $MoSe_2$ Sample on AR-coated glass. (b) Photoluminescence emission after 2.3 eV cw excitation at different temperatures. The exciton and trion resonances are highlighted. (c) Temperature dependence of the PL amplitude with the linear fit used to estimate the phonon activation energy.

5.2.2 Two-Dimensional Coherent Spectroscopy

In the experiment, a single laser pulse gets split into four pulses labeled $A - D$ with controllable time delays and active phase-stabilization. Copropagating with the pulses is a cw laser which is used for phase-locking the experiment even when using long pulse delays. The four pulses are aligned to the corners of a square with sides 2.5 cm in length as shown in Figure 11. Three beams are then focused onto the sample where a FWM signal is generated.

Only the signal in the phase-matching direction $\vec{k}_s = -\vec{k}_A + \vec{k}_B + \vec{k}_C$ is collected by placing an iris in the signal beampath, minimizing noise from scatter or fluorescence. The positioning of the iris is critical for successfully performing 2DCS on ML $MoSe_2$ because the noise background without an iris in place is too large, overshadowing any

FWM signal. Simultaneously, placing the iris at the wrong position will remove the highly directional FWM signal. To find the best place for the iris in the FWM signal pathway, 2DCS or TI-FWM is first performed on an atomic vapor with strong FWM signal and the iris position is optimized using the FWM signal from the atomic vapor. Then the atomic vapor is replaced with the ML sample of interest.

The fourth pulse is routed around the sample and is used for heterodyne detection and SI of the signal. A part of this fourth pulse is also split off in order to lock the phase between the signal and the reference pulse, since the two pulses do not share the same beam path. The signal and reference pulses are overlapped on a CCD coupled to a spectrometer and their interferogram is recorded. To improve the signal-to-noise ratio the phase-cycling scheme presented in Section 3.1.5 is used such that any linear contributions to the signal get cancelled out when adding the phase-cycled spectra. Timecuts are then implemented through software in order to further reduce the noise background. To acquire a 2D spectrum, the time delay between two pulses is stepped and the resulting FWM signal is subsequently Fourier transformed such that a 2D map in the frequency domain is created showing the resonances and their correlations.

The pulse ordering used to create the FWM signal is shown in Figure 4. For the signal emitted in the phase-matching direction, this means that pulse A acts as the conjugated pulse. It excites a coherent polarization in the sample that will oscillate at the field frequency. Pulse B interacts with the polarization and creates a population grating. The grating gets created due to the crossing angle between the pulses, which means that the phase between pulses A and B changes throughout the irradiated sample area. Pulse C then scatters off the grating which is detected as the FWM signal. In order to get a 2D spectrum the signal emission time is time-resolved using SI between the signal and reference pulse and pulse A is scanned earlier revealing the coherence dephasing dynamics.

5.3 Results

This section presents the results leading to the measurement of the intrinsic homogeneous linewidth in ML $MoSe_2$. First, the 2D spectra are shown which are then fit along the cross-diagonal for extraction of the homogeneous linewidth using the equation derived in Section 5.3.2. Then the power dependence used to extrapolate to the case of a single trion in the crystal lattice is presented which is followed by the temperature dependence used to extrapolate to zero temperature. The result obtained for the homogeneous linewidth of trions corresponds to a single trion in the crystal without any crystal movement and is therefore a sample specific intrinsic property and independent of the experimental conditions. However, in order to obtain a more clear picture, samples with variable defect levels would need to be measured as well to gain access to the dependence of the homogeneous linewidth on the availability of defect states.

5.3.1 Two-Dimensional Spectra

The homogeneous linewidth can be extracted from the cross-diagonal linewidth in a 2D spectrum [125]. When the pulses in a 2DCS experiment are much shorter than the measured decoherence times the pulses can be treated as δ-pulses, which has been done in Section 3. However, in the present experiment a dephasing time on the same order as the pulse duration is measured. Therefore excitation can no longer be treated as being in the short-pulse limit and the resonance shape derived in Section 5.3.2 needs to be considered. The finite pulse effects can be summarized by two main effects. Firstly, the lineshape is convoluted with the pulse spectral profile, leading to a sharper cutoff at the wings. Secondly, the phase of the spectra is changed, which is not considered in this case, since only amplitude spectra are presented.

A typical 2D spectrum is shown in Figure 22. The x and y axis correspond to

the emission and absorption axis of the investigated resonance. The only feature in the acquired 2D spectra is a single resonance on the diagonal line indicated by the white dashed line. The linewidth of the resonance in the diagonal direction is limited by the excitation laser bandwidth which is shown in the top of Figure 22 as the blue curve. In the cross-diagonal direction the linewidth of the resonance is related to the dephasing rate.

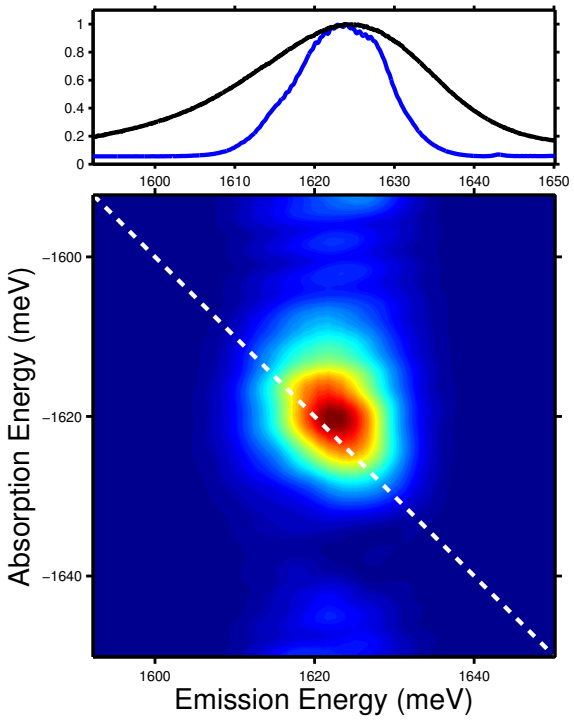

Figure 22: Typical 2D spectrum obtained for the trion resonance. The black curve in the top part shows the PL spectrum for the energies shown in the 2D spectrum. The blue curve is the lineshape of the excitation laser pulse. The white dashed line is the diagonal direction corresponding to absorption and emission at the same energy.

In order to extract the homogeneous linewidth, a slice through the center of the 2D spectrum is taken along the cross-diagonal direction. The data along the cut is then fit with the function in Equation 23 and the fit parameters are extracted. The free parameters contributing to the cross-diagonal lineshape are the homogeneous linewidth Γ, the population decay rate γ, the amplitude S_0 and an offset z_0. The

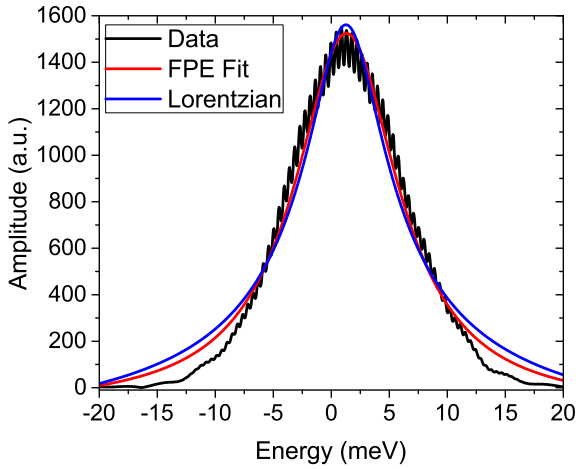

Figure 23: Slice taken through the center of the spectrum in Figure 22 with a fit according to Equation 23 (red curve) as well as a fit to a square-root of a Lorentzian (blue curve).

parameter σ is the excitation pulse duration and is set to 100 fs as was measured from autocorrelation. Since this parameter was measured, it is held fixed during the fitting. The parameter ω_{10} is the center energy of the excitation laser and is set to 1625 meV. Figure 23 shows the data taken from a slice through the center of the spectrum shown in Figure 22 alongside the fit using the function in Equation 23 and a fit with a pure Lorentzian function for comparison. It can be seen that the pure Lorentzian overestimates the signal at the wings as well the peak maximum while the fit function that was used for the analysis decays more rapidly and has a lower maximum value.

5.3.2 Fitting a Cross-Diagonal Slice

As discussed in Section 5.1, the coherent dynamics in ML-TMDs are on the order of hundreds of femtoseconds, being within the same timescale as the excitation pulse used in this experiment. To completely capture the dynamics, the effects due to the finite pulse duration are explicitly modeled into the linewidth measurement. This section briefly discusses how a cross-diagonal slice of a 2D spectrum is fit when the

coherence dephasing time is on the same order as the pulse duration. In order to simplify the calculations, only the case of a two-level system with ground state $|0\rangle$ and excited state $|1\rangle$ is considered. A detailed treatment can be found in Refs [170, 171]. The discussion here is adapted from [170].

The effect of excitation with a finite pulse compared to excitation with a δ-pulse can be summarized by bandwidth limitation. While a δ-pulse contains equal spectral power for arbitrarily high and low frequencies, a finite pulse has a certain bandwidth, which is typically non-uniform in the spectral domain. The finite pulse effect is mathematically described by the convolution integral between the signal shape and the excitation pulse shape and is performed in the time-domain. The pulses used in the experiment have Gaussian shape and are close to transform-limited pulses meaning that the spectral power is largest close to the central frequency and decays rapidly when going away from the central frequency. Therefore processes with a broad absorption spectrum are only probed within the bandwidth of the excitation pulses. The same reasoning holds for processes having a broad emission spectrum, since the signal is measured by heterodyne detection with a reference pulse, which has the same bandwidth as the excitation pulses. Hence any spectral features outside the bandwidth of the laser pulse will not be resolved. Furthermore, the convolution integral introduces a non-uniform phase-shift, which is not resolved in the 2D spectra discussed here, since only the amplitude is considered.

Starting with a semi-classical model and solving the OBE perturbatively yields the n-th order density matrix

$$\rho_{ij}^{(n)}(t) = -\frac{i}{\hbar}\int_{-\infty}^{t}[\hat{V}(t'),\hat{\rho}^{(n-1)}]_{ij}e^{-i\Omega_{ij}(t-t')}dt' \tag{18}$$

where $i, j = 0, 1$. The parameter Ω_{ij} is again defined through the transition frqeuency ω_{ij} as in Equation 12. The relaxation matrix elements are now redefined such that

Γ corresponds to the coherence dephasing rate while γ is the population relaxation time.

$$\Omega_{ij} = \begin{cases} \omega_{ij} - i\Gamma & \text{if } i \neq j \\ -i\gamma & \text{if } i = j \end{cases}. \tag{19}$$

The interaction Hamiltonian $V(t)$ contains the electric field and is given as

$$V(t) = -\mu_{01}[E(t)e^{i(\vec{k}\cdot\vec{r}-\omega t)} + \text{c.c.}] \tag{20}$$

with the transition dipole moment μ_{01} and the slowly varying envelope of the electric field $E(t)$.

Assuming that the pulses have transform limited Gaussian shape, which is a good approximation to the experimental pulse shapes, the electric field envelope for each pulse is written as

$$E_i(t) = \frac{E_i^0}{\sqrt{2\pi}\sigma} e^{-\frac{(t-t_i)^2}{2\sigma^2}} \qquad i = A, B, C \tag{21}$$

with σ being expressed through the intensity duration full width at half maximum $\Delta t_{\text{FWHM}} = 2\sqrt{\ln(2)}\sigma$ and the t_i being the arrival times of the different pulses. Plugging in the pulse shapes and selecting only the signal in the phase-matching direction $\vec{k}_S = -\vec{k}_A + \vec{k}_B + \vec{k}_C$, Equation 18 is modified to

$$\begin{aligned} \rho_{01}^{(3)}(t) \propto & \mu_{01}^3 \int_{-\infty}^{t} dt''' e^{-\frac{(t''')^2}{2\sigma^2}} e^{(i\omega_{01}-\Gamma)(t-t''')} \\ & \times \int_{-\infty}^{t'''} dt'' e^{-\frac{(t''+T)^2}{2\sigma^2}} e^{-\gamma(t'''-t'')} \\ & \times \int_{-\infty}^{t''} dt' e^{-\frac{(t'+T-\tau)^2}{2\sigma^2}} e^{(-i\omega_{01}-\Gamma)(t''-t')}. \end{aligned} \tag{22}$$

Since only the relative arrival times matter in terms of the material response, the pulse arrival times have been replaced with the time delays. The delays are defined as $\tau = t_B - t_A$, $T = t_C - t_B$ and $t = t - t_C$ where t is the emission time of the signal and the t_i correspond to the arrival time of pulse i. To perform the three integrations the convolution theorem is used, which states that the order of integration between FT integral and convolution integral can be switched. First the FT along the ω_τ direction is performed, followed by the integral over t'

$$\rho_{01}^{(3)}(t) \propto \mu_{01}^3 \int_{-\infty}^{t} dt''' e^{-\frac{(t''')^2}{2\sigma^2}} e^{(i\omega_{01}-\Gamma)(t-t''')}$$

$$\times \int_{-\infty}^{t'''} dt'' e^{-\frac{(t''+T)^2}{2\sigma^2}} e^{-\gamma(t'''-t'')}$$

$$\times \frac{1}{\omega_\tau - \omega_{01} + i\Gamma} e^{-\frac{\sigma^2\omega_\tau^2}{2}}.$$

The integral over t'' is a Gaussian integral

$$\rho_{01}^{(3)}(t) \propto \mu_{01}^3 \int_{-\infty}^{t} dt''' e^{-\frac{(t''')^2}{2\sigma^2}} e^{(i\omega_{01}-\Gamma)(t-t''')}$$

$$\times \left(1 + \operatorname{erf}\left(\frac{T + i\sigma^2\left(\omega_t + \omega_\tau - 2\gamma\right)}{2\sigma}\right)\right)$$
$$\times \frac{1}{\omega_\tau - \omega_{01} + i\Gamma} e^{-\frac{\sigma^2\omega_\tau^2}{2}}.$$

Lastly the integral over t''' is performed and the absolute value of the expression is taken, such that the final result is the response function in the 2D frequency domain

used for fitting

$$S(\omega_t, T, \omega_\tau) = S_0 \left| \frac{i}{(\omega_t - \omega_{10} + i\Gamma} \frac{i}{\omega_\tau - \omega_{01} + i\Gamma} e^{-\gamma T} \right.$$

$$\left. \left(1 + \mathrm{erf}\left(\frac{T + i\sigma^2\left(\omega_t + \omega_\tau - 2\gamma\right)}{2\sigma}\right)\right) e^{-\frac{\sigma^2(\omega_t-\gamma)^2}{2}} e^{-\frac{\sigma^2(\omega_\tau-\gamma)^2}{2}} e^{-\frac{\sigma^2\omega_\tau^2}{2}} \right|.$$

An offset z_0 is added into the equation to capture the fact that experimental background is nonzero. Since $T = 0$ in all experiments presented, the equation can be written as the following two-dimensional equation

$$S(\omega_t, \omega_\tau) = z_0 + S_0 \left| \frac{i}{\omega_t - \omega_{10} + i\Gamma} \; \frac{i}{\omega_\tau - \omega_{01} + i\Gamma} \right.$$

$$\left. \left(1 + \mathrm{erf}\left(\frac{i\sigma^2\left(\omega_t + \omega_\tau - 2\gamma\right)}{2\sigma}\right)\right) e^{-\frac{\sigma^2(\omega_t-\gamma)^2}{2}} e^{-\frac{\sigma^2(\omega_\tau-\gamma)^2}{2}} e^{-\frac{\sigma^2\omega_\tau^2}{2}} \right| . \quad (23)$$

In order to fit a cross-diagonal slice, the full dataset gets interpolated to a square matrix, in the case presented here, the matrix contains 2048×2048 entries, governed by the number of pixels of the CCD detector. Then the cross-diagonal is taken from the matrix corresponding to the cross-diagonal slice in the 2D figure. The slice is taken along the center of the spectrum through the point $(1620\mathrm{meV}, -1620\mathrm{meV})$. The same point is used to cut through the spectra in order to ensure that no shift along the trion resonance influences the measured linewidth [172].

The fitting parameters are the signal amplitude S_0, the offset $\omega_{10} = -\omega_{01}$ and the population as well as coherence decay rates γ and Γ, respectively. Furthermore an offset z_0 is included in the fitting which is due to the experimental background being nonzero and was added manually in Equation 23.

5.3.3 Power Dependence of TI-FWM and 2DCS signal

In order to prove the nonlinear nature of the signal, a power-dependence measurement of TI-FWM and the 2DCS experiment is performed. While the TI-FWM signal shows a large background, the 2DCS signal is able to extract the signal from the background showing a clear third-order nonlinear behaviour.

For nonlinear signals, the signal strength scales nonlinearly with the excitation field amplitude. While a first-order process has a linear dependence on the electric field meaning that the field emitted by a linear process E_{lin} is proportional to the input field E_{in}, for a third-order process this proportionality changes to $E_{\mathrm{third}} \propto E_{\mathrm{in}}^3$. Figure 24a shows a typical TI-FWM signal as well as the background. The data is fit with a Gaussian peak in order to average out the oscillations, which are due to interference between the excitation pulses and the signal. The area obtained from this fit of the TI-FWM signal is used to get a measurement of the signal strength. When increasing the laser power, the TI-FWM signal increases superlinearly as can be seen in Figure 24b where the green curve is added as a reference for a linearly increasing signal with the same offset as the one obtained from the linear fit to the data. The double-logarithmic plot reveals that the power dependence is approximately $E_{\mathrm{signal}} \propto E_{in}^{1.9}$, which is much less than 3, meaning that the measured signal contains a large amount of background due to scatter, which scales linearly. The scattered background can be detected by the TI-FWM setup and is shown as the black curve in Figure 24a. However, it can be concluded that there has to be some third-order signal, since the second-order signal vanishes along the observed direction in ML $MoSe_2$. Furthermore the power dependence for the 2DCS experiment is measured. To do so, the amplitude that was extracted in the fitting process described above is used and plotted as a function of input power. However, there is an intrinsic error associated with this method, since the amplitude has to be weighted by the amount of filters used in front

of the spectrometer, which were required in order to maintain the signal close to the maximum dynamic range. Although the filters were calibrated by comparing equal experiments with different filter settings, the fluctuation of the amplitude between different experiments was too large. Instead, the filters were calibrated by doing single shot measurements using the reference beam. The amplitude obtained from a single power dependence measurement is then scaled by the filters used and the power dependence of the measured amplitude is fit to the parabolic function $E_{\text{signal}} = AE_{\text{in}}^{n}$. The extracted parameters are given in Table 5 for power dependence measurements at different temperatures. Since the signal amplitude is plotted against the laser power, a third-order nonlinearity corresponds to $n = 1.5$ rather than $n = 3$ as was expected for the TI-FWM experiment, where intensity versus laser power was shown.

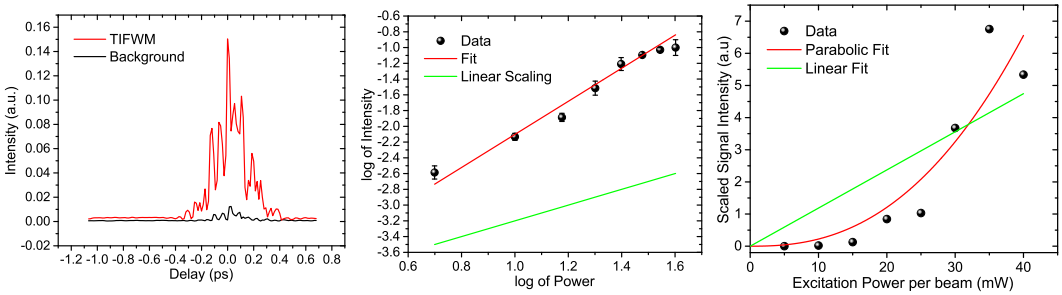

(a) (b) (c)

Figure 24: (a) TI-FWM and background trace as measured from the lock-in amplifier. (b) log-log plot of the power dependence of the area under the TI-FWM curve obtained from a Gaussian fit to the data at 5 K. (c) Power dependence of the extracted fit amplitude of 2D spectra at 5 K.

5.3.4 Power Dependence of the Homogeneous Linewidth

The homogeneous linewidth is measured at different excitation densities in order to get insight into the strength of EID and obtain the homogeneous linewidth at zero excitation density. The excitation density is estimated from the laser power, the focal spot radius, which was measured to be 35 µm using a microscope built into the 2DCS

Temperature	A	Exponent
5 K	62 ± 65	1.65 ± 0.30
10 K	43 ± 77	1.75 ± 0.50
15 K	34 ± 51	1.85 ± 0.41
20 K	24 ± 20	1.94 ± 0.23
25 K	36 ± 45	1.82 ± 0.35
30 K	31 ± 38	1.87 ± 0.34
35 K	47 ± 31	1.63 ± 0.19

Table 5: Nonlinearity fitting parameters

setup, and an absorption of 10% for a single layer of $MoSe_2$. The focal spot size is slightly smaller than the sample size as can be seen by comparison with Figure 21a. The excitation dependence of the homogeneous linewidth is shown in Figure 25 where the data points are averages between multiple measurements and the error bars their corresponding standard deviations. It can be seen that the homogeneous linewidth increases linearly with excitation density. The slope is the strength of EID and at 5 K is measured from a linear fit to the data to be 2.10 ± 0.23 μeV·cm^{-2}.

5.3.5 Temperature Dependence of the Homogeneous Linewidth

The excitation density dependence is repeated at different temperatures and the intercept is extracted at each temperature. The resulting zero excitation density linewidths are shown in Figure 26 with their corresponding fit uncertainties. The zero excitation density homogeneous linewidth shows a linear dependence on the temperature. From a linear fit to the data the strength of PID can be obtained as 8.2 ± 1.6 μeV·K^{-1}. The intercept of the temperature dependence yields the intrinsic homogeneous linewidth which is measured to be $\Gamma_{\text{in}} = 3.60 \pm 0.04$ meV. This linewidth corresponds to a dephasing time of $T_2 = 182 \pm 2$ fs.

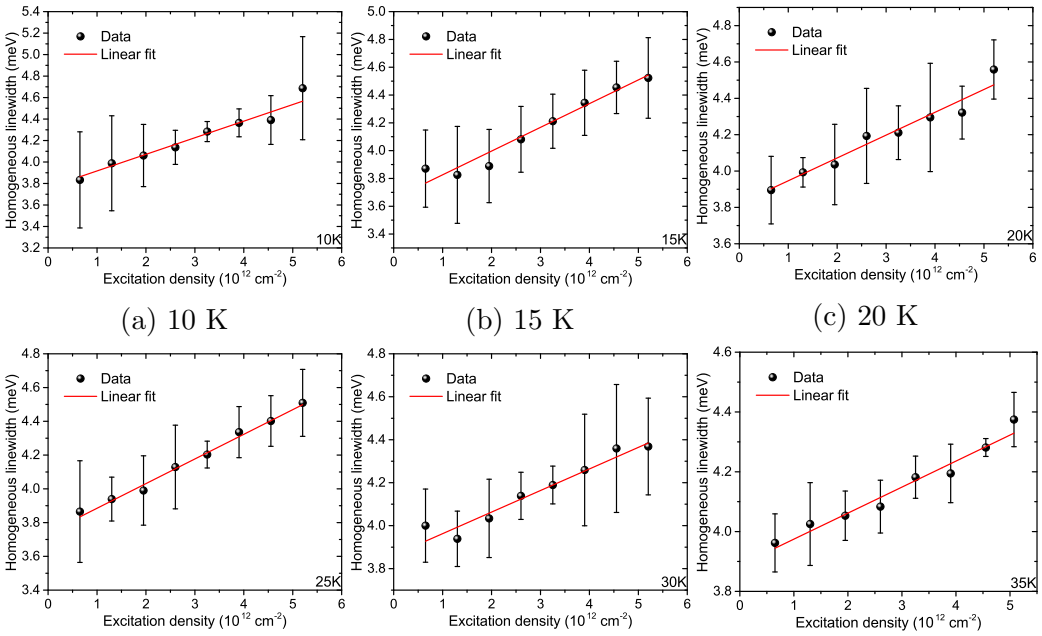

(a) 10 K (b) 15 K (c) 20 K

(d) 25 K (e) 30 K (f) 35 K

Figure 25: Power dependence of the homogeneous linewidth at different temperatures.

5.3.6 Exciton Results

In addition to the trion resonance excitons in ML $MoSe_2$ were investigated. However, only an upper bound on the intrinsic homogeneous linewidth can be given, since the measured linewidth corresponds to a decoherence time equal to or smaller than the laser pulse duration.

This result could be due to two reasons. Firstly, the PL from the exciton resonance in the sample used is much weaker than the emission from the trion resonance as can be seen in Figure 21b. Therefore it is also expected that the FWM signal of the exciton resonance is weak, even under resonant excitation. It is possible that even though the decoherence time of excitons is longer than the pulse duration, the coherence time can not be resolved by the experiment because of the signal being buried in too much background noise. Secondly, the laser bandwidth is narrower at the more blueshifted exciton resonance due to technical limitations of the laser itself. This leads to a pulse

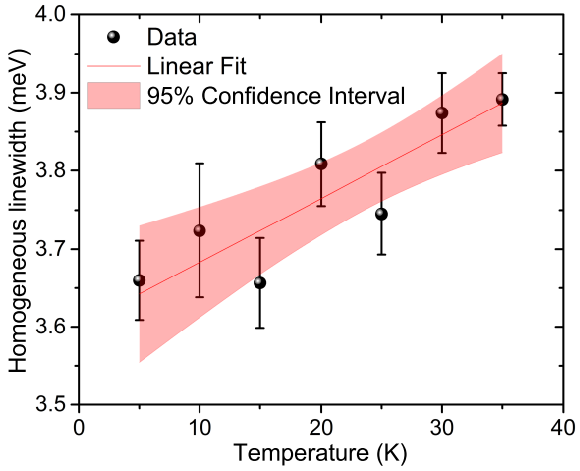

Figure 26: Temperature dependence of the homogeneous linewidth at zero excitation density extrapolated from the results shown in Figure 25. The error bars correspond to the uncertainty of the intercept obtained from the linear fits shown in Figure 25.

duration that is most likely equal to or longer than the decoherence time. The laser pulse duration as measured from autocorrelation is 158 fs. However, the linewidths extracted using the same fitting routine as was used for trions taking into account finite pulse effects, the measured decoherence times are between $140 - 170$ fs.

The corresponding data is presented in Figure 27 showing no clear change over the available excitation densities.

Extrapolating to zero power for each set yields the temperature dependence that is shown in Figure 28, which suggests a negative slope for phonon-induced dephasing. However, as noted above, the pulse duration is equal to or shorter than the signal decay time and therefore the measured dephasing time of excitons is only an upper limit for the coherence lifetime assuming that the measured result is due to the decoherence and not just background noise.

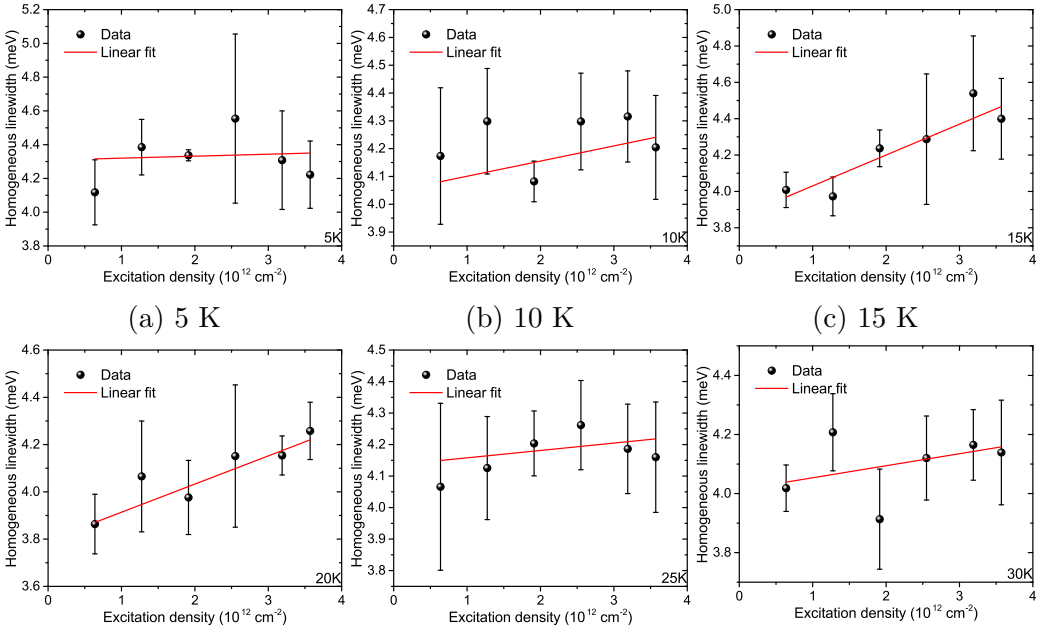

(a) 5 K (b) 10 K (c) 15 K

(d) 20 K (e) 25 K (f) 30 K

Figure 27: Excitation density dependence of the homogeneous linewidth of the exciton resonance at various temperatures used for calculating the temperature dependence of the homogeneous linewidth shown in Figure 28.

5.4 Conclusion

A 2DCS study of the dynamics of trions in ML-TMDs was performed giving the example of $MoSe_2$ as one representative material of the class of ML-TMDs. The intrinsic homogeneous linewidth was measured showing an ultrafast dephasing of 182 fs. Due to the dephasing time being on the order of the pulse duration the effect of the pulse was explicitly considered in the analysis. In addition to the intrinsic dephasing time the effects of EID and PID were measured by performing temperature and excitation dependence measurements of the homogeneous linewidth. Comparing this result to the ultimate limit on the dephasing time, given by $\frac{1}{T_2} = \frac{1}{T_1} + \frac{1}{T_2^*}$, it is seen that the dephasing time is orders of magnitude smaller than the population decay time. As shown in Section 4, the trion decay dynamics are dominated by fast trapping

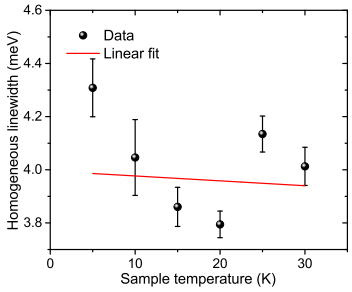

Figure 28: Extracted homogeneous linewidth at different sample temperatures based off of the results presented in Figure 27. Note that the extracted linewidths correspond to signal lifetimes equal to the laser pulse duration and the result can only be considered an upper limit of the exciton dephasing time.

in defect states. The fast dephasing can be explained by the defect states interacting with trions on an ultrafast timescale leading to dephasing without population decay.

6 Summary and Outlook

The present dissertation has investigated the coherent and incoherent dynamics of trions in ML $MoSe_2$ as a representative of the class of ML-TMDs. Trions have previously been found to strongly modify the optoelectronic properties of ML-TMDs such that an understanding of these quasiparticles is necessary for device applications. Gaining insight into the incoherent dynamics is essential for determining the suitability of the material as an information processing platform. Information encoded into the carriers, such as valley polarization, can at most exist for as long as the population lifetime. However, it was shown that it is impossible to nonresonantly excite a valley polarization with measurable lifetime. The dynamics study reveals that the trion dynamics are dominated by decay into nonradiating defect states which have a density of $\approx 10^{13}$ cm^{-2} inside the sample used. The defect density is comparable to the excited carrier density and the dynamics slow down at higher excitation densities due to filling up of the defect states.

The coherent dynamics of trions were studied using 2DCS, a spectroscopic tool that, in contrast to one-dimensional FWM techniques, can unambiguously determine the coherence time even in the presence of inhomogeneous broadening. The decoherence time was found to be limited by pure dephasing, likely due to trions interacting with the defect states revealed by the incoherent dynamics study without population transfer. The result presented here fits well into works of other groups and it can be concluded that in bare ML-TMDs the coherence time is intrinsically on the order of a few hundred fs. A first step in increasing the coherence time has been taken by encapsulating ML-TMDs in hexagonal Boron-Nitride leading to an increase of the dephasing time by at least a factor two. Future studies will also investigate the coherence time of excitons in heterostructures of ML-TMDs. Interlayer excitons in TMD heterostructures have an increased lifetime on the order of nanoseconds and

potentially will also have a longer coherence time than their intralayer counterparts, paving the way for coherent information processing in TMDs. Furthermore, quantum dots have been shown to lead to a narrowing of the PL linewidth associated with an increased lifetime on the order of nanoseconds. Again, future experiments will reveal the coherence time of these interlayer exciton states. Another interesting approach to increasing the coherence time in ML-TMDs may lie in the use of defect states as the platform for coherent manipulation. First experiments have shown that defects in ML-TMDs can have a lifetime of nanoseconds, at least an order of magnitude longer than the measured lifetime of excitons and trions excited in the bulk crystal. Although the coherence time of defects in ML-TMDs has not yet been measured, results on the coherence time of quantum dots in GaAs have shown that the zero-dimensional confinement can increase the coherence time by orders of magnitude.

Although ML-TMDs have ideal properties for a semiconductor and one molecular layer having a thickness of only three atoms or about $7 - 10$ Å [173] already absorbs approximately 10 % of the incoming light, the utility of the material thus far is limited because of the relatively low quantum efficiency. Combined with the low light absorption which can not easily be increased by stacking multiple layers as the optical properties change in bi- and multilayer structures, optical investigation of ML-TMDs remains challenging. Still, a large research effort is being taken to improve understanding of ML-TMDs and transfer them from labs to device applications.

A Collinear Spectroscopy of Encapsulated Monolayer $MoSe_2$

This section discusses results obtained by performing collinear spectroscopy on encapsulated MLs. The results are in disagreement to those reported by others concerning the linewidth narrowing, probably because of a different fabrication technique.

A.1 Introduction

As shown in Section 5, the coherence time of trions in ML-TMDs is on the order of 100s of femtoseconds. This timescale is too short for any device application. It is already known, that defects largely affect the trion dynamics in ML-TMDs, as discussed in Section 4 and towards the end of Section 5. Because of the maximal interfacial area of single-layer crystals with the substrate and environment, one can expect that irregularities in the substrate and interaction with the environment will readily act as defect locations for trions generated in the ML. To avoid interaction with these external defects, ML-TMDs can be encapsulated in hexagonal Boron-Nitride (hBN), which has been shown to have excellent surface quality and low defect density. Encapsulation in hBN therefore decouples the ML-TMD from possible substrate defects. Furthermore, the coupling to the environment is reduced by capping the ML-TMD with another film of hBN on top of the ML [174, 175]. Another beneficial effect lies in the fact that encapsulated samples have enhanced resistance to photodegradation [176]. The effect on the lifetime and coherence time of excitons upon encapsulating a ML in this way has been studied, and it has been found that the coherence time approaches the homogeneous limit [64]. Contrary to the samples previously studied in this dissertation, the flake size of encapsulated samples are on the order of a few µm, since the encapsulated ML-TMDs are mechanically exfoliated MLs, which are typically not found to be larger than 10 µm in sidelength. This prohibits the use of non-collinear 2DCS as the focal spot size would be much larger than

the sample area of interest and any FWM signal from the ML would be completely overshadowed by scatter from non-ML regions. Instead, PL detected collinear 2DCS is used, as described in Section 3.2.2. The spot size obtained using this technique is approximately 1 µm and much smaller than the samples of interest. Using collinear 2DCS it is therefore possible to study encapsulated flakes of exfoliated $MoSe_2$ MLs.

A.2 Experiment

The setup used in this experiment is a modified version of the photocurrent detected setup developed by Nardin *et al.* [29] for the detection of 2DCS from indium gallium arsenide quantum wells inside a device. This section first presents preliminary PL data used for finding the resonance of the $MoSe_2$ ML when encapsulated. Then the experimental setup used for PL detected 2DCS is discussed.

A.2.1 Sample description

The ML in this experiment has been exfoliated from a bulk crystal using mechanical exfoliation. The ML is then transferred onto a thick (100 nm) hBN film on a silicon substrate to isolate it from defects on the silicon surface. The ML flake is then capped using another hBN film with thickness of approximately 20 nm to isolate the ML from the environment. The total device structure is shown in Figure 29a. The most notable feature is that the flake is much smaller than those used in the previous experiments. Therefore, an almost diffraction limited spot size is necessary to investigate the encapsulated ML. Since the sample is now on silicon instead of a glass substrate, all experiments are performed in the reflection geometry as silicon is not transparent to the wavelengths used in the experiment.

A.2.2 Preliminary Experiments

The resonance of the encapsulated $MoSe_2$ ML is found using low-temperature µ-PL. The ML is excited by a 405 nm cw laser diode focused to a spot size of ≤ 1 µm. The PL signal from the ML is collected using an optical fiber and sent to a spectrometer. The result is shown in Figure 29b. Comparison with the PL data in Section 4 and Section 5 shows that the trion PL linewidth is mostly unchanged and the center energy of the PL is also the same for all temperatures. Comparing the relative strength of exciton and trion, it can be seen that the trion emission strength of the encapsulated sample ranges between that used in Section 4 and the one used in Section 5. The trion emission still completely dominates the PL spectrum. The overall preliminary characterization is in stark contrast to the reported results in [64]. However, even though the preliminary characterization points towards the sample being close to the samples already studied in the 2DCS experiment shown in Section 5, it is still of interest if the homogeneous linewidth becomes narrower in the encapsulated sample.

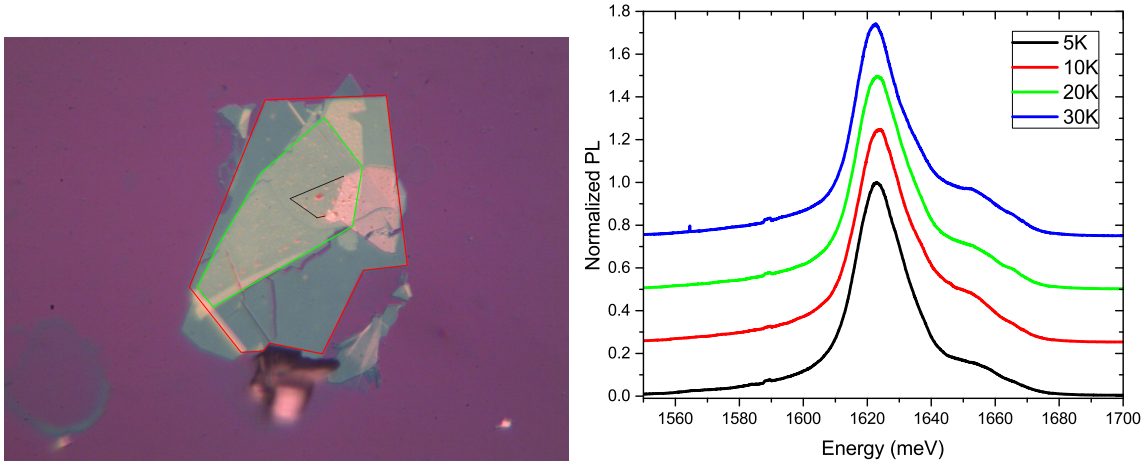

(a) (b)

Figure 29: (a) Microscope image of the encapsulated ML sample. The ML region is within the area highlighted by the black line. The two hBN films are outlined by the red and green lines. The longest side of the ML flake is approximately 27 µm. Photoluminescence emission from encapsulated $MoSe_2$ at low temperatures upon excitation with a 405 nm cw laser.

A.2.3 Collinear 2DCS

Upon having found the PL emission and therefore the resonances ascribed to exciton and trion in the encapsulated $MoSe_2$ ML, 2DCS is performed on the encapsulated flake. Since the flake is smaller than the focal spot size in the non-collinear setup used before, a collinear setup is used. The benefit of using collinear excitation lies in the possibility to focus the laser to a near diffraction-limited spot size by coupling the beams into a microscope objective. The objective used is the same 50× objective used in Section 4 allowing focal spot sizes estimated to be ≈ 1 µm and much smaller than the flake size of 10 µm per side.

The collinear setup splits one laser pulse into four copies with variable delay times. Copropagating with the pulse laser is a reference laser close to the center wavelength of the pulse laser. In this case, the pulse laser is blue-shifted from the trion resonance to 1630 meV while the reference laser is operating at a photon energy of 1620 meV. The blueshifting of the pulse laser is necessary to isolate the signal from the cw laser spectrum.

In contrast to the non-collinear setup, signal and excitation pulses are now co-propagating. To be able to isolate the signal from the background, frequency tagging of the pulses is used. This technique tags each of the four excitation pulses with a unique RF using AOMs. Mixing of the frequencies then results in a beat note at their respective difference frequencies. The beat frequency of the FWM signal is $\omega_s = -\omega_A + \omega_B + \omega_C - \omega_D$ where $A - D$ correspond to the beams $A - C$ and Ref in Figure 4.

Data is recorded by scanning two pulses in time. The pulse sequence shown in Figure 4 is extended by a fourth pulse arriving after pulse C with delay t. Then the delays τ and t are scanned to obtain a two-dimensional spectrum in the time-domain. The spectrum is then Fourier transformed along the two axes to obtain a

2D spectrum in the frequency domain. The optic pathlength is monitored by the reference laser copropagating with the pulse laser. To isolate the FWM signal of interest from linear contributions and other nonlinear signals the reference beat note is used as the reference frequency to a lock-in amplifier. The FWM signal is recorded on a photodetector where the electric fields optically mix and signal at the reference beat frequency is extracted with the help of the lock-in amplifier.

A.3 Results

Following the procedure outlined in Section 5, spectra are recorded at various excitation powers to isolate the zero excitation-density linewidth and remove EID effects. Then the experiment is repeated at different temperatures to extrapolate to the zero-temperature linewidth at zero excitation density, excluding PID effects. The excitation dependence is shown in Figure 30a and exhibits a linear increase upon increasing excitation, similar to the results obtained in Section 5. The large error at low excitation powers is due to the spectra becoming noisy at lower excitation densities since fewer trions are excited.

From the temperature dependence of the homogeneous linewidth the intrinsic homogeneous linewidth in an encapsulated $MoSe_2$ ML is found to be 5.75 ± 0.75 meV. This linewidth corresponds to a coherence time of 114 ± 16 fs, shorter than that of the non-encapsulated samples and much shorter than the values reported for excitons in encapsulated $MoSe_2$ MLs [64].

A.4 Discussion and Conclusion

In this section the intrinsic homogeneous linewidth of trions in encapsulated ML-TMDs was measured using $MoSe_2$ as a representative of the class of ML-TMDs. The measured coherence time of trions is shorter than that of a bare ML and much shorter

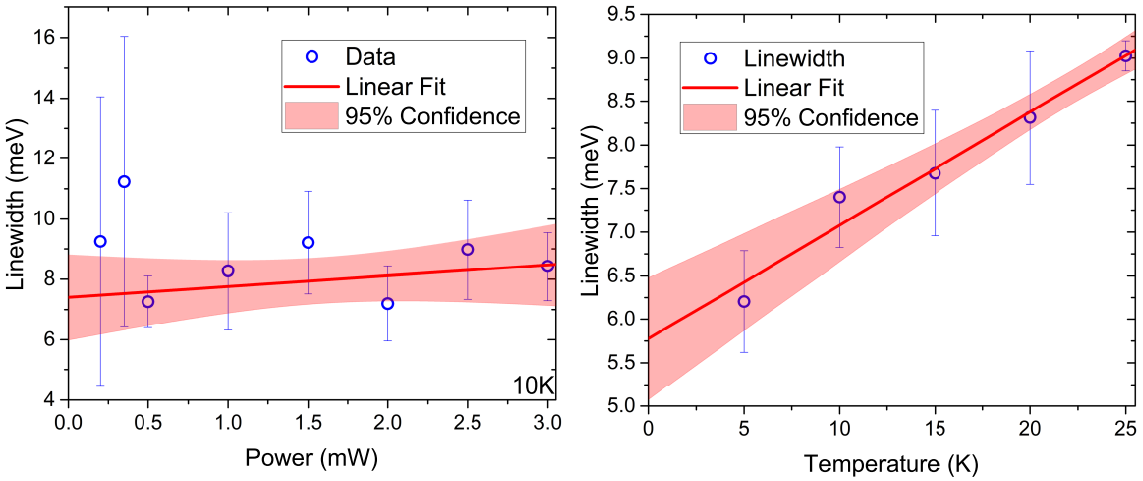

Figure 30: (a) Power dependence of the homogeneous linewidth of encapsulated $MoSe_2$ MLs at 10 K. (b) Temperature dependence of the homogeneous linewidth at zero excitation density. The datapoints and error bar are the y-intercept and corresponding error from the fit in Figure 30a.

than the reported coherence time of excitons in another encapsulated $MoSe_2$ ML. The PL emission in the ML used differs significantly from that of other encapsulated MLs. Most notably, the trion emission is much stronger than the exciton emission, in contrast to PL emission typically reported for encapsulated MLs. Since the substrate on which the ML flake is placed is now thick hBN which is known to have exceptional crystal quality, the PL emission can no longer be assigned to defects in the substrate. Instead, the large trion density is ascribed to defects in the ML flake itself or a different contact between ML flake and hBN substrate rooted in differences in the fabrication process.

B Detailed Discussion of the 2DCS Platform and Alignment Procedure

The non-collinear 2DCS setup has been introduced in Section 3 and Section 5, but the treatment has focused more on the physical processes involved in generating a signal in the phase-matching direction rather than focusing on the specific intricacies of the setup used to implement 2DCS in the presented experiment. This section is going to give a clear overview of the setup and then go on to give a step-by-step procedure for aligning the whole 2DCS system.

B.1 Experimental Setup

A schematic of the top and bottom decks used in the setup is shown in Figure 31 with labels for all optics. The input laser is split for the first time at the beamsplitter $BS1$. Half of the beam is sent to the top deck while the other half keeps propagating on the bottom deck. The bottom half of the beam is delayed using a long (15 cm) double-passing delay stage leading to a maximum total delay of 60 cm or 2 ns. The delayed beam is then sent to another beamsplitter $BS2$ where beams C and D are now generated. Beam C is sent through a glass plate to compensate for the dispersion with respect to beam D. Furthermore, the two mirrors $M6, M7$ before beam C leaves the instrument can be used to adjust the beam position and pointing. Beam D is sent to a second delay stage that can be used to adjust the delay of beam D independently and is reflected using a retroreflector. The retroreflector has the advantage of not requiring any alignment, but the disadvantage of giving little to no room for adjustment of beam pointing or positioning. The half of the input beam sent to the top deck is sent upwards through the use of a periscope consisting of mirrors $M8$ and $M9$. Half of the periscope is on the bottom deck and an iris can be attached for rough alignment of the upgoing beam. The beam coming up to the top deck can also be delayed using a manual stage, however, this capability has not

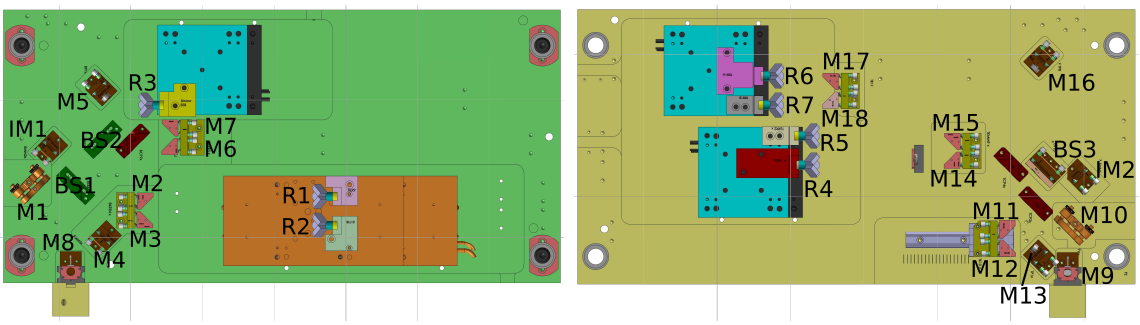

(a) (b)

Figure 31: (a) Bottom and (b) top deck of the 2DCS instrument.

yet been used. The beam is then sent through another glass plate to compensate the dispersion of beams A and B with respect to beams C and D that went through the first beamsplitter. The beam is then split on $BS3$ and the reflected part is sent to a glass plate to compensate the dispersion of beam B with respect to beam A. The total number of glass plates in each beam is four, therefore introducing the exact same amount of dispersion in each beampath, allowing the use of high bandwidth laser pulses in the setup without worrying about changes in dispersion between different beampaths. Beam B is sent to a double-passing delay stage after which it leaves the instrument. Beam A also traverses a double-passing delay stage and is then sent out of the instrument.

Although care was taken when designing the instrument, the stages are not perfectly parallel with respect to each other. However, with the retroreflectors, the only possibility is to align a beam to the stage and rely on the stage positioning inside the instrument, since the retroreflector does not have any way of adjusting the output beam. To improve on the adjustability of the output beams, an extension was developed adding two mirrors to each beampath while keeping the beams copropagating on a box of 2.5 cm sidelength. This extension allows compensation of any deviation of the delay stages from perfect parallelism while still maintaining the phase-lock between the beams.

B.2 Full Alignment Procedure

In this section the full alignment procedure is shown. Each step is clarified by its own drawing. This procedure should only be followed when the instrument has been moved or the internals of the instrument were changed. Otherwise, an alignment of the input beam and, if necessary, the extension, is sufficient for performing 2DCS. The section starts by explaining the blade-method used to ensure that a beam is parallel to a linear stage.

B.2.1 Alignment Using the Blade-Method

The blade method can be used whenever a beam needs to be made parallel to a linear stage, either automatic or manual. It uses the fact that the intensity of a Gaussian beam changes rapidly at the peak center.

To start, a new razor blade is fixed to an $x-z$ manual micrometer controlled stage and a power meter is set up behind the stage to be aligned as shown in Figure 32. The stage is set up such that the blade cuts off half of the beam in the horizontal direction. The stage to align to is then moved towards the mirror as much as possible and the blade position is adjusted until 50 % of the laser power are transmitted. Then the stage is moved to the other end such that the blade is as far away from the mirror as possible. Then the mirror is adjusted until half the laser power is transmitted to the power meter. This is iterated many times (typically about 10-50 times) until the power does not change when moving the blade along the whole stage travel.

After alignment in the horizontal direction, the beam must also be aligned to be vertically parallel to the stage. The blade is placed such that it cuts the beam in half along the vertical direction and the procedure explained above is repeated. Adjusting the mirror in the vertical direction leaves the horizontal direction unaffected such that now the beam is parallel to the stage both vertically and horizontally.

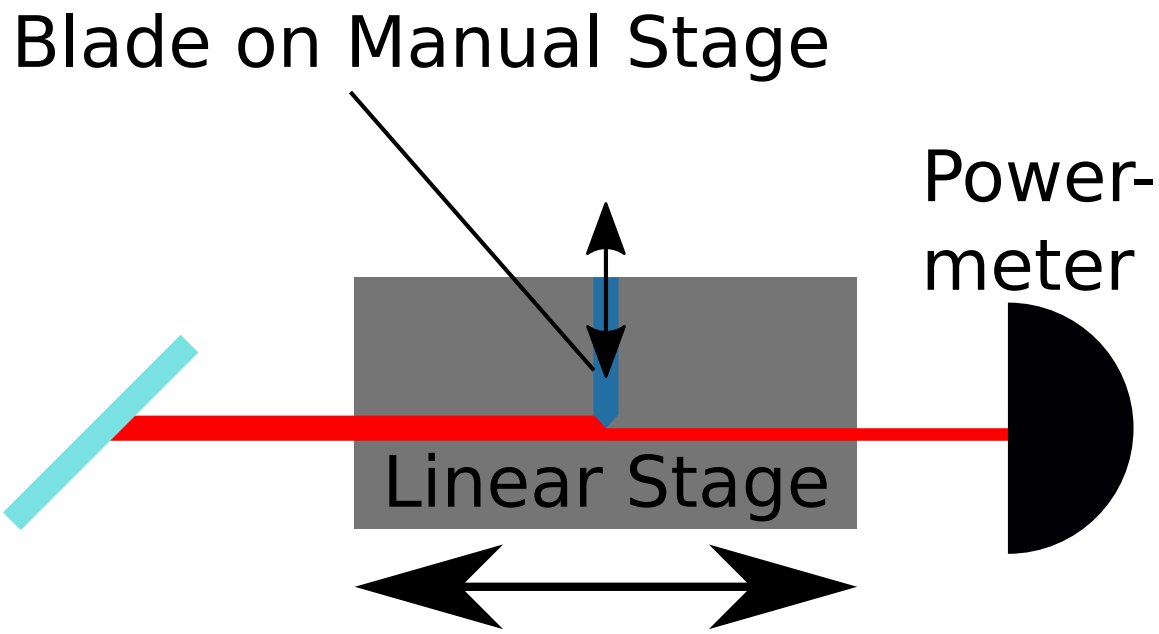

Figure 32: Schematic demonstrating the setup for adjusting a beam to be parallel to a linear stage.

B.2.2 Top Deck Alignment

To start alignment of the instrument, first the top and bottom deck need to be separated. The first step is removing the anodized aluminium panels enclosing the instrument. These are in place to block stray beams and reduce airflow inside the instrument. Afterwards, the four screws holding the two plates together should be removed, highlighted in red in Figure 33a. Then the four screws holding the two spacers highlighted by the white lines in Figure 33a are removed. The spacers will stay inside the instrument until the top deck is lifted since the top deck rests on the spacers now.

There are four screws supplied with the instrument which need to be used to lift the top from the bottom deck. A picture of the screws is shown in Figure 33b. The screws are inserted through the top deck at the holes highlighted in green in Figure 33a. When lifting the top deck, each screw should be turned by no more than one turn at a time. After turning one screw for one turn or less, the other three

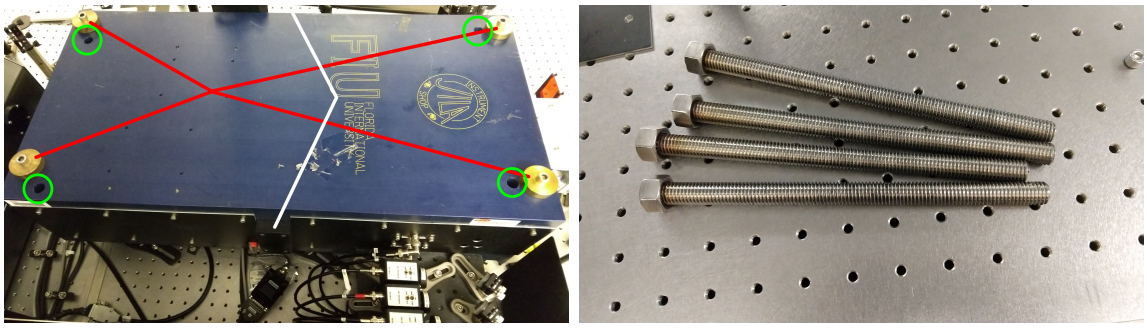

(a) (b)

Figure 33: (a) The closed instrument before opening. (b) The screws used to lift the top deck from the bottom deck.

screws should be turned by the same amount to ensure a homogeneous lifting of the top deck and avoid the top deck getting caught on the guiding pins.

After lifting the top deck high enough that it is completely lifted off the guiding pins the top deck can be moved by two or more persons using the supplied handles shown in Figure 34. The top deck will be aligned first, followed by the bottom deck.

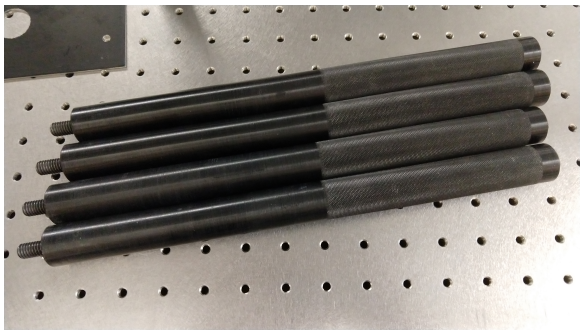

Figure 34: Handles used to lift the top deck.

Top-Deck Alignment

1. Remove the periscope mirror $M9$

2. Remove mirrors $M10$ and $IM2$ as shown in Figure 35

3. Center the beam on the iris at position $I11$ and the input

4. Replace mirrors $M10$ and $IM2$

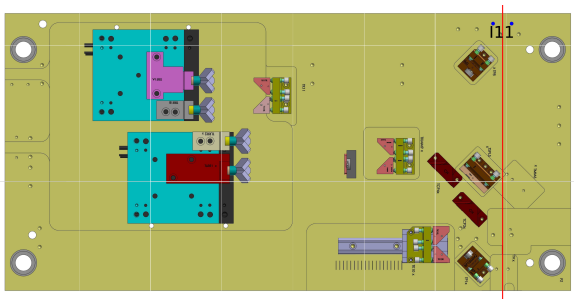

Figure 35: Top deck with the periscope mirror $M9$, input mirror $M10$ and interferometer mirror $IM2$ removed and the alignment beam path.

5. Remove the assembly holding mirrors $M11$ and $M12$

6. Center the beam on the iris at position $I12$ and $I13$ using only mirror $M10$

7. Replace the assembly containing $M11$ and $M12$

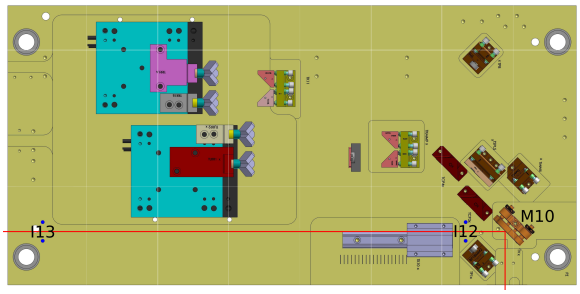

Figure 36: Top deck with the $M11$ and $M12$ assembly removed and the alignment beam path.

8. Remove mirror $M16$

9. Align the beam to pass through the iris placed at $I14$ using $M12$ and $I15$ using $M13$. Iterate this procedure as necessary. Note that the iris at $I14$ needs a cutout for the beam to pass through. The beamsplitter $BS3$ and the glass plate should not be removed.

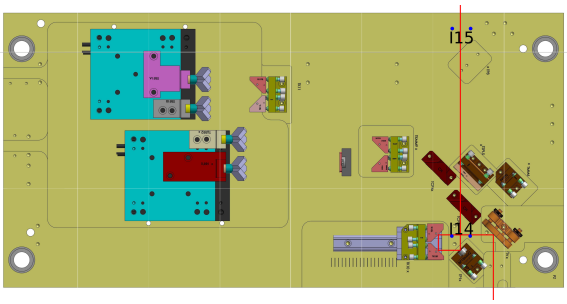

Figure 37: Top deck with mirror $M16$ removed and the alignment beam path.

10. Replace $M16$

11. Remove the retroreflectors $R4$ and $R5$

12. Use $BS3$ to align the beam through $I16$

13. Ensure the beam is parallel to the stage using the blade edge method explained in Section B.2.1

14. Confirm the beam still passes through $I16$ and use the third knob of $BS3$ to align to $I16$

15. Repeat steps 13 and 14 as necessary

16. Replace $R4$

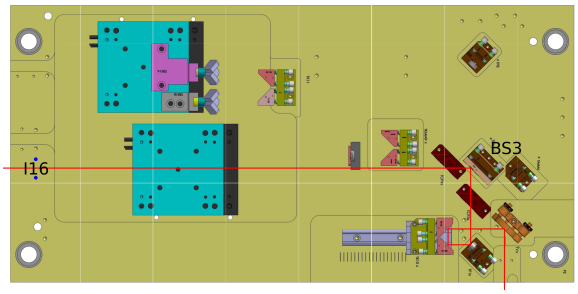

Figure 38: Top deck with retroreflectors $R4$ and $R5$ removed and the alignment beam path.

17. Use $M14$ to align the beam through iris $I17$

18. Use $M15$ to ensure the beam is parallel to the stage

19. Iterate steps 17 and 18 until the beam is passing through the iris and parallel to the stage

20. Replace the retroreflector $R5$

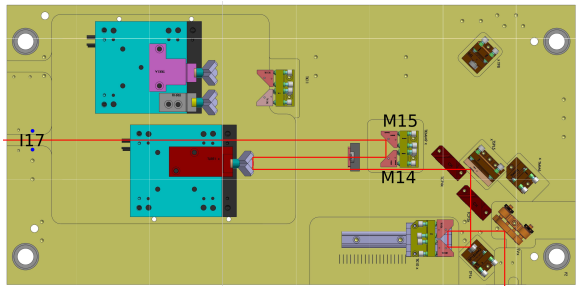

Figure 39: Top deck with retroreflector $R5$ removed and the alignment beam path.

21. Remove the retroreflectors $R6$ and $R7$

22. Use $M16$ to align the beam through iris $I18$

23. Use $M15$ to ensure the beam is parallel to the stage

24. Iterate steps 22 and 23 until the beam is passing through the iris and parallel to the stage

25. Replace $R6$

Now alignment of beam A is completed and the beampath up to $BS3$ is fixed and should not be touched any more.

26. Use $M18$ to ensure the beam is parallel to the stage

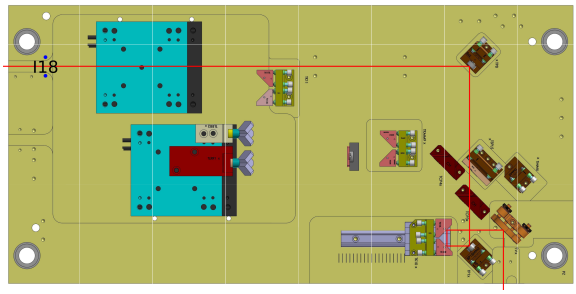

Figure 40: Top deck with retroreflectors $R6$ and $R7$ removed and the alignment beam path.

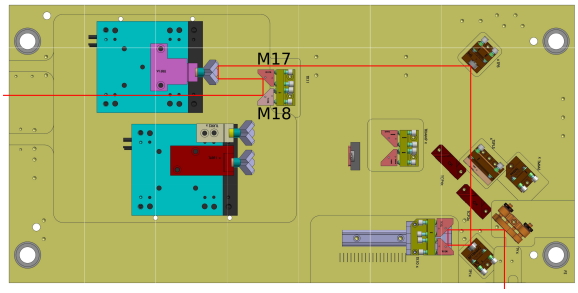

Figure 41: Top deck with retroreflector $R7$ removed and the alignment beam path.

27. Replace $R7$

28. Use $M17$ to align to the iris $I19$

29. Use $M18$ to ensure the beam is parallel to the stage

30. Repeat steps 28 and 29 until the beam is both parallel to the stage and going through iris position $I19$

31. Replace the periscope mirror $M9$

Now alignment of the top deck is done and the top deck is placed in a safe location until the bottom deck is aligned and the two parts are combined again.

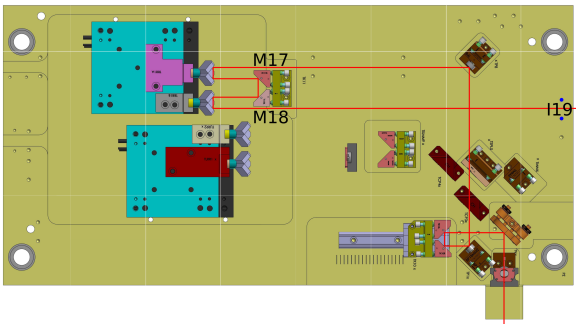

Figure 42: Final top deck beam path for beam B.

B.2.3 Bottom Deck Alignment

Before starting alignment of the bottom deck, the bottom deck should be moved to the location where it will be used later on, since input alignment to the bottom deck will be the final alignment used during experiments. Furthermore, for safety reasons, mirror $M8$ should be removed or covered.

1. Remove mirrors $M1$ and $IM1$
2. Align the input to irises placed at positions $I1$ and $I2$
3. Now fix the external input alignment using two irises for easy recovery in daily operation
4. Replace $M1$ and $IM1$
5. Remove retroreflectors $R1$ and $R2$
6. Use $M1$ to align to iris position $I3$
7. Ensure the beam is parallel to the stage using the blade method
8. Repeat steps 6 and 7 until the beam is both aligned to the stage and passes through $I3$

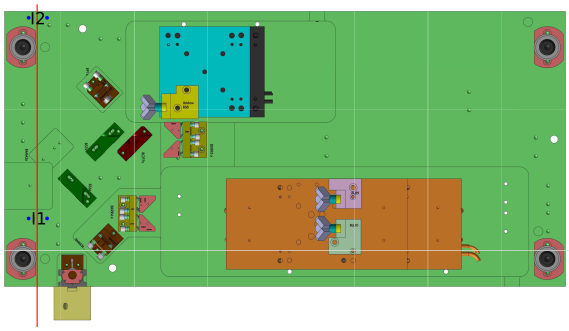

Figure 43: Bottom deck with input mirror $M1$ and interferometer mirror $IM1$ removed and alignment beam path.

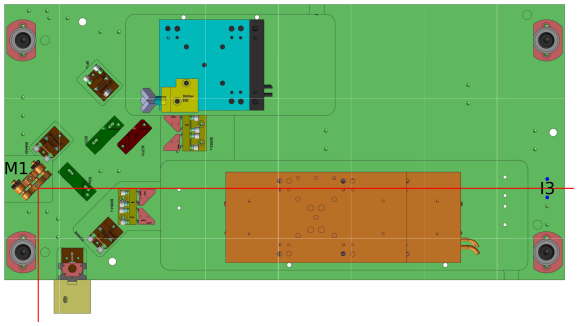

Figure 44: Bottom deck with retroreflectors $R1$ and $R2$ removed and alignment beam path.

9. Replace $R1$

10. Use $M2$ to align to iris $I4$

11. Use $M3$ to ensure the beam is parallel to the stage using the blade method

12. Repeat steps 10 and 11 until the beam is both parallel to the stage and passes through $I4$

13. Replace $R2$

14. Remove $M4$

15. Adjust the retroreflector $R2$ to make the beam pass through $I5$

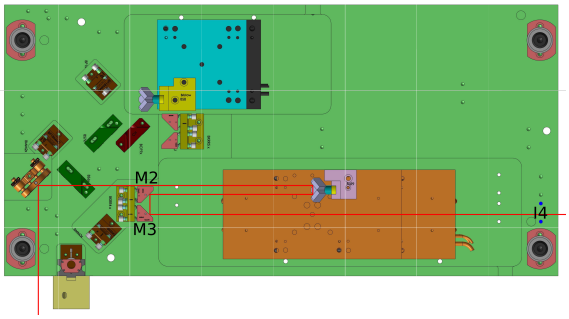

Figure 45: Bottom deck with retroreflector $R2$ removed and alignment beam path.

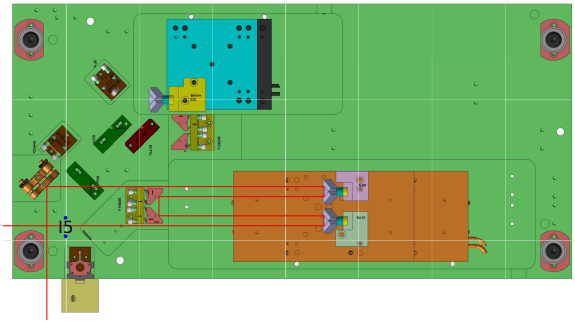

Figure 46: Bottom deck with mirror $M4$ removed and alignment beam path.

16. Replace $M4$

17. Remove $M5$

18. Use $M4$ to align the beam through $I6$ and $I7$

19. Replace $M5$

20. Remove $R3$

21. Use $M5$ to ensure the beam passes through $I8$

22. Use $M5$ to ensure the beam is parallel to the stage

23. Repeat steps 20 and 21 until the beam is both parallel to the stage and passing through $I8$

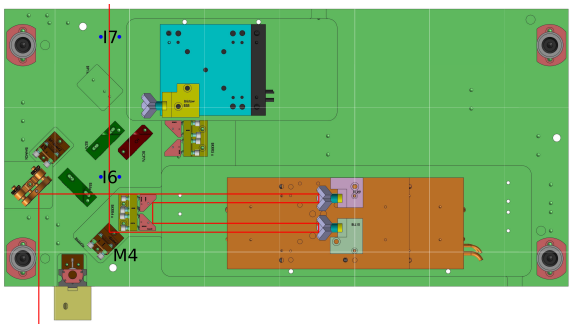

Figure 47: Bottom deck with mirror $M5$ removed and alignment beam path.

24. Replace $R3$

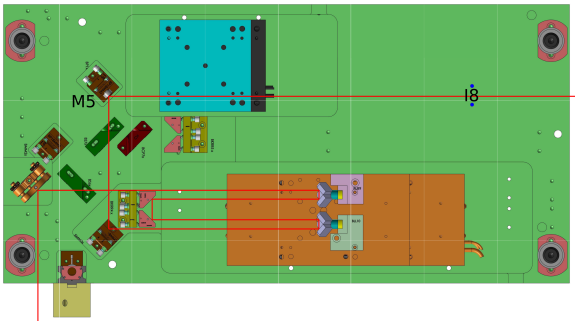

Figure 48: Bottom deck with retroreflector $R3$ removed and alignment beam path.

25. Adjust $R3$ to ensure the beam passes through $I9$

Now beam D is aligned which is used as the reference for aligning beam C.

26. Use $M6$ to align the beam through iris position $I10$

27. Obtain a 1 in. box

28. Place the box as far away from the instrument as possible such that beam D hits the bottom right corner

29. Use $M7$ to align the beam to the bottom left corner of the box

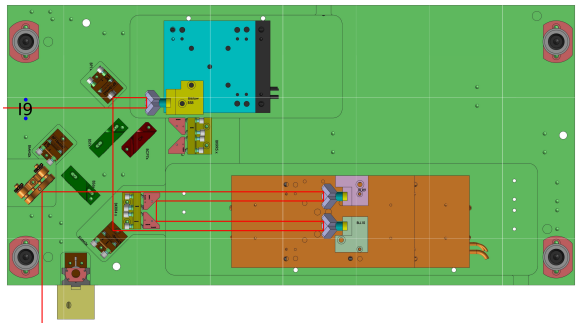

Figure 49: Final bottom deck beam path for beam D.

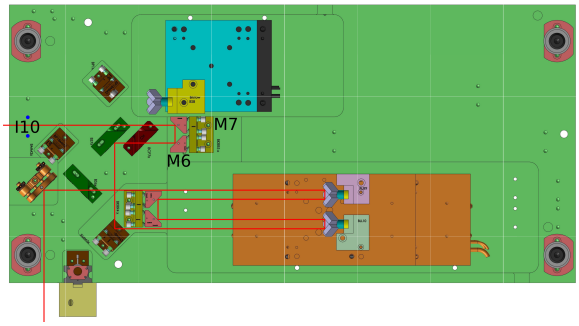

Figure 50: Final bottom deck beam path for beam C.

30. Repeat steps 25 and 28 until the beam passes through $I10$ and hits the bottom left corner of the box

31. Replace the periscope mirror $M8$

The alignment of the bottom deck is done and the top and bottom deck need to be put together. Before joining the two plates, make sure periscope mirrors $M8$ and $M9$ are in place.

B.2.4 Joining Top and Bottom Deck

The long screws used to lift the top deck up in Section B.2.2 are inserted into the top deck again and screwed all the way in, such that the screws will hold the top deck up when joining the two parts. Then the top deck is lifted up, flipped upside down and placed onto the bottom deck such that the holes receiving the guiding pins are

approximately overlapped with the pins. Then the lifting screws are retracted until the top deck starts touching the guiding pins. Now the top deck is aligned to the guiding pins more carefully to make sure the guiding pins enter straight. Furthermore the spacers highlighted in Figure 33a need to be inserted now. The lifting screws are then retracted exactly opposite as described in Section B.2.2, turning each screw no more than one turn at a time and ensuring that the top deck does not get caught on the guiding pins. The spacers can now be fixed, holding top and bottom decks at the correct separation. Also, the locking screws that were removed are put back in place.

Once top and bottom decks are put together again, the periscope needs to be aligned such that the input to the topdeck is recovered. To do this, a box is placed outside of the instrument as far away as possible and the bottom corners of the box are aligned to beams C and D. Then periscope mirror $M9$ is adjusted until A and B are on the top corners of the box. The box is then taken as close to the instrument as possible and the bottom corners are aligned to beams C and D again. $M8$ can now be used to improve overlap of A and B with the top corners of the box. Repeating this procedure beams A and B are eventually vertically parallel and exactly 2.5 cm above beams C and D. However, there is no way to adjust for any horizontal offset between the top and bottom deck using only the periscope for which the extension will be used.

Now the internals of the instrument are fully aligned and any further adjustment is going to be done either through external input alignment or using the extension.

B.2.5 Using the Extension

At this point the output should closely resemble a box with at most one beam of the top deck not being on a corner of the box while the other three are.

One beam that is vertically parallel to the table is chosen as the reference beam, in

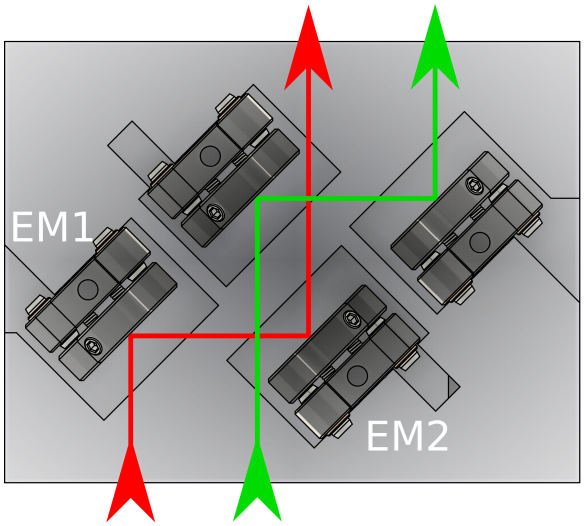

Figure 51: Bottom part of the extension with beam paths for beams C (red) and D (green).

this case it is assumed that beam D is used. The procedure is only explained for beam C deviating from the box but is exactly the same for all other beams and can be done simultaneously. To start, the box is placed as close as possible to the instrument and adjusted such that beam D is overlapped with the bottom right corner of the box. Any deviation of beam C from the box is compensated by adjusting mirror $EM1$. The box is then placed as far away as possible and moved such that beam D is on the bottom right corner again. Then mirror $EM2$ is used to overlap beam C with the bottom left corner again. This procedure is repeated until beam C is simultaneously on the corner of the box when placed close and far away from the instrument.

Now the four beams are at the correct separation and parallel to each other. In this configuration a FWM signal is propagating overlapped with the reference beam and can be found by aligning the reference beam to the spectrometer.

To confirm the overlap between all four beams at the focal plane, a system for imaging a replica focus is built into the setup. Using this any deviation between the four beams can be compensated. Still assuming that only beam C needs to be adjusted, the extension mirror $EM2$ can be used to overlap beam C with beam D.

The output from the instrument should again be checked by placing a box as close as possible and any deviation can be compensated using $EM1$ again.

References

[1] Michael Titze and Hebin Li. Interpretation of optical three-dimensional coherent spectroscopy. *Phys. Rev. A*, 96:032508, 2017.

[2] K. S. Novoselov, A. K. Geim, S. V. Morozov, D. Jiang, Y. Zhang, S. V. Dubonos, I. V. Grigorieva, and A. A. Firsov. Electric field effect in atomically thin carbon films. *Sci.*, 306:666, 2004.

[3] Andre Geim and Konstantin Novoselov. The nobel prize in physics, 2010.

[4] Kin Fai Mak, Changgu Lee, James Hone, Jie Shan, and Tony F. Heinz. Atomically Thin MoS_2: A New Direct-Gap Semiconductor. *Phys. Rev. Lett.*, 105:136805, 2010.

[5] K. Chiu, X. Zhang, X. Liu, V. M. Menon, Y. Chen, J. Wu, and Y. Lee. Synthesis and application of monolayer semiconductors (june 2015). *IEEE J. Quantum Electron.*, 51(10):1–10, 2015.

[6] A. Kumara and P. K. Ahluwalia. Electronic structure of transition metal dichalcogenides monolayers 1H-MX_2 (M = Mo, W; X = S, Se, Te) from ab-initio theory: new direct band gap semiconductors. *The Eur. Phys. J. B*, 85(186), 2012.

[7] Qinsheng Wang, Shaofeng Ge, Xiao Li, Jun Qiu, Yanxin Ji, Ji Feng, and Dong Sun. Valley carrier dynamics in monolayer molybdenum disulphide from helicity resolved ultrafast pump-probe spectroscopy. *ACS Nano*, 7(12):11087–11093, 2013.

[8] G. Kioseoglou, A. T. Hanbicki, M. Currie, A. L. Friedman, and B. T. Jonker. Optical polarization and intervalley scattering in single layers of MoS_2 and $MoSe_2$. *Sci. Reports*, 6, 2016.

[9] Philipp Steinleitner, Philipp Merkl, Philipp Nagler, Joshua Mornhinweg, Christian Schüller, Tobias Korn, Alexey Chernikov, and Rupert Huber. Direct Observation of Ultrafast Exciton Formation in a Monolayer of WSe_2. *Nano Lett.*, 17(3):1455–1460, 2017.

[10] Xiaodong Xu, Wang Yao, Di Xiao, and Tony F. Heinz. Spin and pseudospins in layered transition metal dichalcogenides. *Nat. Phys.*, 10(5):343–350, 2014.

[11] G. Kioseoglou, A. T. Hanbicki, M. Currie, A. L. Friedman, D. Gunlycke, and B. T. Jonker. Valley polarization and intervalley scattering in monolayer MoS_2. *Appl. Phys. Lett.*, 101, 2012.

[12] S. Dal Conte, F. Bottegoni, E. A. A. Pogna, D. De Fazio, S. Ambrogio, I. Bargigia, C. D'Andrea, A. Lombardo, M. Bruna, F. Ciccacci, A. C. Ferrari,

G. Cerullo, and M. Finazzi. Ultrafast valley relaxation dynamics in monolayer MoS_2 probed by nonequilibrium optical techniques. *Phys. Rev. B*, 92(23):1–6, 2015.

[13] Gang Wang, Cedric Robert, Aslihan Suslu, Bin Chen, Sijie Yang, Sarah Alamdari, Iann C Gerber, Thierry Amand, Xavier Marie, Sefaattin Tongay, and Bernhard Urbaszek. Spin-orbit engineering in transition metal dichalcogenide alloy monolayers. *Nat. Commun.*, 6:10110, 2015.

[14] Luyi Yang, Nikolai A. Sinitsyn, Weibing Chen, Jiangtan Yuan, Jing Zhang, Jun Lou, and Scott A. Crooker. Long-lived nanosecond spin relaxation and spin coherence of electrons in monolayer MoS_2 and WS_2. *Nat. Phys.*, 11:830–835, 2015.

[15] Kai Hao, Galan Moody, Fengcheng Wu, Chandriker Kavir Dass, Lixiang Xu, Chang-Hsiao Chen, Liuyang Sun, Ming-Yang Li, Lain-Jong Li, Allan H. MacDonald, and Xiaoqin Li. Direct measurement of exciton valley coherence in monolayer WSe_2. *Nat. Phys.*, 12(7):677–682, 2016.

[16] S. Dufferwiel, T. P. Lyons, D. D. Solnyshkov, A. A. P. Trichet, F. Withers, S. Schwarz, G. Malpuech, J. M. Smith, K. S. Novoselov, M. S. Skolnick, D. N. Krizhanovskii, and A. I. Tartakovskii. Valley addressable exciton-polaritons in atomically thin semiconductors. *Nat. Photonics*, 11:497–501, 2017.

[17] Tsuneya Ando. Screening effect and impurity scattering in monolayer graphene. *J. Phys. Soc. Jpn.*, 75:074716, 2006.

[18] S. Nunomura, D. Samsonov, and J. Goree. Transverse waves in a two-dimensional screened-coulomb crystal (dusty plasma). *Phys. Rev. Lett.*, 84:5141–5144, 2000.

[19] T. Zhang. *Optical Two-Dimensional Fourier Transform Spectroscopy of Semiconductors*. Ph.D. dissertation, University of Colorado Boulder, 2008.

[20] Bairen Zhu, Xi Chen, and Xiaodong Cui. Exciton Binding Energy of Monolayer WS_2. *Sci. Reports*, 5:9218, 2015.

[21] Akshay Singh, Galan Moody, Kha Tran, Marie E. Scott, Vincent Overbeck, Gunnar Berghäuser, John Schaibley, Edward J. Seifert, Dennis Pleskot, Nathaniel M. Gabor, Jiaqiang Yan, David G. Mandrus, Marten Richter, Ermin Malic, Xiaodong Xu, and Xiaoqin Li. Trion formation dynamics in monolayer transition metal dichalcogenides. *Phys. Rev. B*, 93:041401, 2016.

[22] Robert W. Boyd. *Nonlinear Optics*. Academic Press, 2008.

[23] Corey Janisch, Yuanxi Wang, Ding Ma, Nikhil Mehta, Ana Laura Elías, Néstor Perea-López, Mauricio Terrones, Vincent Crespi, and Zhiwen Liu. Extraordinary second harmonic generation in tungsten disulfide monolayers. *Sci. Reports*, 4, 2014.

[24] Michael C. Lucking, Kory Beach, and Humberto Terrones. Large second harmonic generation in alloyed tmds and boron nitride nanostructures. *Sci. Reports*, 8, 2018.

[25] Anton Autere, Henri Jussila, Andrea Marini, J. R. M. Saavedra, Yunyun Dai, Antti Säynätjoki, Lasse Karvonen, He Yang, Babak Amirsolaimani, Robert A. Norwood, Nasser Peyghambarian, Harri Lipsanen, Khanh Kieu, F. Javier García de Abajo, and Zhipei Sun. Optical harmonic generation in monolayer group-vi transition metal dichalcogenides. *Phys. Rev. B*, 98:115426, 2018.

[26] Lukas Mennel, Matthias Paur, and Thomas Mueller. Second harmonic generation in strained transition metal dichalcogenide monolayers: Mos2, mose2, ws2, and wse2. *APL Photonics*, 4(3):034404, 2019.

[27] Kai-Qiang Lin, Sebastian Bange, and John M. Lupton. Quantum interference in second-harmonic generation from monolayer wse2. *Nat. Phys.*, 2019.

[28] A. D. Bristow, D. Karaiskaj, X. Dai, T. Zhang, C. Carlsson, K. R. Hagen, R. Jimenez, and S. T. Cundiff. A versatile ultrastable platform for optical multidimensional fourier-transform spectroscopy. *Rev. Sci. Instruments*, 80(7), 2009.

[29] Gaël Nardin, Travis M. Autry, Kevin L. Silverman, and S. T. Cundiff. Multidimensional coherent photocurrent spectroscopy of a semiconductor nanostructure. *Opt. Express*, 21(23):28617–28627, 2013.

[30] Gaël Nardin, Travis M. Autry, Galan Moody, Rohan Singh, Hebin Li, and Steven T. Cundiff. Multi-dimensional coherent optical spectroscopy of semiconductor nanostructures: Collinear and non-collinear approaches. *J. Appl. Phys.*, 117(11):112804, 2015.

[31] Hebin Li and Steven T. Cundiff. Chapter One - 2D Coherent Spectroscopy of Electronic Transitions, 2017.

[32] Eric Martin. *Coherent Spectroscopy at the Diffraction Limit*. Ph.D. dissertation, University of Michigan, 2018.

[33] Richard R. Ernst, Geoffrey Bodenhausen, and Alexander Wokaun. *Principles of magnetic resonance in one and two dimensions*. Clarendon Press, 1987.

[34] Richard R. Ernst. Nobel Lecture - Nuclear Magnetic Resonance Fourier Transform Spectroscopy, 1992.

[35] H. M. Berman, J. Westbrook, Z. Feng, G. Gilliland, T. N. Bhat, H. Weissig, I. N. Shindyalov, and P. E. Bourne. The protein data bank, 2000.

[36] S. A. Huettel, A. W. Song, and G. McCarthy. *Functional Magnetic Resonance Imaging*. Number Bd. 1 in Functional Magnetic Resonance Imaging. Sinauer Associates, 2004.

[37] Yoshitaka Tanimura and Shaul Mukamel. Two-dimensional femtosecond vibrational spectroscopy of liquids. *The J. Chem. Phys.*, 99(12):9496–9511, 1993.

[38] John D. Hybl, Allison W. Albrecht, Sarah M. Gallagher Faeder, and David M. Jonas. Two-dimensional electronic spectroscopy. *Chem. Phys. Lett.*, 297(3):307 – 313, 1998.

[39] O. Golonzka, M. Khalil, N. Demirdöven, and A. Tokmakoff. Vibrational anharmonicities revealed by coherent two-dimensional infrared spectroscopy. *Phys. Rev. Lett.*, 86:2154–2157, 2001.

[40] Peifang Tian, Dorine Keusters, Yoshifumi Suzaki, and Warren S. Warren. Femtosecond phase-coherent two-dimensional spectroscopy. *Sci.*, 300(5625):1553–1555, 2003.

[41] T. Brixner, I. V. Stiopkin, and G. R. Fleming. Tunable two-dimensional femtosecond spectroscopy. *Opt. Lett.*, 29(8):884–886, 2004.

[42] M. L. Cowan, J. P. Ogilvie, and R. J. D. Miller. Two-dimensional spectroscopy using diffractive optics based phased-locked photon echoes. *Chem. Phys. Lett.*, 386(1):184 – 189, 2004.

[43] Camelia N. Borca, Tianhao Zhang, Xiaoqin Li, and Steven T. Cundiff. Optical two-dimensional fourier transform spectroscopy of semiconductors. *Chem. Phys. Lett.*, 416(4):311 – 315, 2005.

[44] Victor Volkov, Roland Schanz, and Peter Hamm. Active phase stabilization in fourier-transform two-dimensional infrared spectroscopy. *Opt. Lett.*, 30(15):2010–2012, 2005.

[45] Wolfgang Langbein and Brian Patton. Heterodyne spectral interferometry for multidimensional nonlinear spectroscopy of individual quantum systems. *Opt. Lett.*, 31(8):1151–1153, 2006.

[46] Tianhao Zhang, Camelia N. Borca, Xiaoqin Li, and S. T. Cundiff. Optical two-dimensional fourier transform spectroscopy with active interferometric stabilization. *Opt. Express*, 13(19):7432–7441, 2005.

[47] Ulrike Selig, Florian Langhojer, Frank Dimler, Tatjana Löhrig, Christoph Schwarz, Björn Gieseking, and Tobias Brixner. Inherently phase-stable coherent two-dimensional spectroscopy using only conventional optics. *Opt. Lett.*, 33(23):2851–2853, 2008.

[48] Wei Zhuang, Tomoyuki Hayashi, and Shaul Mukamel. Coherent multidimensional vibrational spectroscopy of biomolecules: concepts, simulations, and challenges. *Angewandte Chemie (International ed. English)*, 48(21):3750—3781, 2009.

[49] Feng Gao, Steven T. Cundiff, and Hebin Li. Probing dipole–dipole interaction in a rubidium gas via double-quantum 2d spectroscopy. *Opt. Lett.*, 41(13):2954–2957, 2016.

[50] Shaogang Yu, Michael Titze, Yifu Zhu, Xiaojun Liu, and Hebin Li. Observation of scalable and deterministic multi-atom dicke states in an atomic vapor. *arXiv*, 2018.

[51] Shaogang Yu, Michael Titze, Yifu Zhu, Xiaojun Liu, and Hebin Li. Long range dipole-dipole interaction in atomic vapors probed by double-quantum two-dimensional coherent spectroscopy. *arXiv*, 2018.

[52] Xiaoqin Li, Tianhao Zhang, Camelia N. Borca, and Steven T. Cundiff. Many-body interactions in semiconductors probed by optical two-dimensional fourier transform spectroscopy. *Phys. Rev. Lett.*, 96:057406, 2006.

[53] Steven T. Cundiff, Tianhao Zhang, Alan D. Bristow, Denis Karaiskaj, and Xingcan Dai. Optical two-dimensional fourier transform spectroscopy of semiconductor quantum wells. *Accounts Chem. Res.*, 42(9):1423–1432, 2009.

[54] Alan D. Bristow, Denis Karaiskaj, Xingcan Dai, Richard P. Mirin, and Steven T. Cundiff. Polarization dependence of semiconductor exciton and biexciton contributions to phase-resolved optical two-dimensional fourier-transform spectra. *Phys. Rev. B*, 79:161305, 2009.

[55] Khadga J. Karki, Julia R. Widom, Joachim Seibt, Ian Moody, Mark C. Lonergan, Tõnu Pullerits, and Andrew H. Marcus. Coherent two-dimensional photocurrent spectroscopy in a pbs quantum dot photocell. *Nat. Commun.*, 5:5869, 2014.

[56] Lijun Yang and Shaul Mukamel. Two-dimensional correlation spectroscopy of two-exciton resonances in semiconductor quantum wells. *Phys. Rev. Lett.*, 100:057402, 2008.

[57] M. Koch, J. Feldmann, G. von Plessen, E. O. Göbel, P. Thomas, and K. Köhler. Quantum beats versus polarization interference: An experimental distinction. *Phys. Rev. Lett.*, 69:3631–3634, 1992.

[58] V. G. Lyssenko, J. Erland, I. Balslev, K.-H. Pantke, B. S. Razbirin, and J. M. Hvam. Nature of nonlinear four-wave-mixing beats in semiconductors. *Phys. Rev. B*, 48:5720–5723, 1993.

[59] Hebin Li, Alan D. Bristow, Mark E. Siemens, Galan Moody, and Steven T. Cundiff. Unraveling quantum pathways using optical 3d fourier-transform spectroscopy. *Nat. Commun.*, 4:1390, 2013.

[60] Galan Moody, Chandriker Kavir Dass, Kai Hao, Chang-Hsiao Chen, Lain-Jong Li, Akshay Singh, Kha Tran, Genevieve Clark, Xiaodong Xu, Gunnar Berghäuser, Ermin Malic, Andreas Knorr, and Xiaoqin Li. Intrinsic homogeneous linewidth and broadening mechanisms of excitons in monolayer transition metal dichalcogenides. *Nat. Commun.*, 6:8315, 2015.

[61] Kai Hao, Lixiang Xu, Philipp Nagler, Akshay Singh, Kha Tran, Chandriker Kavir Dass, Christian Schüller, Tobias Korn, Xiaoqin Li, and Galan Moody. Coherent and Incoherent Coupling Dynamics between Neutral and Charged Excitons in Monolayer MoSe2. *Nano Lett.*, 16(8):5109–5113, 2016.

[62] Kai Hao, Judith F. Specht, Philipp Nagler, Lixiang Xu, Kha Tran, Akshay Singh, Chandriker Kavir Dass, Christian Schüller, Tobias Korn, Marten Richter, Andreas Knorr, Xiaoqin Li, and Galan Moody. Neutral and charged inter-valley biexcitons in monolayer $MoSe_2$. *Nat. Commun.*, 8:15552, 2017.

[63] C.E. Stevens, P. Dey, J. Paul, Z. Wang, H. Zhang, A.H. Romero, J. Shan, D.J. Hilton, and D. Karaiskaj. The role of electron-phonon interactions on the coherence lifetime of monolayer transition metal dichalcogenides. *Solid State Communications*, 266(Supplement C):30 – 33, 2017.

[64] Eric W. Martin, Jason Horng, Hanna G. Ruth, Eunice Paik, Michael-Henr Wentzel, Hui Deng, and Steven T. Cundiff. Encapsulation Narrows Excitonic Homogeneous Linewidth of Exfoliated $MoSe_2$ Monolayer. *arXiv*, 2018.

[65] Richard P. Feynman. Plenty of room at the bottom, 1959.

[66] Anderson P. W. More is different. *Sci.*, 177:393–396, 1972.

[67] Landau L. D. and Lifshitz E. M. Course of theoretical physics 3, 1986.

[68] Jesús Carrete, Wu Li, Lucas Lindsay, David A. Broido, Luis J. Gallego, and Natalio Mingo. Physically founded phonon dispersions of few-layer materials and the case of borophene. *Mater. Res. Lett.*, 4(4):204–211, 2016.

[69] V. I. Anisimov and O. Gunnarsson. Density-functional calculation of effective coulomb interactions in metals. *Phys. Rev. B*, 43:7570–7574, 1991.

[70] F. W. Van Keuls, X. L. Hu, H. W. Jiang, and A. J. Dahm. Screening of the coulomb interaction in two-dimensional variable-range hopping. *Phys. Rev. B*, 56:1161–1169, 1997.

[71] T. O. Wehling, E. Şaşıoğlu, C. Friedrich, A. I. Lichtenstein, M. I. Katsnelson, and S. Blügel. Strength of effective coulomb interactions in graphene and graphite. *Phys. Rev. Lett.*, 106:236805, 2011.

[72] Timothy C. Berkelbach, Mark S. Hybertsen, and David R. Reichman. Theory of neutral and charged excitons in monolayer transition metal dichalcogenides. *Phys. Rev. B*, 88:045318, 2013.

[73] Kin Fai Mak and Jie Shan. Photonics and optoelectronics of 2D semiconductor transition metal dichalcogenides. *Nat. Photonics*, 10:216–226, 2016.

[74] Diana Y. Qiu, Felipe H. da Jornada, and Steven G. Louie. Optical spectrum of mos_2: Many-body effects and diversity of exciton states. *Phys. Rev. Lett.*, 111:216805, 2013.

[75] Gunnar Berghäuser and Ermin Malic. Analytical approach to excitonic properties of mos_2. *Phys. Rev. B*, 89:125309, 2014.

[76] Miguel M. Ugeda, Aaron J. Bradley, Su-Fei Shi, Felipe H. da Jornada, Yi Zhang, Diana Y. Qiu, Wei Ruan, Sung-Kwan Mo, Zahid Hussain, Zhi-Xun Shen, Feng Wang, Steven G. Louie, and Michael F. Crommie. Giant bandgap renormalization and excitonic effects in a monolayer transition metal dichalcogenide semiconductor. *Nat. Mater.*, 13:1091–1095, 2014.

[77] Sangeeth Kallatt, Govindarao Umesh, and Kausik Majumdar. Valley-coherent hot carriers and thermal relaxation in monolayer transition metal dichalcogenides. *The J. Phys. Chem. Lett.*, 7(11):2032–2038, 2016.

[78] A. T. Hanbicki, M. Currie, G. Kioseoglou, A. L. Friedman, and B. T. Jonker. Measurement of high exciton binding energy in the monolayer transition-metal dichalcogenides WS_2 and WSe_2. *Solid State Commun.*, 203:16 – 20, 2015.

[79] Ilkka Kylänpää and Hannu-Pekka Komsa. Binding energies of exciton complexes in transition metal dichalcogenide monolayers and effect of dielectric environment. *Phys. Rev. B*, 92:205418, 2015.

[80] Kin Fai Mak, Keliang He, Changgu Lee, Gwan Hyoung Lee, James Hone, Tony F. Heinz, and Jie Shan. Tightly bound trions in monolayer MoS_2. *Nat. Mater.*, 12:207–211, 2013.

[81] Keliang He, Nardeep Kumar, Liang Zhao, Zefang Wang, Kin Fai Mak, Hui Zhao, and Jie Shan. Tightly Bound Excitons in Monolayer WSe_2. *Phys. Rev. Lett.*, 113:026803, 2014.

[82] Jason W. Christopher, Bennett B. Goldberg, and Anna K. Swan. Long tailed trions in monolayer MoS_2: Temperature dependent asymmetry and resulting red-shift of trion photoluminescence spectra. *Sci. Reports*, 7, 2017.

[83] F. Gao, Y. Gong, M. Titze, R. Almeida, P. M. Ajayan, and H. Li. Valley Trion Dynamics in Monolayer $MoSe_2$. *Phys. Rev. B*, 94:245413, 2016.

[84] C. Kittel. *Introduction to Solid State Physics*. Wiley, 1996.

[85] S. Reich, J. Maultzsch, C. Thomsen, and P. Ordejón. Tight-binding description of graphene. *Phys. Rev. B*, 66:035412, 2002.

[86] A. Grüneis, C. Attaccalite, L. Wirtz, H. Shiozawa, R. Saito, T. Pichler, and A. Rubio. Tight-binding description of the quasiparticle dispersion of graphite and few-layer graphene. *Phys. Rev. B*, 78:205425, 2008.

[87] E. Cappelluti, R. Roldán, J. A. Silva-Guillén, P. Ordejón, and F. Guinea. Tight-binding model and direct-gap/indirect-gap transition in single-layer and multilayer MoS_2. *Phys. Rev. B*, 88:075409, 2013.

[88] Gui-Bin Liu, Wen-Yu Shan, Yugui Yao, Wang Yao, and Di Xiao. Three-band tight-binding model for monolayers of group-VIB transition metal dichalcogenides. *Phys. Rev. B*, 88:085433, 2013.

[89] Ferdows Zahid, Lei Liu, Yu Zhu, Jian Wang, and Hong Guo. A generic tight-binding model for monolayer, bilayer and bulk MoS_2. *AIP Adv.*, 3(5):052111, 2013.

[90] S. K. Mahatha, K. D. Patel, and K. S. R. Menon. Electronic structure investigation of mos2 and mose2 using angle-resolved photoemission spectroscopy and ab initio band structure studies. *J. Physics: Condens. Matter*, 24(47), 2012.

[91] Alexey Chernikov, Timothy C. Berkelbach, Heather M. Hill, Albert Rigosi, Yilei Li, Ozgur Burak Aslan, David R. Reichman, Mark S. Hybertsen, and Tony F. Heinz. Exciton Binding Energy and Nonhydrogenic Rydberg Series in Monolayer WS_2. *Phys. Rev. Lett.*, 113:076802, 2014.

[92] Heather M. Hill, Albert F. Rigosi, Cyrielle Roquelet, Alexey Chernikov, Timothy C. Berkelbach, David R. Reichman, Mark S. Hybertsen, Louis E. Brus, and Tony F. Heinz. Observation of Excitonic Rydberg States in Monolayer MoS_2 and WS_2 by Photoluminescence Excitation Spectroscopy. *Nano Lett.*, 15:2992–2997, 2015.

[93] G. Wang, E. Palleau, T. Amand, S. Tongay, X. Marie, and B. Urbaszek. Polarization and time-resolved photoluminescence spectroscopy of excitons in $MoSe_2$ monolayers. *Appl. Phys. Lett.*, 106(11):112101, 2015.

[94] E. Courtade, M. Semina, M. Manca, M. M. Glazov, C. Robert, F. Cadiz, G. Wang, T. Taniguchi, K. Watanabe, M. Pierre, W. Escoffier, E. L. Ivchenko, P. Renucci, X. Marie, T. Amand, and B. Urbaszek. Charged excitons in monolayer WSe_2: Experiment and theory. *Phys. Rev. B*, 96:085302, 2017.

[95] Jun Xiao, Mervin Zhao, Yuan Wang, and Xiang Zhang. Excitons in atomically thin 2D semiconductors and their applications. *Nanophotonics*, 6:1309–1328, 2017.

[96] Z. Li, T. Wang, Z. Lu, C. Jin, Y. Chen, Y. Meng, Z. Lian, T. Taniguchi, K. Watanabe, S. Zhang, D. Smirnov, and S. F. Shi. Revealing the biexciton and trion-exciton complexes in BN encapsulated WSe_2. *Nat. communications*, 9, 2018.

[97] Galan Moody, John Schaibley, and Xiaodong Xu. Exciton dynamics in monolayer transition metal dichalcogenides [invited]. *J. Opt. Soc. Am. B*, 33(7):C39–C49, 2016.

[98] C. Poellmann, P. Steinleitner, U. Leierseder, P. Nagler, G. Plechinger, M. Porer, R. Bratschitsch, C. Schüller, T. Korn, and R. Huber. Resonant internal quantum transitions and femtosecond radiative decay of excitons in monolayer wse2. *Nat. Mater.*, 14:889–893, 2015.

[99] Xiao-Xiao Zhang Yumeng You, Timothy C. Berkelbach, Mark S. Hybertsen, David R. Reichman, and Tony F. Heinz. Observation of biexcitons in monolayer wse2. *Nat. Phys.*, 11:477–481, 2015.

[100] Huimin Su, Aiying Deng, Zhiheng Zhen, and Jun-Feng Dai. Γ-valley assisted intervalley scattering in monolayer and bilayer Ws_2 revealed by time-resolved kerr rotation spectroscopy. *Phys. Rev. B*, 97:115426, 2018.

[101] A. A. Mitioglu, L. Klopotowski, D. K. Maude, G. Deligeorgis, S. Anghel, L. Kulyuk, and P. Plochocka. Intervalley scattering of excitons and trions in monolayer wse2 under strong excitation. *arXiv*, 2015.

[102] Zilong Wang, Alejandro Molina-Sánchez, Patrick Altmann, Davide Sangalli, Domenico De Fazio, Giancarlo Soavi, Ugo Sassi, Federico Bottegoni, Franco Ciccacci, Marco Finazzi, Ludger Wirtz, Andrea C. Ferrari, Andrea Marini, Giulio Cerullo, and Stefano Dal Conte. Intravalley spin–flip relaxation dynamics in single-layer ws2. *Nano Lett.*, 18(11):6882–6891, 2018.

[103] Dezheng Sun, Yi Rao, Georg A. Reider, Gugang Chen, Yumeng You, Louis Brézin, Avetik R. Harutyunyan, and Tony F. Heinz. Observation of rapid exciton–exciton annihilation in monolayer molybdenum disulfide. *Nano Lett.*, 14(10):5625–5629, 2014.

[104] Yiling Yu, Yifei Yu, Chao Xu, Andy Barrette, Kenan Gundogdu, and Linyou Cao. Fundamental limits of exciton-exciton annihilation for light emission in transition metal dichalcogenide monolayers. *Phys. Rev. B*, 93:201111, 2016.

[105] Mark Danovich, Viktor Zólyomi, Vladimir I. Fal'ko, and Igor L. Aleiner. Auger recombination of dark excitons in WS_2 and WSe_2 monolayers. *2D Mater.*, 3(3):035011, 2016.

[106] Haining Wang, Changjian Zhang, and Farhan Rana. Ultrafast dynamics of defect-assisted electron–hole recombination in monolayer mos2. *Nano Lett.*, 15(1):339–345, 2015.

[107] Aaron M. Jones, Hongyi Yu, John R. Schaibley, Jiaqiang Yan, David G. Mandrus, Takashi Taniguchi, Kenji Watanabe, Hanan Dery, Wang Yao, and Xiaodong Xu. Excitonic luminescence upconversion in a two-dimensional semiconductor. *Nat. Phys.*, 12:323–327, 2016.

[108] C. A. Sackett, D. Kielpinski, B. E. King, C. Langer, V. Meyer, C. J. Myatt, M. Rowe, Q. A. Turchette, W. M. Itano, D. J. Wineland, and C. Monroe. Experimental entanglement of four particles. *Nat.*, 404:256–259, 2000.

[109] H. Häffner, W. Hänsel, C. F. Roos, J. Benhelm, D. Chek al kar, M. Chwalla, T. Körber, U. D. Rapol, M. Riebe, P. O. Schmidt, C. Becher, O. Gühne, W. Dür, and R. Blatt. Scalable multiparticle entanglement of trapped ions. *Nat.*, 438:643–646, 2005.

[110] Thomas Monz, Philipp Schindler, Julio T. Barreiro, Michael Chwalla, Daniel Nigg, William A. Coish, Maximilian Harlander, Wolfgang Hänsel, Markus Hennrich, and Rainer Blatt. 14-qubit entanglement: Creation and coherence. *Phys. Rev. Lett.*, 106:130506, 2011.

[111] N. Kiesel, C. Schmid, G. Tóth, E. Solano, and H. Weinfurter. Experimental observation of four-photon entangled dicke state with high fidelity. *Phys. Rev. Lett.*, 98:063604, 2007.

[112] Witlef Wieczorek, Christian Schmid, Nikolai Kiesel, Reinhold Pohlner, Otfried Gühne, and Harald Weinfurter. Experimental observation of an entire family of four-photon entangled states. *Phys. Rev. Lett.*, 101:010503, 2008.

[113] R. Prevedel, G. Cronenberg, M. S. Tame, M. Paternostro, P. Walther, M. S. Kim, and A. Zeilinger. Experimental realization of dicke states of up to six qubits for multiparty quantum networking. *Phys. Rev. Lett.*, 103:020503, 2009.

[114] Witlef Wieczorek, Roland Krischek, Nikolai Kiesel, Patrick Michelberger, Géza Tóth, and Harald Weinfurter. Experimental entanglement of a six-photon symmetric dicke state. *Phys. Rev. Lett.*, 103:020504, 2009.

[115] Xing-Can Yao, Tian-Xiong Wang, Ping Xu, He Lu, Ge-Sheng Pan, Xiao-Hui Bao, Cheng-Zhi Peng, Chao-Yang Lu, Yu-Ao Chen, and Jian-Wei Pan. Observation of eight-photon entanglement. *Nat. Photonics*, 6:225–228, 2012.

[116] Xi-Lin Wang, Luo-Kan Chen, W. Li, H.-L. Huang, C. Liu, C. Chen, Y.-H. Luo, Z.-E. Su, D. Wu, Z.-D. Li, H. Lu, Y. Hu, X. Jiang, C.-Z. Peng, L. Li, N.-L. Liu, Yu-Ao Chen, Chao-Yang Lu, and Jian-Wei Pan. Experimental ten-photon entanglement. *Phys. Rev. Lett.*, 117:210502, 2016.

[117] R. Barends, J. Kelly, A. Megrant, A. Veitia, D. Sank, E. Jeffrey, T. C. White, J. Mutus, A. G. Fowler, B. Campbell, Y. Chen, Z. Chen, B. Chiaro, A. Dunsworth, C. Neill, P. O'Malley, P. Roushan, A. Vainsencher, J. Wenner, A. N. Korotkov, A. N. Cleland, and John M. Martinis. Superconducting quantum circuits at the surface code threshold for fault tolerance. *Nat.*, 508:500–503, 2014.

[118] Chao Song, Kai Xu, Wuxin Liu, Chui-ping Yang, Shi-Biao Zheng, Hui Deng, Qiwei Xie, Keqiang Huang, Qiujiang Guo, Libo Zhang, Pengfei Zhang, Da Xu, Dongning Zheng, Xiaobo Zhu, H. Wang, Y.-A. Chen, C.-Y. Lu, Siyuan Han, and Jian-Wei Pan. 10-qubit entanglement and parallel logic operations with a superconducting circuit. *Phys. Rev. Lett.*, 119:180511, 2017.

[119] Jagdeep Shah. *Ultrafast Spectroscopy of Semiconductors and Semiconductor Nanostructures*. Springer Series in Solid-State Sciences. Springer-Verlag Berlin Heidelberg, 1996.

[120] Jeongho Kim, Shaul Mukamel, and Gregory D. Scholes. Two-dimensional electronic double-quantum coherence spectroscopy. *Accounts Chem. Res.*, 42(9):1375–1384, 2009.

[121] Alexandra Nemeth, Franz Milota, Tomáš Mančal, Tönu Pullerits, Jaroslaw Sperling, Jürgen Hauer, Harald F. Kauffmann, and Niklas Christensson. Double-quantum two-dimensional electronic spectroscopy of a three-level system: Experiments and simulations. *The J. Chem. Phys.*, 133(9):094505, 2010.

[122] Xingcan Dai, Marten Richter, Hebin Li, Alan D. Bristow, Cyril Falvo, Shaul Mukamel, and Steven T. Cundiff. Two-dimensional double-quantum spectra reveal collective resonances in an atomic vapor. *Phys. Rev. Lett.*, 108:193201, 2012.

[123] Bachana Lomsadze and Steven T. Cundiff. Frequency-comb based double-quantum two-dimensional spectrum identifies collective hyperfine resonances in atomic vapor induced by dipole-dipole interactions. *Phys. Rev. Lett.*, 120:233401, 2018.

[124] Tatsuo Yajima and Yoichi Taira. Spatial optical parametric coupling of picosecond light pulses and transverse relaxation effect in resonant media. *J. Phys. Soc. Jpn.*, 47(5):1620–1626, 1979.

[125] Mark E. Siemens, Galan Moody, Hebin Li, Alan D. Bristow, and Steven T. Cundiff. Resonance lineshapes in two-dimensional fourier transform spectroscopy. *Opt. Express*, 18(17):17699–17708, 2010.

[126] V. O. Lorenz, X. Dai, H. Green, T. R. Asnicar, and S. T. Cundiff. High-density, high-temperature alkali vapor cell. *Rev. Sci. Instruments*, 79(12):123104, 2008.

[127] G. Moody, R. Singh, H. Li, I. A. Akimov, M. Bayer, D. Reuter, A. D. Wieck, A. S. Bracker, D. Gammon, and S. T. Cundiff. Influence of confinement on biexciton binding in semiconductor quantum dot ensembles measured with two-dimensional spectroscopy. *Phys. Rev. B*, 87:041304, 2013.

[128] T. M. Autry, G. Moody, C. McDonald, J. M. Fraser, R. P. Mirin, and K. L. Silverman. Vibrational interferometry enables single-scan acquisition of all $\chi(3)$ multi-dimensional coherent spectral maps. In *Conference on Lasers and Electro-Optics*, page FF3D.3. Optical Society of America, 2018.

[129] Haiyan Nan, Zilu Wang, Wenhui Wang, Zheng Liang, Yan Lu, Qian Chen, Daowei He, Pingheng Tan, Feng Miao, Xinran Wang, Jinlan Wang, and Zhenhua Ni. Strong photoluminescence enhancement of mos2 through defect engineering and oxygen bonding. *ACS Nano*, 8(6):5738–5745, 2014.

[130] Murray A. Lampert. Mobile and immobile effective-mass-particle complexes in nonmetallic solids. *Phys. Rev. Lett.*, 1:450–453, 1958.

[131] K. Kheng, R. T. Cox, Merle Y. d' Aubigné, Franck Bassani, K. Saminadayar, and S. Tatarenko. Observation of negatively charged excitons x^- in semiconductor quantum wells. *Phys. Rev. Lett.*, 71:1752–1755, 1993.

[132] M. T. Portella-Oberli, J. Berney, L. Kappei, F. Morier-Genoud, J. Szczytko, and B. Deveaud-Plédran. Dynamics of trion formation in $\mathrm{in}_x\mathrm{ga}_{1-x}\mathrm{As}$ quantum wells. *Phys. Rev. Lett.*, 102:096402, 2009.

[133] Jason S. Ross, Sanfeng Wu, Hongyi Yu, Nirmal J. Ghimire, Aaron M. Jones, Grant Aivazian, Jiaqiang Yan, David G. Mandrus, Di Xiao, Wang Yao, and Xiaodong Xu. Electrical control of neutral and charged excitons in a monolayer semiconductor. *Nat. Commun.*, 4:1474, 2013.

[134] A. Thilagam. Two-dimensional charged-exciton complexes. *Phys. Rev. B*, 55:7804–7808, 1997.

[135] Aaron M. Jones, Hongyi Yu, Nirmal J. Ghimire, Sanfeng Wu, Grant Aivazian, Jason S. Ross, Bo Zhao, Jiaqiang Yan, David G. Mandrus, Di Xiao, Wang Yao,

and Xiaodong Xu. Optical generation of excitonic valley coherence in monolayer wse2. *Nat. Nanotechnol.*, 8:634–638, 2013.

[136] Tawinan Cheiwchanchamnangij and Walter R. L. Lambrecht. Quasiparticle band structure calculation of monolayer, bilayer, and bulk mos_2. *Phys. Rev. B*, 85:205302, 2012.

[137] J. Jadczak, A. Delgado, L. Bryja, Y. S. Huang, and P. Hawrylak. Robust high-temperature trion emission in monolayers of $Mo(S_ySe_{1-y})_2$ alloys. *Phys. Rev. B*, 95:195427, 2017.

[138] C. H. Lui, A. J. Frenzel, D. V. Pilon, Y.-H. Lee, X. Ling, G. M. Akselrod, J. Kong, and N. Gedik. Trion-induced negative photoconductivity in monolayer mos_2. *Phys. Rev. Lett.*, 113:166801, 2014.

[139] Akshay Singh, Galan Moody, Sanfeng Wu, Yanwen Wu, Nirmal J. Ghimire, Jiaqiang Yan, David G. Mandrus, Xiaodong Xu, and Xiaoqin Li. Coherent electronic coupling in atomically thin $mose_2$. *Phys. Rev. Lett.*, 112:216804, 2014.

[140] Xiaodong Xu, Bo Sun, Paul R. Berman, Duncan G. Steel, Allan S. Bracker, Dan Gammon, and L. J. Sham. Coherent population trapping of an electron spin in a single negatively charged quantum dot. *Nat. Phys.*, 4:692–695, 2008.

[141] T. Korn, S. Heydrich, M. Hirmer, J. Schmutzler, and C. Schüller. Low-temperature photocarrier dynamics in monolayer mos2. *Appl. Phys. Lett.*, 99(10), 2011.

[142] D. Lagarde, L. Bouet, X. Marie, C. R. Zhu, B. L. Liu, T. Amand, P. H. Tan, and B. Urbaszek. Carrier and Polarization Dynamics in Monolayer MoS_2. *Phys. Rev. Lett.*, 112:047401, 2014.

[143] Hongyan Shi, Rusen Yan, Simone Bertolazzi, Jacopo Brivio, Bo Gao, Andras Kis, Debdeep Jena, Huili Grace Xing, and Libai Huang. Exciton dynamics in suspended monolayer and few-layer mos2 2d crystals. *ACS Nano*, 7(2):1072–1080, 2013.

[144] Qiannan Cui, Frank Ceballos, Nardeep Kumar, and Hui Zhao. Transient absorption microscopy of monolayer and bulk wse2. *ACS Nano*, 8(3):2970–2976, 2014.

[145] Nardeep Kumar, Qiannan Cui, Frank Ceballos, Dawei He, Yongsheng Wang, and Hui Zhao. Exciton-exciton annihilation in $mose_2$ monolayers. *Phys. Rev. B*, 89:125427, 2014.

[146] Cong Mai, Andrew Barrette, Yifei Yu, Yuriy G. Semenov, Ki Wook Kim, Linyou Cao, and Kenan Gundogdu. Many-body effects in valleytronics: Direct measurement of valley lifetimes in single-layer mos2. *Nano Lett.*, 14(1):202–206, 2014.

[147] Cong Mai, Yuriy G. Semenov, Andrew Barrette, Yifei Yu, Zhenghe Jin, Linyou Cao, Ki Wook Kim, and Kenan Gundogdu. Exciton valley relaxation in a single layer of ws_2 measured by ultrafast spectroscopy. *Phys. Rev. B*, 90:041414, 2014.

[148] Ehren M. Mannebach, Karel-Alexander N. Duerloo, Lenson A. Pellouchoud, Meng-Ju Sher, Sanghee Nah, Yi-Hong Kuo, Yifei Yu, Ann F. Marshall, Linyou Cao, Evan J. Reed, and Aaron M. Lindenberg. Ultrafast electronic and structural response of monolayer mos2 under intense photoexcitation conditions. *ACS Nano*, 8(10):10734–10742, 2014.

[149] G. Wang, X. Marie, I. Gerber, T. Amand, D. Lagarde, L. Bouet, M. Vidal, A. Balocchi, and B. Urbaszek. Giant enhancement of the optical second-harmonic emission of wse_2 monolayers by laser excitation at exciton resonances. *Phys. Rev. Lett.*, 114:097403, 2015.

[150] Xiao-Xiao Zhang, Yumeng You, Shu Yang Frank Zhao, and Tony F. Heinz. Experimental evidence for dark excitons in monolayer wse_2. *Phys. Rev. Lett.*, 115:257403, 2015.

[151] Luyi Yang, Weibing Chen, Kathleen M. McCreary, Berend T. Jonker, Jun Lou, and Scott A. Crooker. Spin coherence and dephasing of localized electrons in monolayer mos2. *Nano Lett.*, 15(12):8250–8254, 2015.

[152] Tomasz Jakubczyk, Valentin Delmonte, Maciej Koperski, Karol Nogajewski, Clément Faugeras, Wolfgang Langbein, Marek Potemski, and Jacek Kasprzak. Radiatively limited dephasing and exciton dynamics in mose2 monolayers revealed with four-wave mixing microscopy. *Nano Lett.*, 16(9):5333–5339, 2016.

[153] Michael Titze, Bo Li, Xiang Zhang, Pulickel M. Ajayan, and Hebin Li. Intrinsic coherence time of trions in monolayer $mose_2$ measured via two-dimensional coherent spectroscopy. *Phys. Rev. Mater.*, 2:054001, 2018.

[154] John R. Schaibley, Todd Karin, Hongyi Yu, Jason S. Ross, Pasqual Rivera, Aaron M. Jones, Marie E. Scott, Jiaqiang Yan, D. G. Mandrus, Wang Yao, Kai-Mei Fu, and Xiaodong Xu. Population pulsation resonances of excitons in monolayer $mose_2$ with sub-1 μeV linewidths. *Phys. Rev. Lett.*, 114:137402, 2015.

[155] G. Wang, L. Bouet, D. Lagarde, M. Vidal, A. Balocchi, T. Amand, X. Marie, and B. Urbaszek. Valley dynamics probed through charged and neutral exciton emission in monolayer wse_2. *Phys. Rev. B*, 90:075413, 2014.

[156] Xingli Wang, Yongji Gong, Gang Shi, Wai Leong Chow, Kunttal Keyshar, Gonglan Ye, Robert Vajtai, Jun Lou, Zheng Liu, Emilie Ringe, Beng Kang Tay, and Pulickel M. Ajayan. Chemical vapor deposition growth of crystalline monolayer $MoSe_2$. *ACS Nano*, 8(5):5125–5131, 2014.

[157] Xiaotian Zhang, Tanushree H. Choudhury, Mikhail Chubarov, Yu Xiang, Bhakti Jariwala, Fu Zhang, Nasim Alem, Gwo-Ching Wang, Joshua A. Robinson, and Joan M. Redwing. Diffusion-controlled epitaxy of large area coalesced wse2 monolayers on sapphire. *Nano Lett.*, 18(2):1049–1056, 2018.

[158] Yu-Chuan Lin, Bhakti Jariwala, Brian M. Bersch, Ke Xu, Yifan Nie, Baoming Wang, Sarah M. Eichfeld, Xiaotian Zhang, Tanushree H. Choudhury, Yi Pan, Rafik Addou, Christopher M. Smyth, Jun Li, Kehao Zhang, M. Aman Haque, Stefan Fölsch, Randall M. Feenstra, Robert M. Wallace, Kyeongjae Cho, Susan K. Fullerton-Shirey, Joan M. Redwing, and Joshua A. Robinson. Realizing large-scale, electronic-grade two-dimensional semiconductors. *ACS Nano*, 12(2):965–975, 2018.

[159] Saurav Islam, Semonti Bhattacharyya, Abhinav Kandala, Anthony Richardella, Nitin Samarth, and Arindam Ghosh. Bulk-impurity induced noise in large-area epitaxial thin films of topological insulators. *Appl. Phys. Lett.*, 111(6):062107, 2017.

[160] Humberto R. Gutiérrez, Nestor Perea-López, Ana Laura Elías, Ayse Berkdemir, Bei Wang, Ruitao Lv, Florentino López-Urías, Vincent H. Crespi, Humberto Terrones, and Mauricio Terrones. Extraordinary Room-Temperature Photoluminescence in Triangular WS_2 Monolayers. *Nano Lett.*, 13(8):3447–3454, 2013.

[161] Hebin Li, Austin P. Spencer, Andrew Kortyna, Galan Moody, David M. Jonas, and Steven T. Cundiff. Pulse Propagation Effects in Optical 2D Fourier-Transform Spectroscopy: Experiment. *The J. Phys. Chem. A*, 117(29):6279–6287, 2013.

[162] Austin P. Spencer, Hebin Li, Steven T. Cundiff, and David M. Jonas. Pulse Propagation Effects in Optical 2D Fourier-Transform Spectroscopy: Theory. *The J. Phys. Chem. A*, 119(17):3936–3960, 2015.

[163] Ermin Malic, Malte Selig, Maja Feierabend, Samuel Brem, Dominik Christiansen, Florian Wendler, Andreas Knorr, and Gunnar Berghäuser. Dark excitons in transition metal dichalcogenides. *Phys. Rev. Mater.*, 2:014002, 2018.

[164] Nicholas A. Lanzillo, A. Glen Birdwell, Matin Amani, Frank J. Crowne, Pankaj B. Shah, Sina Najmaei, Zheng Liu, Pulickel M. Ajayan, Jun Lou, Madan Dubey, Saroj K. Nayak, and Terrance P. O'Regan. Temperature-dependent phonon shifts in monolayer mos2. *Appl. Phys. Lett.*, 103(9):093102, 2013.

[165] Yaowu Hu, Feng Zhang, Michael Titze, Biwei Deng, Hebin Li, and Gary J. Cheng. Straining effects in mos2 monolayer on nanostructured substrates: temperature-dependent photoluminescence and exciton dynamics. *Nanoscale*, 10:5717–5724, 2018.

[166] D. Edelberg, D. Rhodes, A. Kerelsky, B. Kim, J. Wang, A. Zangiabadi, C. Kim, A. Abhinandan, J. Ardelean, M. Scully, D. Scullion, L. Embon, I. Zhang, R. Zu, Elton J. G. Santos, L. Balicas, C. Marianetti, K. Barmak, X.-Y. Zhu, J. Hone, and A. N. Pasupathy. Hundredfold enhancement of light emission via defect control in monolayer transition-metal dichalcogenides. *arXiv*, 2018.

[167] Nihit Saigal and Sandip Ghosh. Phonon induced luminescence decay in monolayer mos2 on sio2/si substrates. *Appl. Phys. Lett.*, 107(24):242103, 2015.

[168] Malte Selig, Gunnar Berghäuser, Archana Raja, Philipp Nagler, Christian Schüller, Tony F. Heinz, Tobias Korn, Alexey Chernikov, Ermin Malic, and Andreas Knorr. Excitonic linewidth and coherence lifetime in monolayer transition metal dichalcogenides. *Nat. Commun.*, 7:13279, 2016.

[169] Jiani Huang, Thang B. Hoang, and Maiken H. Mikkelsen. Probing the origin of excitonic states in monolayer wse2. *Sci. Reports*, 6:22414, 2016.

[170] Christopher L. Smallwood, Travis M. Autry, and Steven T. Cundiff. Analytical solutions to the finite-pulse bloch model for multidimensional coherent spectroscopy. *J. Opt. Soc. Am. B*, 34(2):419–429, 2017.

[171] Václav Perlík, Jürgen Hauer, and František Šanda. Finite pulse effects in single and double quantum spectroscopies. *J. Opt. Soc. Am. B*, 34(2):430–439, 2017.

[172] Eric Jones, Travis Oliphant, Pearu Peterson, et al. SciPy: Open source scientific tools for Python, 2001–. [Online; accessed 08/01/2018].

[173] Jonathan C. Shaw, Hailong Zhou, Yu Chen, Nathan O. Weiss, Yuan Liu, Yu Huang, and Xiangfeng Duan. Chemical vapor deposition growth of monolayer $MoSe_2$ nanosheets. *Nano Res.*, 7(4):511–517, 2014.

[174] C. R. Dean, A. F. Young, I. Meric, C. Lee, L. Wang, S. Sorgenfrei, K. Watanabe, T. Taniguchi, P. Kim, K. L. Shepard, and J. Hone. Boron nitride substrates for high-quality graphene electronics. *Nat. Nanotechnol.*, 5:722 – 726, 2010.

[175] Xu Cui, Gwan-Hyoung Lee, Young Duck Kim, Ghidewon Arefe, Pinshane Y. Huang, Chul-Ho Lee, Daniel A. Chenet, Xian Zhang, Lei Wang, Fan Ye, Filippo Pizzocchero, Bjarke S. Jessen, Kenji Watanabe, Takashi Taniguchi, David A. Muller, Tony Low, Philip Kim, and James Hone. Multi-terminal transport measurements of mos2 using a van der waals heterostructure device platform. *Nat. Nanotechnol.*, 10:534 – 540, 2015.

[176] Seongjoon Ahn, Gwangwoo Kim, Pramoda K. Nayak, Seong In Yoon, Hyunseob Lim, Hyun-Joon Shin, and Hyeon Suk Shin. Prevention of transition metal dichalcogenide photodegradation by encapsulation with h-bn layers. *ACS Nano*, 10(9):8973–8979, 2016.

VITA

MICHAEL TITZE

2010 - 2013	B.Sc., Physics Heinrich Heine Universität Düsseldorf Düsseldorf, Germany
2013 - 2016	M.Sc., Physics Florida International University Miami, Florida
2017 - 2019	Doctoral Candidate Florida International University Miami, Florida
2018	Dissertation Year Fellowship Florida International University

Publications and Conference Presentations

1. M. Titze, C. Fei, M. Munoz, H. Wang and H. Li, "Carrier Dynamics Between the Ordered and Disordered Orthorhombic Lattice Domains in Methylammonium Lead Iodide Perovskite revealed by Two-Dimensional Coherent Spectroscopy", (manuscript in preparation)

2. S. Yu, M. Titze, Y. Zhu, X. Liu, and H. Li, "Long range dipole-dipole interaction in atomic vapors probed by double-quantum two-dimensional coherent spectroscopy", arXiv:1811.07963 (submitted)

3. S. Yu, M. Titze, Y. Zhu, X. Liu, and H. Li, "Observation of scalable and deterministic multi-atom Dicke states in an atomic vapor", arXiv:1807.09300, (submitted)

4. M. Titze, B. Li ,X. Zhang, P. M. Ajayan and H. Li, "Intrinsic coherence time of trions in monolayer $MoSe_2$ measured via two-dimensional coherent spectroscopy", Phys. Rev. Materials, 2, 054001 (2018)

5. Y. Hu, F. Zhang, M. Titze, B. Deng, H. Li and G. J. Cheng, "Straining effects in MoS 2 monolayer on nanostructured substrates: temperature-dependent photoluminescence and exciton dynamics", Nanoscale, 10, 5717 (2018)

6. M. Titze and H. Li, "Interpretation of optical three-dimensional coherent spectroscopy", Phys. Rev. A 96, 032508 (2017)

7. F. Gao, Y. Gong, M. Titze, R. Almeida, P. M. Ajayan, and H. Li, "Valley trion dynamics in monolayer $MoSe_2$", Phys. Rev. B 94, 245413 (2016)

8. M. Titze , B. Li, P. M. Ajayan, H. Li, "Intrinsic Homogeneous Linewidth of Trions in Monolayer MoSe 2 ", CLEO 2018, FF1D.3, May 13-18, San Jose, California

9. M. Titze and H. Li, "Optical 2D coherent spectroscopy of valley dynamics in monolayer transition metal dichalcogenide (Invited Paper)", Ultrafast Bandgap Photonics III 2018, 10638-24, 16 - 19 April, Orlando, Florida

10. M. Titze , F. Gao, R. Almeida, Y. Gong, P. M. Ajayan, and H. Li, "Valley Trion Dynamics in Monolayer MoSe2," in Frontiers in Optics 2016, JW4A.192. October 17-21, Rochester, New York

11. M. Titze , F. Gao, H. Li, "Trion Dynamics in Monolayer MoSe2", FAME, May 5-7, 2016, Tampa, Florida

12. M. Titze , F. Gao, S.T. Cundiff, H. Li, "Probing dipole-dipole interactions in dilute Rb vapor via double-quantum 2D coherent spectroscopy", PQE-2015, Jan 3-8, Snowbird, Utah